# COHERENCE PROPERTIES OF MICROCAVITY POLARITONS: FROM PARAMETRIC SCATTERING TO BOSE-EINSTEIN CONDENSATION

THÈSE N$^{O}$ 3515 (2006)

PRÉSENTÉE LE 12 MAI 2006

À LA FACULTÉ SCIENCES DE BASE

Laboratoire d'optoélectronque quantique

SECTION DE PHYSIQUE

ÉCOLE POLYTECHNIQUE FÉDÉRALE DE LAUSANNE

POUR L'OBTENTION DU GRADE DE DOCTEUR ÈS SCIENCES

PAR

Stefan KUNDERMANN

Diplom-Physiker, Technische Universität Darmstadt, Allemagne
et de nationalité allemande

acceptée sur proposition du jury:

Prof. R. Schaller, président du jury
Dr J.-L. Staehli, directeur de thèse
Prof. M. Bayer, rapporteur
Prof. A. Imamoglu, rapporteur
Prof. V. Savona, rapporteur

ÉCOLE POLYTECHNIQUE
FÉDÉRALE DE LAUSANNE

Lausanne, EPFL
2006

# Contents

# Abstract

This thesis presents the coherence properties of polaritons in semiconductor microcavities. Semiconductor microcavities are microstructures in which the exciton ground state of a semiconductor quantum well is coupled to a photonic mode of a microresonator. The strong coupling mixes the character of excitons and photons, giving rise to the lower and upper polariton branches, quasiparticles with an unusual energetic dispersion relation due to the extreme mass difference between exciton and photon. Particularly special is the dispersion of the lower polariton, which forms a dip in the 2-dimensional k-space around the lowest energy state with zero in-plane momentum. In this dip, which can be seen as a trap in momentum space, the polaritons are efficiently isolated from dephasing mechanisms involving phonons. Polaritons can be resonantly excited at desired points on the polariton dispersion by shining on the microcavity laser light at the appropriate angle and wavelength. Polaritons can interact and scatter pairwise with each other conserving energy and in plane momentum k, a process similar to parametric scattering of photons in a nonlinear crystal. One polariton from a pump reservoir scatters down to the signal state at k = 0 (corresponding to normal incidence) and a second takes away the excess energy and momentum of the first and scatters up to the idler position ($\{k_P, k_P\} \rightarrow \{0, 2k_P\}$). This process can be stimulated by a small amount of signal polaritons injected with a probe laser beam at normal incidence.

Here the coherence properties of the polariton parametric scattering have been investigated using spectroscopy techniques sensitive to the optical phase, for example coherent control with phase-locked femtosecond probe pulses. Just above the threshold for the stimulated parametric scattering, the parametric amplification process is given by the linear superposition of the individual amplification processes of each probe pulse. The emission of signal, pump, and idler can be controlled by tuning the relative phase of the 150fs-long probe pulses, which are separated by a few picoseconds in time. Experiments are presented that deal with the real-time dynamics of the parametric scattering in the spontaneous and the stimulated regime. It is shown, that in the spontaneous regime the scattering is started by a small amount of polaritons which have relaxed to the band bottom by emitting phonons. In the regime where polariton scattering is stimulated by an external probe, the rise of the signal intensity is delayed with respect to the arrival time of both pump and probe, a feature that can be attributed to the complex phase-matching mechanism for the parametric scattering.

In the second part of the thesis, the spontaneous build up of a macroscopic coherence in a CdTe microcavity under non-resonant laser excitation is analysed. The build up of a long-range spatial coherence easily exceeding the thermal wavelength of

the polaritons is shown. This is the hallmark of Bose-Einstein condensation and the proof of a macroscopic wavefunction. Experimental data on the statistical distribution of the polaritons in time, the polarisation of the non-linear emission, and the quantum transition from a thermal to a coherent state[1] confirm that Bose-Einstein condensation of microcavity polaritons has been observed. We regard these observations as the first bullet-proof evidence for spontaneous Bose-Einstein condensation in a solid state system, a phenomenon that has been the subject to many investigations and controversies during the past four decades.

keywords: microcavity polaritons, excitons, parametric amplification, parametric oscillator, coherent control, Bose-Einstein condensation, interferometry

[1]The data about the statistical distribution, the polarisation, and the transition from a thermal to a coherent state is by courtesy of Jacek Kasprzak of the University of Grenoble.

# Version abrégée

Cette thèse présente une investigation des propriétés cohérentes des polaritons dans des microcavités semiconductrices. Les microcavités semiconductrices sont des microstructures dans lesquelles on observe un régime de couplage fort entre l'état fondamental de l'exciton dans un puits quantique et un mode photonique du microrésonateur. Le couplage fort mélange les propriétés de l'exciton et du photon et donne naissance à deux branches de polaritons. Ces quasi-particules ont une dispersion énergétique inusuelle due à la grande différence de masse effective entre exciton et photon. La dispersion de la branche basse de polariton forme une sorte de piège dans l'espace réciproque bidimensionel autour de l'état de plus basse énergie, à $k = 0$. Dans ce piège les polaritons sont isolés efficacement des processus de déphasage impliquant des phonons. Il est possible de créer optiquement des polaritons dans un état spécifique à l'aide de faisceaux laser d'énergie et d'angle d'incidence adéquats. Les polaritons peuvent interagir entre eux en conservant l'énergie et la quantité de mouvement, de manière similaire à la diffusion paramétrique de photons dans un cristal non-linéaire. Un polariton du réservoir de pompe diffuse alors vers l'état du signal à $k = 0$ (ce qui correspond à incidence normale) alors qu'un deuxième gagne son énergie et sa quantité du mouvement excédentaires et diffuse vers l'état du complémentaire ($\{k_P, k_P\} \rightarrow \{0, 2k_P\}$). Il est possible de stimuler ce processus en injectant une petite quantité de polaritons dans l'état signal avec un faisceau laser de sonde.

Les propriétés de cohérence de la diffusion paramétrique ont été étudiées à l'aide de techniques spectroscopiques sensibles à la phase optique, comme le contrôle cohérent utilisant des impulsions femtosecondes de phase relative bien définie. Juste en-dessous du seuil de diffusion paramétrique stimulée, le processus d'amplification est dû à la superposition des processus d'amplification de chaque impulsions sonde. L'émission provenant du signal, de la pompe et du complémentaire peut-être contrôlée en ajustant la phase relative entre les deux impulsion sonde de 150 fs de durée, séparées dans le temps de quelques picosecondes. D'autre part, nous avons réalisé des mesures de la dynamique en temps réel de la diffusion paramétrique en régimes spontané et stimulé. Nous avons démontré que dans le régime spontané la diffusion paramétrique est initiée par les quelques polaritons qui ont relaxé vers le bas de la bande par émission de phonons. Dans le régime où la diffusion est stimulée par une sonde externe, la montée du signal est retardée par rapport à l'instant où arrivent la pompe et la sonde, une propriété qui peut-être attribuée à un processus complexe lié à l'accord de phase de la diffusion paramétrique.

Dans une deuxième partie nous nous intéressons à l'apparition d'une cohérence

macroscopique spontanée dans les microcavités CdTe sous excitation non-résonante. Nous observons la formation d'une cohérence spatiale dont la portée excède largement la longueur de corrélation thermique. Cette observation démontre l'existence d'une fonction d'onde macroscopique, et constitue ainsi une preuve essentielle de la formation d'un condensat de Bose-Einstein. D'autre parts des résultats concernant la thermodynamique des polaritons, la polarisation de l'émission non-linéaire, et la transition d'un état thermique vers un état cohérent[2] confirment la validité de notre conclusion. Ces observations apportent ainsi la première preuve indiscutable de la formation d'un condensat de Bose en milieu solide, un phènomène qui a été sujet de nombreuses études et controverses ces derniers 40 ans.

[2]Les données experimentales sur la distribution, la polarisation et la transition d'un état thermique vers un état cohérent sont des données pas encore publiés de Jacek Kasprzak de l'Université de Grenoble qui, par amabilité, ont été mis à disposition pour la discussion dans cette thèse.

# Zusammenfassung

Die vorliegende Dissertation beschäftigt sich mit den Kohärenzeigenschaften von Polaritonen in Halbleiter-Mikroresonatoren. Halbleiter-Mikroresonatoren sind Mikrostrukturen, in denen der Exzitonen-Grundzustand eines Halbleiter-Quantentopfes mit einer photonischen Mode eines Mikroresonators stark koppelt. Durch die starke Kopplung von Exziton und Photon entstehen die neuen Eigenzustände des Systems, die Polaritonen. Aufgrund der extremen Massendifferenz haben diese Quasiteilchen eine unübliche energetische Dispersionsrelation. Von besonderer Bedeutung ist die Dispersion des unteren Polaritonen-Niveaus, die eine Vertiefung im 2-dimensionalen k-Raum um den Zustand mit verschwindendem Impuls in der Resonatorebene aufweist. Innerhalb dieser Vertiefung, die als eine Art Falle angesehen werden kann, sind die Polaritonen wirkungsvoll von Dephasierungsmechanismen mit Phononen isoliert. Polaritonen können durch resonante Laserstrahlung an gewünschten Stellen der Dispersionskurve durch die Anpassung des Einfallswinkels und der Laserwellenlänge angeregt werden. Innerhalb der Vertiefung können die Polaritonen unter Einhaltung von Energie- und Impulserhaltung paarweise streuen. Ein Polariton vom Pumpreservoir streut in den energetisch niedrigeren Zustand bei $k = 0$ (entsprechend normaler Einfallsrichtung) und ein zweites übernimmt überschüssige Energie und Impuls des ersten und streut in den energetisch höheren Idler-Zustand ($\{k_P, k_P\} \rightarrow \{0, 2k_P\}$). Der Prozess kann mittels einer kleinen Menge von Signal-Polaritonen, die durch einen schwachen Prüfimpuls angeregt werden, stimuliert werden.

Durch optisch phasensensitive spektroskopische Methoden wie kohärente Kontrolle mit Femtosekunden-Laserimpulsen, die eine feste Phasenbeziehung aufweisen. Knapp oberhalb der Schwelle für die stimulierte parametrische Polaritonen-Streuung, ergibt sich der parametrische Verstärkungsprozess als lineare Überlagerung der jeweiligen Verstärkungsprozesse der jeweiligen Prüfimpulse. Die Emission von Signal-, Pump- und Idler-Zuständen kann durch das Verändern der relativen Phase zweier Prüfimpulse mit 150 $fs$ Zeitdauer, die in einem Zeitabstand von mehreren Pikosekunden auftreffen, gesteuert werden. Es werden Experimente vorgestellt, die sich mit dem Realzeitverhalten der parametrischen Streuung im spontanen und stimulierten Regime beschäftigen. Es wird gezeigt, dass die spontane parametrische Streuung von einer kleinen Menge von Polaritonen gestartet wird, die aufgrund Emission von Phononen im untersten Polaritonenzustand angekommen sind. Im stimulierten Regime ist der Anstieg der Signal Emissions-Intensität im Vergleich zur Ankunftszeit von Pump- und Prüfimpuls verzögert, was einem komplizierten Phasenanpassungs-Mechanismus zuzuordnen ist.

Im zweiten Teil der Arbeit wird das spontane Auftreten einer makroskopischen

Kohärenz, die in einem Cadmium-Tellurit-Mikroresonator unter nicht-resonanter Anregung auftritt, untersucht. Das Auftreten einer räumlichen Weitbereichs-Kohärenz, die mehrfach die thermische Wellenlänge der Polaritonen überschreitet, wird gezeigt, eine Schlüsseleigenschaft von Bose-Einstein Kondensation und der Beweis für die Existenz einer makroskopischen Wellenfunktion. Aufgrund weiterer experimenteller Daten über die statistische Verteilung der Polaritonen, die Polarisation der nicht-linearen Emission und dem quantenstatistischen Übergang von einem thermischen in einen kohärenten Zustand[3], kann geschlussfolgert werden, dass Bose-Einstein Kondensation von Polaritonen beobachtet wurde. Wir betrachten die gezeigten Ergebnisse als einen eindeutigen Beleg für spontane Bose-Einstein Kondensation in eimem Festkörper, ein Phänomen, das in den vergangenen 40 Jahren Gegenstand vieler Untersuchungen und kontroverser Diskussionen war.

[3]Die Daten über Verteilung, Polarisation und Übergang von einem thermischen in einen kohärenten Zustand sind unveröffentlichte Ergebnisse von Jacek Kasprzak von der Universität Grenoble, und wurden freundlicherweise zur Diskussion in der vorliegenden Arbeit zur Verfügung gestellt.

# Riassunto

Questa tesi studia le proprietà di coerenza dei polaritoni nelle microcavità a semiconduttore. Le microcavità sono microstrutture in cui lo stato fondamentale dell'eccitone in un pozzo quantico è accoppiato al modo fotonico del microrisonatore. L'accoppiamento forte mescola le caratteristiche di eccitoni e fotoni, generando i polaritoni, quasiparticelle con una dispersione energetica molto inusuale a causa della differenza tra la massa dell'eccitone e quella del fotone. In particolare, la dispersione del polaritone inferiore forma una buca nello spazio k reciproco attorno agli stati con minore energia. In questa buca, che puo' essere considerata una buca nello spazio degli impulsi, i polaritoni non risentono della decoerenza indotta dai fononi. I polaritoni possono essere eccitati in risonanza nei punti desiderati della dispersione illuminando la microcavità con luce laser proveniente da un appropriato angolo e di appropriata frequenza. I polaritoni possono interagire tra loro e diffondere due a due conservando energia e impulso k (nel piano del pozzo quantico), un processo simile alla diffusione parametrica dei fotoni in un cristallo nonlineare. Un polaritone diffonde da un serbatoio creato dal fascio di pompa verso lo stato del segnale a k=0 (che corresponde ad una eccitazione ad incidenza normale) e un secondo polaritone porta via la quantità di moto e l'energia che il primo polaritone ha in eccesso, diffondendo verso lo stato dell'idler ($\{k_P, k_P\} \rightarrow \{0, 2k_P\}$). Il processo può essere stimolato da una piccola quantità di polaritoni iniettata dal fascio di sonda ad incidenza normale.

Le proprietà di coerenza dei polaritoni sono state studiate con tecniche spettroscopiche sensibili alla fase, come il controllo coerente con impulsi al femtosecondo. Appena al di sopra della soglia per la diffusione parametrica, il processo di amplificazione parametrica è la sovrapposizione lineare dell'amplificazione di ciascuno dei due impulsi di sonda. L'emissione del segnale, della pompa e dell'idler possono essere controllate dalla fase relativa dei due impulsi di sonda, che durano 150 fs, ma sono separati da diversi picosecondi. Sono presentati anche degli esperimenti sulla dinamica in tempo reale della diffusione parametrica nel regime spontaneo e nel regime stimolato. Si mostra che nel regime di diffusione spontanea la diffusione è iniziata da un piccolo numero di polaritoni che rilassano al fondo della banda emettendo dei fononi. Nel regime in cui invece la diffusione è stimolata da una sonda esterna, la crescita dell'intensità del segnale è ritardata rispetto all'arrivo degli impulsi di pompa e di sonda, una caratteristica che può essere attribuita al complesso meccanismo di "phase matching" della diffusione parametrica.

In una seconda parte della tesi si analizza la coerenza spontanea in una microcavità di CdTe sottoposta ad eccitazione non risonante. Si mette in evidenza l'apparire di una

coerenza spaziale a lungo raggio su distanze che eccedono di gran lunga la lunghezza d'onda termica dei polaritoni, il marchio ufficiale della condensazione di Bose-Einstein e la prova dell'esistenza di una funzione d'onda macroscopica. Dati sperimentali sulla distribuzione statistica dei polaritoni, la polarizzazione dell'emissione nonlineare e la transizione da uno stato termico ad uno stato coerente[4] confermano la conclusione che la condensazione di Bose-Einstein dei polaritoni è stata osservata. Consideriamo queste osservazioni come la prima prova inattaccabile della condensazione di Bose-Einstein spontanea nello stato solido, un fenomeno che è stato oggetto di innumerevoli studi e controversie negli scorsi quarant'anni.

[4]I dati sperimentali sulla distribuzione statistica dei polaritoni, la polarizzazione e la transizione da uno stato termico ad uno stato coerente e una cortesia di Jacek Kasprzak dell'Università di Grenoble.

# Chapter 1

# Introduction

The epoch of quantum physics started in 1900, when Max Planck presented his work on the spectrum of black-body radiation, later known as Planck's law of radiation. His work broke with the largely accepted mechanistic point of view in physics at that time which can be characterised by the Leibnitz statement "Natura non facit saltus", nature does not make jumps. In order to derive his law for black-body radiation, Planck had to introduce that electromagnetic radiation is exchanged by small quanta and not in a continuous way. The introduction of this concept marks the birth of quantum physics. At the time of the publication of his work, Planck essentially thought about his concept basically as a mathematical tool rather than an epoch-making new concept. Five years later, Albert Einstein found in his works about the photoelectric-effect, that these quanta of the electromagnetic field - photons - are real particles and not simply a mathematical construct. It was in 1924 that S. N. Bose managed to derive Planck's formula considering photons a gas of indistinguishable particles. His concept of treating photons as indistinguishable particles was generalised by Einstein to any gas of bosons. An important consequence of the concept of indistinguishability is, that bosons have an enhanced probability to be in the same quantum state with respect to distinguishable particles. This statistical property is the bases of effects such as laser stimulation, superfluidity, Bose-Einstein condensation, and superconductivity.

Laser stimulation is the phenomenon with the largest impact on our everyday life, since we are frequently using semiconductor lasers in CD-players, DVD-players, and in telecommunications. It was in 1962 that the first semiconductor laser was demonstrated by Hall [50] using a GaAs pn-junction. These first semiconductor lasers only worked at liquid nitrogen temperature in the pulsed regime. The breakthrough for a broad application was achieved in 1970 independently by Alferov in the Soviet Union [20] and Panish at Bell Labs in the US [82, 54] using a heterojunction structure. During the 70s new crystal growth technologies were developed such as molecular beam epitaxy (MBE) and metal-organic chemical vapour deposition (MOCVD). These new technologies allowed stacking of almost defect free thin layers of different semiconductor materials in a very precise and controlled manner. In such ultra thin so-called quantum wells, the carriers are quasi-confined in the growth direction. In such a 2-dimensional structure, the number of electronic states is strongly reduced compared with that in 3D and a

much lower threshold current for quantum-well lasers was anticipated. In 1975 Van der Ziel and co-workers built the first optically pumped laser with a quantum well as an active region [113] and an electrically pumped quantum well laser was demonstrated two years later by Dupuis et al. [42]. The advancement of the MBE technology allowed the stacking of hundreds of layers of top quality semiconductor material and it was in 1979 that the first vertical cavity surface emitting laser (VCSEL) using Bragg reflectors to form the cavity was built [107]. All of these developments paved the way for the application of semiconductor lasers in consumer electronics and telecommunication.

In a laser a large number of photons are in the same state and the resulting light field is coherent. According to the fundamentals of quantum mechanics, matter particles can accumulate in the same state and acquire a macroscopic coherence. A consequence of which is the superfluidity of helium at low temperature or Bose-Einstein condensation of dilute atomic gases. For a long time it has been a dream to realise such phenomena in a solid state system. One promising candidate to achieve this goal has been the exciton quasiparticle in a semiconductor: particularly suited for the effect of Bose-Einstein condensation it was proposed as early as 1962 by Blatt [11]. The problem of excitons is that at a certain density their wavefunctions start to mutually penetrate and a plasma of electrons and holes forms, i.e. the picture of an exciton as a composite boson is no more valid.

An attempt to overcome this problem was made in the early 90s. A quantum well was embedded in a microresonator placed at the antinodes of the electric field of its resonant photon mode. The energy of the resonator mode was fixed around the 1s-excitonic resonance of the quantum well. Due to the high finesse of the microcavity and the homogeneity of the quantum well, the strong coupling regime of exciton and photon mode could be achieved [117]. In this regime, exciton and photon wavefunctions mix and give rise to new eigenstates of the system, the microcavity polaritons. These eigenmodes exhibit properties of both exciton and photon mode. The polariton mode at lower energy, the lower polariton, features a unique dispersion relation. For very small in-plane wavevector, the dispersion is very steep due to the steep dispersion relation of the photon mode. At higher in-plane momentum, it recovers the very flat dispersion relation of the uncoupled 2-dimensional quantum well exciton. The very steep dispersion of the polaritons around zero in-plane momentum implies that the polaritons have a very low mass, about $10^4$ to $10^5$ times lower than the exciton mass. Collective bosonic effects for polaritons can be expected when their spatial separation is of the order of their de Broglie wavelength. The thermal de Broglie wavelength of the polaritons is about 100 times larger than the one of excitons (about $0.1\mu m$ for excitons and $10\mu m$ for polaritons at $T \sim 10\,K$). This feature makes microcavity polaritons promising candidates for the achievement of quantum degenerate effects, especially Bose-Einstein condensation.

After the first demonstration of a microcavity working in the strong coupling regime, the research focussed on the characterisation of the linear properties such as the in-plane dispersion [57] and the improvement of the cavity structures. In 1996 a first series of measurements claimed the observation of the spontaneous transition to a coherent state in the polariton system. It turned out that the observed transition occured in the weak coupling regime and a conventional photon-laser transition had been observed.

Further works tried to evidence such a transition under non-resonant excitation using microcavities in the GaAs material system, but a non-linear transition occuring in the strong-coupling regime could not be reported. Later on the idea was risen to cool the polaritons using electrons as scattering partners and to overcome the relaxation bottleneck for the polaritons [74], but the experimental investigation could not demonstrate a spontaneous coherent phase transition in such a structure [65]. A conclusive spontaneous phase transition occurring in the strong coupling regime in GaAs based microcavities has not been evidenced up to now.

However it has been possible to demonstrate the achievement of quantum degeneracy of polaritons by the direct resonant excitation of a few polariton modes, when the coherence of the incident laser beam is transferred to the polariton system. This coherence is efficiently preserved in a microcavity because pure dephasing mechanisms are not efficient and the relaxation time is comparable to the population lifetime of the polaritons. The absence of efficient pure dephasing mechanisms enables the transfer of the injected polariton excitation to other states preserving the initial coherence. Based on this property it has been possible to demonstrate a parametric polariton wavemixing, in which the coherence of the incident laser is transferred to a signal and an idler polariton mode, satisfying energy and in-plane momentum conservation [99]. This process is highly efficient and presents potential for technical application in ultrafast amplification devices [93]. A large variety of features observed in optical parametric oscillators and amplifiers can also be observed in the polariton parametric oscillator such as, the possibility to create entangled photons [77, 96] and phase coherence [64]. Furthermore, it has been demonstrated, that the polaritons in the parametric scattering regime can indeed accumulate in one single quantum state, demonstrating the quantum degeneracy of the polaritons [7].

The appearance of a spontaneously driven coherent transition in GaAs based microcavities could not be demonstrated. The relaxation of the polaritons appears to be too inefficient to achieve a condensation in the lowest energy state as the strong coupling regime breaks down due to the very high exciton densities needed. In 1996 the first strongly coupled microcavity in the CdTe material system was realised. The advantage of this system is the larger oscillator strength of the exciton. Two years later Dang et al. demonstrated a non-linear stimulation effect occurring in the strong coupling regime under non-resonant excitation[33]. Up to now this is the only appearance of a non-linear spontaneous stimulation effect in a microcavity occurring in the strong coupling regime under non-resonant excitation.

The present thesis investigates the coherence and dynamics properties of microcavity polaritons. Two processes are considered:

- **Parametric scattering of polaritons.** Here the coherence of the laser field is transferred to the polariton field and the coherence measured is induced by the exciting laser. The sample used here is a single quantum well GaAs based microcavity.

- **Incoherent relaxation of polaritons and stimulated emission from the bottom of the lower polariton band.** In this process, the incident coherence

of the exciting laser is lost. For the experiments a multi quantum well CdTe based microcavity has been employed.

The basic properties of the microcavity polaritons and the polariton parametric scattering are described in chapter 2. In a first set of experiments the phase coherent properties of polariton parametric scattering are investigatated using a coherent control technique in chapter 3. Chapter 4 is devoted to the rich dynamical phenomena which can be observed for the polariton parametric scattering in the spontaneous as well as in the stimulated case. Chapter 5 discusses the coherence properties of the polaritons spontaneously relaxing to the bottom of the polariton band when a CdTe cavity is excited non-resonantly. It is discussed whether the appearance of the spontaneous coherence can be attributed to the phenomenon of Bose-Einstein condensation of polaritons. Chapter 6 concludes this work and gives an outlook on the future of polariton physics.

# Chapter 2

# Fundamentals of Polaritons

Polaritons are the elementary excitations of microcavities. In this chapter we develop the fundamental properties of microcavity polaritons and their interaction at high intensity. We start with the description of excitons in quantum wells and the dispersion relation of a planar Fabry-Pérot resonator. In section 2.3, the strong coupling of resonator photons and excitons is described, the dispersion relation of the polaritons is presented, and the linear Hamiltonian shown. In section 2.4 the employed microcavity samples are described. 2.5 introduces polariton parametric oscillation and amplification starting with the desription of standard optical parametric amplification and oscillation in transparent crystals exhibiting a $\chi^{(2)}$-type non-linearity. Furthermore the experimental data on parametric scattering is presented. In 2.5.3, the full non-linear Hamiltonian of the system is described and the Heisenberg equations of motion for the polarisation in the three parametric modes are developped. A classification of the different phenomena observed in standard optical amplification and in the microcavity polariton system is given in 2.6.1.

## 2.1 Excitons in a Quantum Well

A quantum well consists of a thin layer of a semiconductor material, sandwiched between a material with a larger band-gap. Consequently the free carriers in the well, i.e. electrons in the conduction band and holes in the valence band are confined in the z-direction (the direction normal to the quantum well layer). An electron-hole pair can be created by the absorption of a photon. In this case an electron is excited from the valence band into the conduction band and the energy of this excited state amounts to

$$E_c(\mathbf{k}_\parallel) - E_v(\mathbf{k}_\parallel) = E_{gap} + \frac{\hbar^2 k_{\parallel,e}^2}{2m_e^*} + \frac{\hbar^2 k_{\parallel,h}^2}{2m_h^*}, \tag{2.1}$$

where $m_e^*$ and $m_e^*$ correspond to the effective mass of the electron and the hole. $\mathbf{k}_\parallel$ is the in-plane wavevector of electron and hole in the plane of the quantum well (they are confined in the z-direction). Electrons and holes have opposite charge and thus experience an attractive Coulomb interaction. Eq. 2.1 has to be modified in order

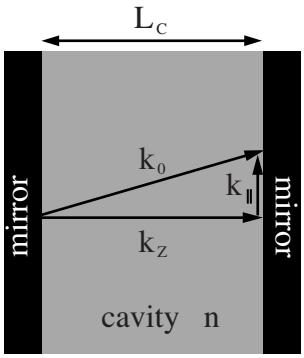


**Figure 2.1:** Schematic of a planar Fabry-Pérot resonator. The two planar mirrors are separated by a spacer of some dielectric material with refractive index n and thickness $L_c$.

to account for this interaction. In the framework of the Wannier theory of excitons, the exciton problem reduces to the well known hydrogen problem and its solution are easily described:

$$E_n = -R_y \cdot \frac{1}{n^2} = -\frac{\mu e^4}{8\epsilon h^2}\frac{1}{n^2} \tag{2.2}$$

The influence of the crystal ions on the electron-hole pair is accounted for by the dielectric constant, i.e. the Coulomb interaction of electron and hole is screened by the dielectric surrounding. The binding energy of the exciton ground state (its Rydberg constant $R_y$) is of the order of a few $meV$. As a consequence, the excitons are ionised at room-temperature in common materials used in semiconductor optics such as GaAs, InGaAs, and AlGaAs.

The energy dispersion $E(k_\parallel)$ of an exciton moving in a quantum well can be written as follows:

$$E_x^{(n)}(\mathbf{k}_\parallel) = E_{gap} - E_n + \frac{\hbar^2 k_\parallel^2}{2M^*} = E_0 + \frac{\hbar^2 k_\parallel^2}{2M^*}, \tag{2.3}$$

Excitons in quantum wells can be excited by resonant light. At normal incidence, excitons are created by photons of energy $E_0 = \hbar\omega_0$. The effective mass of excitons in GaAs is approximately one fourth the mass of a free electron ($M^\star = 0.25 \cdot 10^{-31} kg$), or equivalently about 4-5 orders of magnitude heavier than the mass attributed to the photon mode in a microcavity. As a consequence its energy $E_x^{(n)}(\mathbf{k}_\parallel)$ varies much slower than the energy of the photon mode.

## 2.2 Photon modes in a microresonator

The semiconductor microcavity consists of a bottom distributed Bragg reflector (DBR) mirror grown on a substrate, a cavity which contains the active medium (the quantum well) and a top DBR mirror. A schematic of a planar Fabry-Pérot resonator consisting

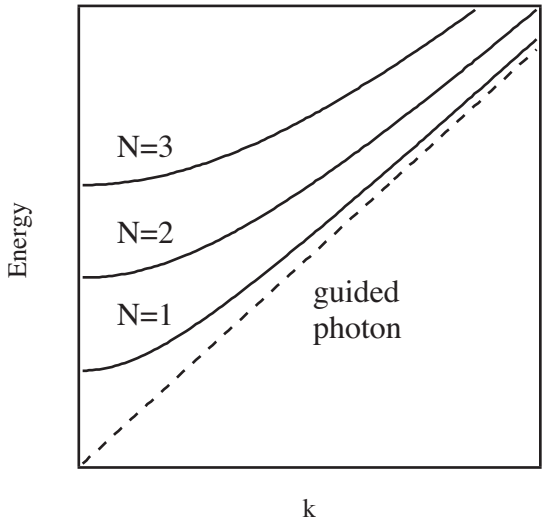


**Figure 2.2:** Photon energy of the resonant Fabry-Pérot mode versus $k_\parallel$. The dashed line indicates the dispersion of the photon mode which is guided inside the cavity. The N=1, 2, 3 modes are shown.

in a cavity with cavity length $L_c$ is depicted in fig. 2.1. The wavevector $k_0 = \frac{\omega}{c} \cdot n$ of a photon mode inside the cavity can be split into its component in the plane of the cavity ($k_\parallel$) and its component perpendicular to the plane in the z-direction ($k_Z$), where $k_0^2 = k_Z^2 + k_\parallel^2$. The resonator quantises the wavevector of the resonant mode in the z-direction, such that

$$k_z L_c = \sqrt{\frac{\omega^2}{c^2} n_{cav}^2 - k_\parallel^2} L_c = N\pi \tag{2.4}$$

$\omega$ is the photon frequency and $n_{cav}$ the refraction index of the spacer inside the cavity.

Using 2.4 the dispersion relation of the resonator $E(k_\parallel)$ can be drawn (fig. 2.2). The photon energies of the resonant Fabry-Pérot modes for N=1, 2, 3 are depicted versus $k_\parallel$. For small $k_\parallel$ the dispersion is parabolic, whereas for high in-plane momenta the curve joins the dispersion of the 2-dimensional photon mode propagating in the plane of the resonator (dashed line in fig. 2.2).

For small in-plane momentum equation 2.4 can be approximated by a Taylor series:

$$E_C(k_\parallel) \cong \frac{\hbar c}{n_{cav}} k_z + \frac{1}{2} \frac{\hbar c}{n_{cav}} \frac{k_\parallel^2}{k_z} \tag{2.5}$$

The first term of 2.5 is the energy of the photon mode in the normal direction of the cavity. The second can be considered to be the "kinetic energy" of the photon in the plane of the cavity. Thus we can extract from it a parameter which corresponds

to the mass of the resonant photon mode according to $E_{kin} = \frac{\hbar^2 k_\parallel^2}{2m}$. In order to relate the mass to the incident vacuum photon wavelength also the resonance condition 2.4 is put into 2.6:

$$m = \frac{\hbar n_{cav}}{c} k_z = \frac{\hbar n_{cav} N\pi}{cL_c} = \frac{\hbar N\pi}{c\lambda_0} \tag{2.6}$$

N is the order of the Fabry-Pérot-resonance and $\lambda_0$ the relevant vacuum wavelength. For a wavelength of 800nm the photon mass for N=1 (the lowest resonant mode) is $1.4 \cdot 10^{-36} kg$ - 5 orders of magnitude lower than the mass of an exciton which is typically of the order of 10% of the free electron mass.

## 2.3 Strong coupling regime

We have discussed the properties of a quantum well exciton and a Fabry-Pérot resonator in the previous sections. If we place a quantum well in a microcavity at the antinodes of the electric field of the photon mode, excitons and confined photons can interact. In the strong coupling regime, excitons and photons exchange their energy several times, before the energy leaves the cavity as a photon, or the exciton scatters with a phonon into a high momentum state. Thus the strong coupling regime requires that the cavity photon is transformed into an exciton before it decays into an external photon, and that the exciton transforms into a resonator photon before it experiences dephasing, in other words the energy splitting $2\hbar\Omega_R$ between the polariton modes is larger than the respective broadening of the exciton and photon mode. In this case, exciton and photon are no longer the normal modes of the system and the new eigenmodes of the system, the microcavity polaritons, form.

### Linear Hamiltonian of the system

The linear Hamiltonian of the strongly coupled exciton photon system reads

$$H_0 = \sum_k E_C(k_\parallel) a_{\mathbf{k}}^\dagger a_{\mathbf{k}} + \sum_k E_X(k_\parallel) b_{\mathbf{k}}^\dagger b_{\mathbf{k}} \qquad + \sum_k \hbar\Omega_R (a_{\mathbf{k}}^\dagger b_{\mathbf{k}} + b_{\mathbf{k}}^\dagger a_{\mathbf{k}}), \tag{2.7}$$

where $a_{\mathbf{k}}^\dagger, a_{\mathbf{k}}$ and $b_{\mathbf{k}}^\dagger, b_{\mathbf{k}}$ are the creation and annihilation operators of photon and exciton with in-plane wavevector $\mathbf{k}$ respectively, and $\hbar\Omega_R$ describes the coupling energy. The dispersion of the coupled polariton modes can be calculated using the expressions found in section 2.2 and 2.1 can be written as follows [97]:

$$E_{LP,UP}(k_\parallel) = \frac{E_C(k_\parallel) + E_X(k_\parallel)}{2} \mp \frac{1}{2}\sqrt{(E_C(k_\parallel) - E_X(k_\parallel))^2 + 4|\hbar\Omega_R|^2} \tag{2.8}$$

The in-plane dispersion of the polaritons and the uncoupled photons and excitons is shown in figure 2.3. The uncoupled exciton shows almost no dispersion due to its

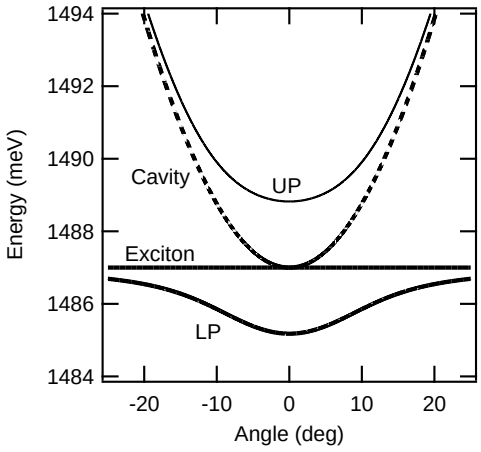


**Figure 2.3:** Angular dispersion of lower and upper polariton when exciton and cavity photon are in resonance. The uncoupled dispersion of exciton and cavity photon is also drawn.

large effective mass. In contrast, the cavity modes show a very steep dispersion, which has a parabola-like shape around $k = 0$. The lower polariton dispersion exhibits a dip around $k = 0$ and joins the dispersion of the bare exciton for high in-plane momentum. The shape of the upper polariton mode dispersion is similar to the dispersion of the cavity modes.

Since exciton and photon are no longer the stationary states of the system, it is convenient to diagonalise the Hamiltonian by the following unitary transformation:

$$\begin{pmatrix} p_{\mathbf{k}} \\ u_{\mathbf{k}} \end{pmatrix} = \begin{pmatrix} X_k & C_k \\ -C_k & X_k \end{pmatrix} \begin{pmatrix} b_{\mathbf{k}} \\ a_{\mathbf{k}} \end{pmatrix} \tag{2.9}$$

$X_k$ and $C_k$ being the Hopfield factors introduced in his pioneering work [56] in 1958 described by

$$X_k = \frac{1}{\sqrt{1 + (\frac{\hbar\Omega_R}{E_{LP}(k_\parallel) - E_C(k_\parallel)})^2}} \qquad C_k = -\frac{1}{\sqrt{1 + (\frac{E_{LP}(k_\parallel) - E_C(k_\parallel)}{\hbar\Omega_R})^2}}. \tag{2.10}$$

We end up with the linear Hamiltonian describing the system in the polariton basis:

$$H_0 = \sum_k E_{LP}(k_\parallel) p^\dagger_{\mathbf{k}} p_{\mathbf{k}} + \sum_k E_{UP}(k_\parallel) u^\dagger_{\mathbf{k}} u_{\mathbf{k}}. \tag{2.11}$$

$p^\dagger_{\mathbf{k}}, p_{\mathbf{k}}$ and $u^\dagger_{\mathbf{k}}, u_{\mathbf{k}}$ are the creation and annihilation operatrors for lower and upper polaritons at wavevector $\mathbf{k}$ respectively.

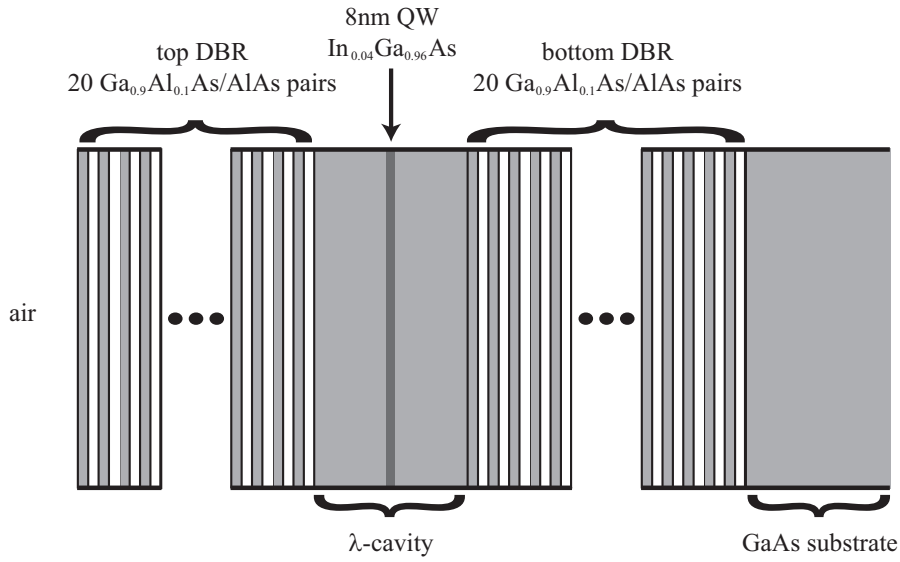


**Figure 2.4:** Structure of the III-V microcavity sample.

## 2.4 Microcavity samples

In the experimental work two different microcavity samples were investigated. For the work on parametric scattering of polaritons, a very high quality GaAs-based cavity sample has been employed. The very narrow linewidth of the sample allowed for the coherence and dynamics studies presented in chapter 3 and 4. The CdTe-based II-VI microcavity was used to study the condensation phenomena of the polaritons described in chapter 5. In the following we present the linear properties of both cavities.

### 2.4.1 III-V GaAs microcavity

The III-V microcavity was grown in the group of M. Ilegems by U. Oesterle at EPFL. It is the product of an intense study in optimising the linewidth of the exciton and the cavity resonance [110]. The sample structure is depicted in figure 2.4.

The sample was grown on a GaAs-substrate. The GaAs $\lambda$-cavity is sandwiched between a pair of Bragg-reflectors being composed of alternated $\lambda/4$-layers of AlGaAs and AlAs. The bottom mirror contains 26.5 pairs, whereas the top reflector is made out of 20 pairs. This asymmetry allows an efficient coupling of the laser light into the cavity. Whilst the very high reflectivity of the bottom mirror assures a high finesse of the resonator (the finesse in a similar bare cavity without quantum well and 20/29 pair mirrors amounts to 5530 [110]). The cavity contains an $8\,nm$ quantum well (QW) of $In_{0.04}Ga_{0.96}As$. The emission energy of the 1s level of the heavy hole exciton level is within the band-gap of GaAs and thus the sample can be studied in reflection and transmission. The linear characterisation of the cavity at normal incidence is shown in fig. 2.5.

The cavity spacer layer has a wedge and thus the resonance frequency of the res-

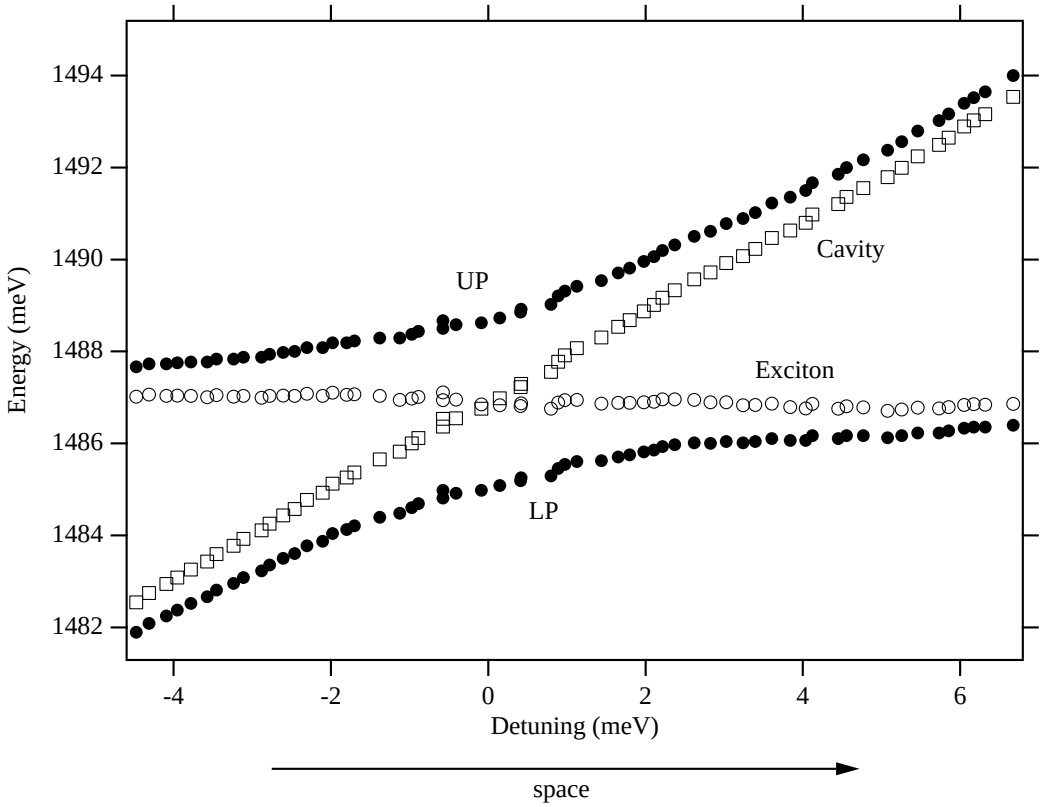


**Figure 2.5:** Linear characterisation of the III-V cavity sample. The energies of the lower (LP) and upper polariton (UP) have been carried out on different points in the direction of the cavity wedge in transmission experiments. The corresponding energy of the cavity and of the exciton have been calculated using eq. 2.8.

onator can be varied by moving the laser spot over the sample. The quantum well properties are the same all over the sample. The solid dots show the lower and the upper polariton resonance at $k = 0$, whereas the open circles and squares indicate the bare exciton and cavity energy. At zero detuning of cavity and exciton the polariton curves show their minimum energy splitting of $2\hbar\Omega_R = 3.6\,meV$. The linewidth (not determined here) is of the order of $0.1\,meV$ [110] giving a splitting to linewidth ratio of more than 30.

### 2.4.2 II-VI CdTe microcavity

The CdTe microcavity consists of a 2λ-cavity containing 4 stacks of 4 CdTe quantum wells at the antinodes of the electric field. The cavity material is $Cd_{40\%}Mn_{60\%}Te$ and the Bragg mirrors consist of $\lambda/4$-layers of $Cd_{40\%}Mn_{60\%}Te$ and $Cd_{75\%}Mg_{25\%}Te$. The cavity is characterised in reflectivity measurements. The energy of the polariton

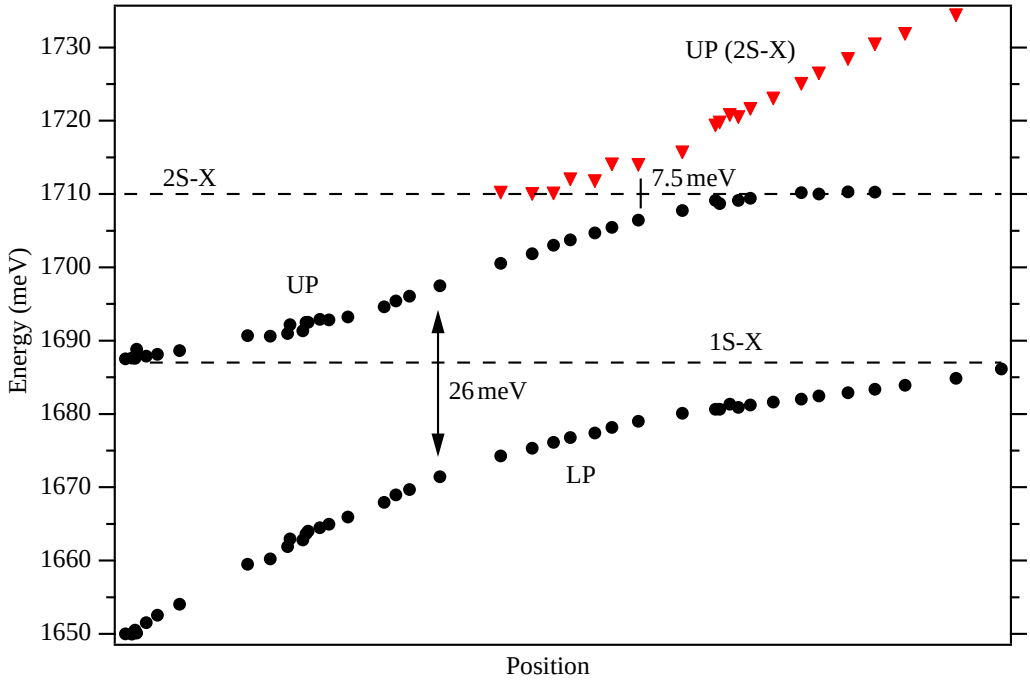


**Figure 2.6:** Linear characterisation of the II-VI cavity sample. The energies of the lower (LP) and upper polariton (UP) have been carried out on different points in the direction of the cavity wedge. The data is by courtesy of Jacek Kasprzak of the University of Grenoble.

resonances is depicted versus the sample position in fig. 2.6. The lower-upper polariton minimum energy splitting is $2\hbar\Omega_R = 26\,meV$. The upper polariton curve displays another anticrossing involving the 2S-exciton level with a minimum splitting of $7.5\,meV$. The width of the upper and lower polariton resonance at the minimum energy splitting amount to $0.5\,meV$ and $1.46\,meV$ respectively [88].

## 2.5 Polariton parametric oscillation and amplification

### 2.5.1 Parametric amplification and oscillation in transparent crystals

Parametric amplification was demonstrated almost 40 years ago [51, 23] using a $LiNbO_3$-crystal with a non-linear susceptibility $\chi^{(2)}$. In the experiment [51], the parametric amplification of a He-Ne laser beam in a $LiNbO_3$-crystal pumped by an argon ion laser is observed. Parametric amplification can be obtained straight-forwardly if we have a medium with a non-vanishing second order susceptibility $\chi^{(2)}$ [18]. In this case, the polarisation in the medium due to $\chi^{(2)}$ is

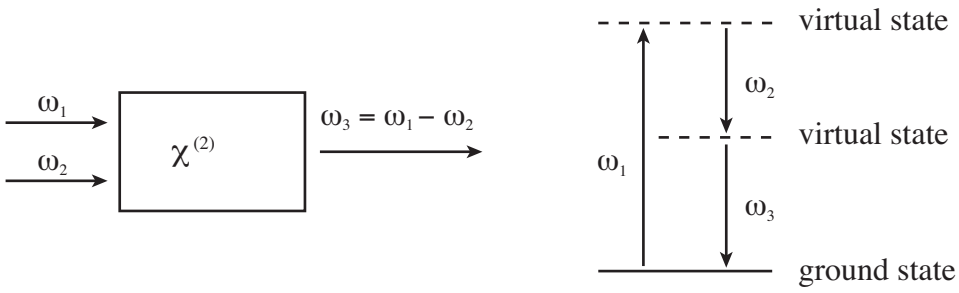


**Figure 2.7:** Difference frequency generation

$$\tilde{P}^{(2)} = \chi^{(2)} \tilde{E}(t)^2. \tag{2.12}$$

As input wave we consider a field with two distinct frequency components

$$\tilde{E}(t) = E_1 \cdot e^{-i\omega_1 t} + E_2 \cdot e^{-i\omega_2 t} + c.c. \tag{2.13}$$

If we precisely calculate the different terms of the second order polarisation we get five different processes: second harmonic generation of $\omega_1$, second harmonic generation of $\omega_2$, sum-frequency generation $\omega_1 + \omega_2$, difference-frequency generation $\omega_1 - \omega_2$, and optical rectification. In a concrete experiment, usually only one of the processes is observed with an apreciable intensity, since a complex phase-matching[1] has to be satisfied in the crystal. We want to focus on the difference frequency generation. In this case, the non-linear interaction of the incident waves $\omega_1$ and $\omega_2$ ($\omega_1 > \omega_2$) create a photon at frequency $\omega_3 = \omega_1 - \omega_2$ (see fig. 2.7). To conserve energy, for each photon created at $\omega_3$, a second photon at $\omega_2$ is formed. Fig. 2.7 shows the input and the output of the $\chi^{(2)}$-process as well as the energy level diagram. At the input, we have one photon at $\omega_1$ (a pump photon) and a second one at $\omega_2$ (a probe photon), and at the output we obtain one photon at $\omega_3 = \omega_1 - \omega_2$ (an idler photon) and two photons at $\omega_2$ (the amplified signal with one photon from the input, the other one generated due to energy conservation). The term "difference frequency generation" stands for the fact that a photon at the frequency difference between the initial two photons is generated. It is popular as well to name this process parametric amplification, since the photons at frequency $\omega_2$ are amplified. The process $\omega_1 \rightarrow \omega_2 + \omega_3$ can even occur when no $\omega_2$-field is applied, which is known as parametric fluorescence [23]. In this case the frequencies $\omega_2$ and $\omega_3$ are determined by the phase-matching in the crystal. When such a non-linear crystal is placed in an optical cavity, $\omega_2$ and/or $\omega_3$ can build up to very large values, when the cavity is resonant with one, two, or all three frequencies involved. Such a device is known as an optical parametric oscillator. It corresponds qualitatively to the microcavity, since here the active medium - the quantum well - is placed inside the cavity.

[1] energy and wavevector conservation

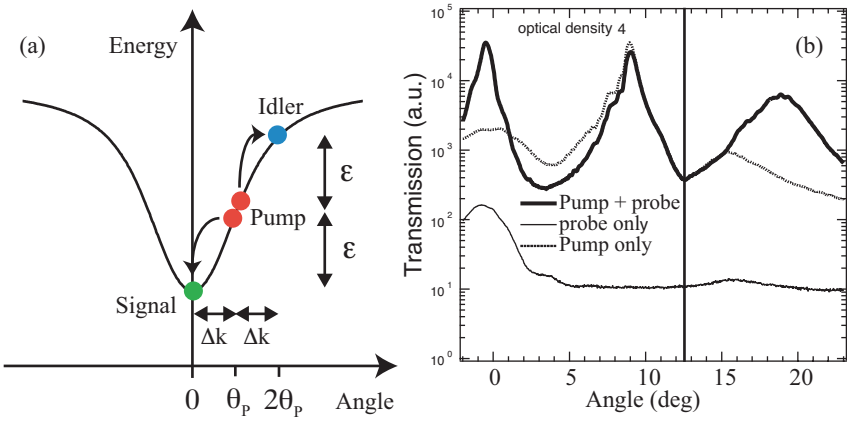


**Figure 2.8:** On panel (a) the angular dispersion of the lower polariton is shown. The polariton parametric scattering involves two pump polaritons scattering into a signal idler pair. On panel (b) transmission spectra are depicted showing signal, pump, and idler emissions. The bottom axis is the emission angle and the left axis the transmission intensity on a logarithmic scale.

### 2.5.2 Polariton parametric amplification

As in an optical parametric oscillator with a $\chi^{(2)}$- crystal, the signal, pump, and idler states are resonant with the resonator, which is in our case the microcavity. Since the states of the active medium (the excitons) are real and not virtual states, and strongly coupled to the cavity, the dispersion of the resonant cavity is modified by the excitons as explained in section 2.3. In contrast to a $\chi^{(2)}$- crystal oscillator, polariton parametric amplification is a $\chi^{(3)}$- process, since it involves two pump polaritons instead of one. As stated before, the lower polariton dispersion is the modified exciton dispersion with a dip around k=0 induced by the photon dispersion. Polaritons inside the dip are efficiently isolated from scattering with phonons. Inside the dip a stimulated parametric polariton-polariton scattering process conserving energy and in-plane momentum, is possible [99, 93, 111]. Indeed the particular shape of the lower polariton dispersion allows for such a scattering. The dispersion in the radiative region is depicted in Fig. 2.8. Polaritons with different in-plane wave vectors can be generated by illuminating the sample with resonant laser light impinging from different directions. At normal incidence polaritons with zero in-plane momentum are generated whereas for off-normal angles polaritons with finite in-plane momentum appear. For a special point near the inflection point of the dispersion called magic wave vector or magic angle, polaritons can be generated by a resonant pump laser beam and then scatter into a pair of signal and idler polaritons conserving energy and momentum. The polaritons scattering to the higher energy state - called the idler polaritons - take away the excess energy $\epsilon$ and momentum $\Delta k$ of the signal polaritons scattering down to the band bottom. The phase-matching condition for the scattering reads:

$$2E_{LP}(k_p) = E_{LP}(k_{\|} = 0) + E_{LP}(2k_p), 2k_p = k_s + k_i \tag{2.14}$$

The process can be stimulated creating a small amount of polaritons at $k = 0$ using

a weak probe beam at normal incidence.

This is shown on the right of fig. 2.8, where the angular resolved detection of the polariton emission is shown. If the pump beam alone hits the sample at the magic angle ($\simeq 10^\circ$ for the employed sample) we observe an emission around k=0 and also a broadly distributed angular emission at the higher angle idler states. When the probe is switched on, the signal and idler emission become strongly enhanced and the angular emission distribution of signal and idler become much sharper. At the same time the pump polariton reservoir is depleted as the emission from the pump polaritons is weakened in presence of the probe.

In general the phase-matching condition defined in equation 2.14 allows for an infinite number of signal-idler modes situated on an eight shaped region in k-space [30, 68]. Here we don't concentrate on this feature since all the experiments of the present thesis have been performed for the above configuration with the pump laser beam at the magic angle.

### 2.5.3 Theory of the parametric amplifier

As we have seen, in a standard OPO exploiting the $\chi^{(2)}$ non-linearity of a transparent non-linear crystal gives rise to parametric oscillation. In this section we want to derive the evolution equations for the polariton parametric amplifier [29] starting from the microscopic Coulomb interaction of the polaritons. In section 2.3 we introduced the linear Hamiltonian in the polariton basis (equation 2.11). We now want to develop the full Hamiltonian including the Coulomb interaction of the polaritons and the coupling to the external photon modes. After that we will draw the Heisenberg equations of motion for the signal, pump, and idler mode.

#### Hamiltonian of the system

To obtain the full Hamiltonian for the polaritons we need to add the coupling of the polaritons to external photons and their mutual interaction due to Coulomb interaction and the saturation of the exciton oscillator strength. The interaction of the polaritons and external photon modes will be described in the framework of the so-called quasi-mode approximation as described in reference [31]. According to the finite finesse of the cavity, the polaritons are coupled to a continuum of external radiation modes. The coupling is described by

$$H_{qm} = \int d\Omega \left\{ \sum_k g(\Omega) C_{\mathbf{k}} p^\dagger_{\mathbf{k}} \alpha_{\mathbf{k},\Omega} + h.c. \right\}, \tag{2.15}$$

where $\alpha^\dagger_{\mathbf{k},\Omega}$ and $\alpha_{\mathbf{k},\Omega}$ are the creation and annihilation operators for an extracavity photon with in-plane wavevector $\mathbf{k}$ and frequency $\Omega$. $g(\Omega)$ is a slowly varying function of $\Omega$, and describes the coupling between the cavity photon mode and the external photons [97]. When an external classical field is applied, $\alpha_{\mathbf{k},\Omega}$ can be replaced by its mean value, which corresponds to the classical value of the field.

The second ingredient needed for the full Hamiltonian is the interaction between the polaritons due to the Coulomb interaction and the saturation of the excitonic transition as described in reference [92]. In the experiments, we want to study, the pump only excites the lower polariton branch. The interaction Hamiltonian is thus written in the polariton basis, neglecting all terms containing the upper polariton operators $u^\dagger_{\mathbf{k}}$ and $u_{\mathbf{k}}$ [31]. The corresponding interaction Hamiltonian reads

$$H_{PP} = \frac{1}{2} \sum_{\mathbf{k},\mathbf{k'},\mathbf{q}} \frac{\lambda_X^2}{A} V^{PP}_{\mathbf{k},\mathbf{k'},\mathbf{q}}\, p^\dagger_{\mathbf{k}+\mathbf{q}}\, p^\dagger_{\mathbf{k'}-\mathbf{q}}\, p_{\mathbf{k}}\, p_{\mathbf{k'}}. \tag{2.16}$$

The effective interaction potential $V^{PP}_{\mathbf{k},\mathbf{k'},\mathbf{q}}$ reads

$$V^{PP}_{\mathbf{k},\mathbf{k'},\mathbf{q}} = \frac{6e^2}{\epsilon\lambda_X} X_{\mathbf{k}+\mathbf{q}} X_{\mathbf{k'}} X_{\mathbf{k'}-\mathbf{q}} X_{\mathbf{k}} + 2\frac{\hbar\Omega_R}{n_{sat}\lambda_X^2}(|C_{\mathbf{k}+\mathbf{q}}|X_{\mathbf{k'}} + |C_{\mathbf{k'}}|X_{\mathbf{k}+\mathbf{q}})X_{\mathbf{k'}-\mathbf{q}} X_{\mathbf{k}}. \tag{2.17}$$

$e, \epsilon, \lambda_X$, and $n_{sat}$ being the elementary charge, the dielectric constant of the cavity, the exciton Bohr radius, and the saturation density of the excitonic transition. The first term in 2.17 describes the contribution of the Coulomb interaction between excitons, whereas the second accounts for the saturation of the exciton oscillator strength. It is important to point out, that both terms are always positive, i.e. the interaction potential is repulsive. The saturation density for the excitons can be obtained corresponding to [92]

$$n_{sat} = \frac{7}{16}\frac{1}{\pi\lambda_X^2} = \frac{0.139}{\lambda_X^2} \tag{2.18}$$

and amounts to $8 \cdot 10^{10} excitons/cm^2$ for GaAs with $\lambda_X = 13\,nm$.
We have now described all of the components needed to express the full Hamiltonian

$$H = \sum_k E_{LP}(k) p^\dagger_{\mathbf{k}} p_{\mathbf{k}} + H_{PP} + H_{qm}. \tag{2.19}$$

**Equations of motion for signal, pump, and idler polarisation**

In principle, the Hamiltonian permits the deviation of the equations of motion for the polariton field operators. The next step towards obtaining the equations of motion is to make some approximations so the set of equations can be solved numerically. Most of the experiments on parametric scattering of polaritons are made in the stimulated regime. As stated before, the operator describing the external photon modes, can be replaced by their mean values. Furthermore we are working above the stimulation threshold. In this case, the contribution of the incoherent populations and the number correlations between signal, pump, and idler are negligible with respect to the coherent polarisation building up in the three modes [98, 102]. Thus, it is sufficient to investigate the mean values of the lower polariton operators at signal, pump, and idler.

Furthermore, the interaction of the polaritons is treated only to the first order. This is justified by the fact, that the pump mode is strongly occupied, and the signal and idler polarisation can be neglected compared to the pump. It is convenient to write the polarisation in terms of the rescaled polarisation $\mathcal{P}$ which is given by

$$\mathcal{P}_{\mathbf{k}} = \frac{\lambda_X}{\sqrt{A}}\langle p_{\mathbf{k}}\rangle, \tag{2.20}$$

where $A$ is the quantisation area.
The equations of motion in terms of $\mathcal{P}$ read:

$$\text{Signal:} \quad i\hbar\frac{\partial\mathcal{P}_0}{\partial t} = (\tilde{E}_0 - i\gamma_0)\mathcal{P}_0 + E_{int}\mathcal{P}^{\star}_{2k_p}\mathcal{P}^2_{k_p} + F_0(t) \tag{2.21}$$

$$\text{Pump:} \quad i\hbar\frac{\partial\mathcal{P}_{k_p}}{\partial t} = (\tilde{E}_{k_p} - i\gamma_{k_p})\mathcal{P}_{k_p} + 2E_{int}P^{\star}_{k_p}\mathcal{P}_0\mathcal{P}_{2k_p} + F_{k_p}(t) \tag{2.22}$$

$$\text{Idler:} \quad i\hbar\frac{\partial\mathcal{P}_{2k_p}}{\partial t} = (\tilde{E}_{2k_p} - i\gamma_{2k_p})\mathcal{P}_{2k_p} + E_{int}\ \mathcal{P}^{\star}_0\mathcal{P}^2_{k_p}, \tag{2.23}$$

where $P_0$, $P_{k_p}$, $P_{2k_p}$ are the mean lower polariton fields for signal, pump, and idler wave-vectors respectively and $E_{int}$ is the coupling energy due to polariton-polariton scattering potential. On the RHS of each of the three equations, the first term is the 'free term', *i.e.* the evolution of the polarization of signal, pump, and idler mode in absence of interaction with the other modes. The homogeneous k-dependent linewidth $\gamma_k$ determines an exponential decay rate of the signal ($\gamma_k$ is determined by the losses of polaritons through the cavity mirrors and non-radiative losses). Note that the energy $\tilde{E}(k)$ includes a renormalization due to the polariton-polariton interaction and therefore it is slightly higher than the energy $E(k)$ calculated in the absence of pump polaritons. The second term is the parametric scattering rate: for the signal (idler) it is proportional to the square of the pump polarization (*i.e.*, proportional to the pump intensity) and to the conjugate of the idler (signal) polarization. The symmetry between signal and idler equations reflects the fact that for each polariton scattering from the pump *down* to the signal there is another one scattering *up* to the idler and vice versa. This reflects the mutual classical correlation of the creation of signal and idler polaritons. The last term in the first two equations ($F_{0,k_p}(t)$) corresponds to the external driving electric field, *i.e.*, the temporal evolution of the pump and probe laser pulses.

### Other models of parametric amplification

Since the first model presented by Ciuti, different models have been developed starting from the Hamiltonian equation 2.19. The model presented contains the evolution of the polarisations of signal, pump, and idler and works in a regime, where a strong laser field is present at the pump and a weak laser field stimulates the scattering, i.e. it is applicable above the threshold for parametric amplification. When pump and/or probe intensity are adjusted far above threshold, second order scattering processes become important, i.e. for example the process $\{0, k\} \rightarrow \{-k, 2k\}$ occurs. In [101] experimental data evidencing such processes are shown and a steady state model describing the

data is developed. Another problem arises, when the pump intensity is strong: The first order polariton interaction reaches values, which are of the order of the splitting of the polariton modes. Savasta et al. have proposed a model addressing this problem, describing the polaritons interaction including second order interaction of excitons, i.e. the two exciton correlations [95, 94]. To model the spontaneous parametric scattering, it is not sufficient to look only at the mean polarisation in the system. The polariton field operators can be written in terms of the mean polarisation and an operator describing the quantum fluctuations around the classical value. Accounting for all possible correlations and polarisations, a system of 12 coupled equations of motion is found [98]. The model can be used to study the behaviour of the system when starting at very low pump intensity below threshold and successively passing the stimulation threshold for the scattering. It is indeed a challenging task to solve these 12 coupled equations. A similar, slightly less complex model is used to evaluate the quantum statistical properties of polaritons in spontaneous parametric scattering just below threshold [102]. In [30], a 2D-space of wavevectors is used to obtain the shape of parametric luminescence in k-space. The parametric process in [30] is seeded by extracavity photon modes.

### 2.5.4 Phase-relation between signal, pump, and idler

We want to study the phase relation between signal, pump, and idler. The parametric interaction of the polaritons is found in the second term of eq. 2.21. If we set the polarisation of the signal, pump, and idler to

$$P_j(t) = A_j(t) \cdot e^{-i(\omega_j t + \phi_j)} \tag{2.24}$$

with $A_j(t)$ being the slowly varying real amplitude of the polarisation $P_j(t)$, the second term in eq. 2.21 gives

$$-A_0(t)i\omega \cdot e^{-i(\omega_0 t+\phi_0)} = \frac{E_{int}}{i\hbar} A_{2k_p}(t) A_{k_p}(t)^2 \cdot e^{+i(\omega_{2k_p} t+\phi_{2k_p})} e^{-2i(\omega_{k_p} t+\phi_{k_p})}. \tag{2.25}$$

To satisfy 2.25 for any time $t$, the condition $-A_0(t)i\omega = \frac{E_{int}}{i\hbar} A_{2k_p}(t) A_{k_p}(t)^2$ has to be satisfied and we obtain

$$e^{-i(\omega_0 t+\phi_0)} = e^{+i(\omega_{2k_p} t+\phi_{2k_p})} e^{-2i(\omega_{k_p} t+\phi_{k_p})}. \tag{2.26}$$

Separating the frequency terms and the phase-factors $\phi_j$ we obtain

$$1 = e^{-i(2\omega_{k_p} - \omega_{2k_p} - \omega_0)t} \cdot e^{-i(2\phi_{k_p} - \phi_{2k_p} - \phi_0)}. \tag{2.27}$$

Due to the phase-matching discussed in section 2.5.2 the first factor equals 1 and we get the phase relation between signal, pump, and idler

$$2\phi_{k_p} - \phi_{2k_p} - \phi_0 = 0. \tag{2.28}$$

This phase relation has been derived from the equations 2.21 - 2.23 for the parametric amplifier. It is also valid for the spontaneous parametric scattering above threshold, when the signal and idler beams are coherent.

## 2.6 Definition of terms

### 2.6.1 Classification of processes

We want to define briefly the terms for the processes related to parametric amplification in transparent $\chi^{(2)}$ crystals and in a strongly coupled microcavity:

1. **parametric amplification in transparent, $\chi^{(2)}$ non-linear crystals,** also known as difference frequency generation. A pump wave with frequency $\omega_1$ hits a $\chi^{(2)}$ non-linear crystal in its transparency region together with a probe at frequency $\omega_2$. The probe stimulates the creation of a pair of photons at $\omega_2$ and $\omega_3 = \omega_1 - \omega_2$. $\omega_2$ and $\omega_3$ are called signal and idler waves. At the output of the crystal an idler beam ($\omega_3$) is obtained. The probe beam at $\omega_2$ is amplified, explaining the term parametric *amplification.*

2. **parametric fluorescence in a transparent, $\chi^{(2)}$ non-linear crystal:** In principle a similar process to the parametric amplification (1), but not stimulated by a probe beam. A pump photon at $\omega_1$ decays spontaneously into two photons of frequencies $\omega_2$ and $\omega_3$, where $\omega_2 + \omega_3 = \omega_1$. Signal and idler photons are entangled.

3. **parametric oscillation in a resonator containing a transparent $\chi^{(2)}$ non-linear crystal:** The spontaneous creation of a signal-idler photon pairs as in (2), when the $\chi^{(2)}$ non-linear crystal is placed in a resonator being resonant with one, two, or all three parametric modes. Below the threshold for the parametric oscillation correlated signal-idler pairs are created, whereas above threshold signal and idler are coherent beams.

4. **seeded parametric oscillation in a resonator containing a transparent $\chi^{(2)}$ non-linear crystal:** The same process as (3) with an applied probe beam seeding the parametric oscillation. There is parametric amplification of the probe.

5. **polariton parametric oscillation in a semiconductor microcavity:** Semiconductor microcavity resonantly excited by a pump laser beam. Signal and idler polariton pairs form corresponding to the phase-matching relation $2E_{LP}(k_p) = E_{LP}(k_{\|} = 0) + E_{LP}(2k_p)$. The analogy of this process is the optical parametric oscillator (3).

6. **polariton parametric amplification in a semiconductor microcavity:** Same as (5), but the polariton parametric scattering process is stimulated by

a weak probe beam [2]. The analogy of this process is the seeded optical parametric oscillator (4).

### 2.6.2 Characteristic times

All the processes investigated in this work have a characteristic timescale of the order of a few up to a few hundred picoseconds. We have to carefully define the different time parameters characterising the properties of polaritons and their interactions. In this work, the terms used in the framework of the formalism of optical and semiconductor Bloch equations [103, 53] will be employed:

- $T_1$ accounting for the population decay (diagonal elements of the density matrix).
- $T_2^*$ accounting for the coherence decay (off-diagonal elements of the density matrix)
- $\Gamma_{hom.}$ is the homogeneous linewidth of the resonance accessible by spectroscopic measurements:

$$\frac{\Gamma_{hom.}}{2\hbar} = \frac{1}{T_2} = \frac{1}{2T_1} + \frac{1}{T_2^*} \tag{2.29}$$

$T_2$ will be referred to as the coherence time in this manuscript.

The coherence time $T_2$ contains a contribution from the population decay time $T_1$ (or lifetime) for the given resonance, and the pure dephasing time $T_2^*$, which characterises pure dephasing mechanisms like interaction with phonons or carrier-carrier scattering. The microcavity polariton states, specially the lower polaritons are efficiently isolated from such pure dephasing mechanisms so that generally the pure dephasing time is very long compared to the population lifetime and the coherence time $T_2$ thus almost equals twice the population lifetime. The spectral linewidth of a resonance is proportional to the inverse of its coherence time.

In the present work we usually speak about the decay of intensities. If we speak in this case about a coherence time, we mean the coherence decay time of the intensity which equals half the coherence time of the polarisation. When the considered resonance is inhomogeneously broadened, the coherence time is the apparently measured coherence time $T_2'$, which is shorter than $T_2$ according to $\frac{1}{T_2'} = \frac{1}{T_2} + \frac{\Gamma_{inhom.}}{2\hbar}$.

[2] The term seeded parametric oscillation in a semiconductor microcavity would be more appropriate in analogy to the nomenclature for transparent non-linear crystals. The established term in the polariton community is however "polariton parametric ammplificaton".

# Chapter 3

# Coherent Control of Polariton Parametric Scattering

In this and the following chapter, we will study the coherence and dynamical properties of polariton parametric scattering. This chapter will focus on the coherence properties of polariton parametric amplification when the parametric scattering is stimulated by a weak probe. It is a well known property of seeded parametric oscillation in transparent $\chi^{(2)}$-crystals, that the signal, pump, and idler emission have a mutual phase relation, i.e. they are phase-coherent. The coherence of the polaritons during a stimulated parametric scattering process is conserved in the sense of equations 2.21-2.23 of the polariton parametric amplifier [29], and illustrated in equation 2.28.

The aim of this chapter is to show experimentally the phase coherence of signal, idler, and pump during the parametric polariton amplification process, using a coherent control technique.

The idea of coherent control pulse shaping techniques was first raised in the domain of physical chemistry [114]. Such techniques have allowed for the control of chemical reactions [6] and even for the control of the shape of electronic wavefunctions [116]. Coherent control of exciton dynamics in quantum wells [55] and quantum dots [14] have been demonstrated. The coherent manipulation of microcavity polaritons has been shown in [76] and [69], and the coherence time of the polaritons was measured [76].

## 3.1 Experimental Setup

The sample described in section 2.4.1 is cooled down in a cold finger cryostat or a helium bath cryostat to temperatures of $\simeq 10\,\mathrm{K}$ or $\simeq 2\,\mathrm{K}$ respectively. The experimental setup is an ultrafast pump double probe experiment and depicted in fig. 3.1. The excitation pulses are emitted by a mode-locked Ti:sapphire laser working with an 80 MHz repetition rate and a 150 fs pulse duration. The beam is divided into the pump and the probe. The pump beam passes a $\simeq 1\,\mathrm{meV}$ wide band pass filter and therefore has a duration of $\simeq 1\,\mathrm{ps}$. The pulses impinging on the sample at the off-normal angle of $\simeq 10°$, which corresponds to the magic angle for our cavity. The probe pulses pass a

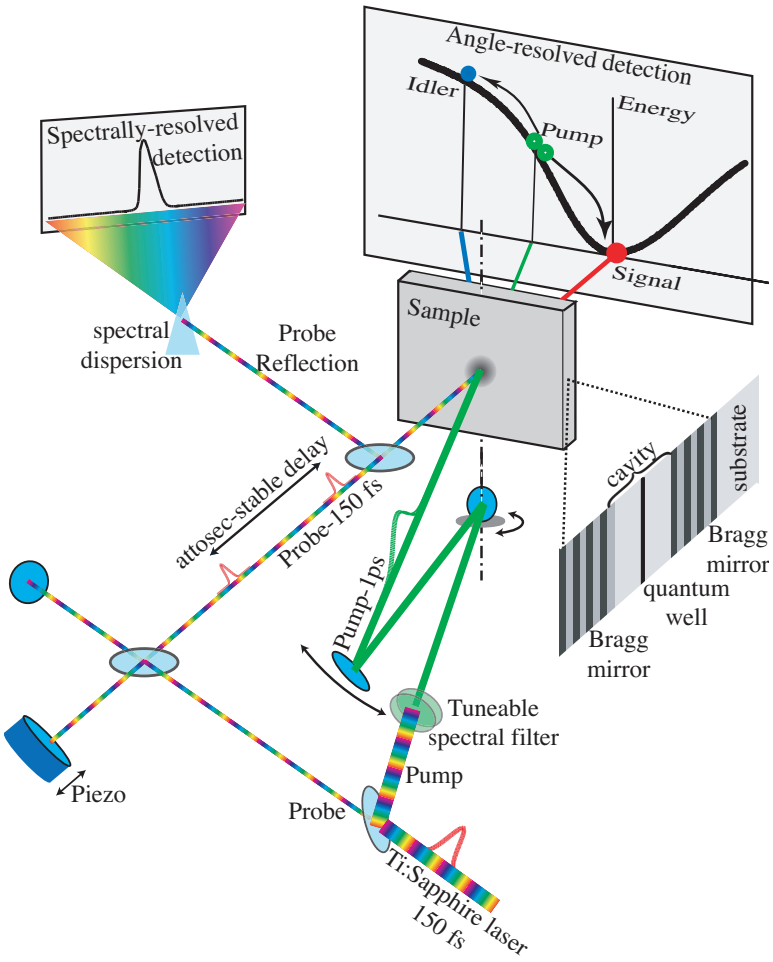


**Figure 3.1:** Experimental setup.

stabilized Michelson interferometer, and arrive at the sample at normal incidence. The relative delay and phase of the two probe pulses can be varied (see appendix A and [115]). The emission emitted at the rear of the sample was imaged onto a CCD camera with angular resolution to image the signal pump, and idler emission at the same time. The signal emission is also detected in time integration with spectral resolution.

## 3.2 Quantitative analysis

To study the coherence properties of the scattering, two kinds of measurements have been made in order to obtain information about the dynamics and the coherence of the scattering. First the experiment was performed using a single probe pulse by blocking one of the interferometer arms (see fig. 3.1). The transmission spectrum of the probe is shown in fig. 3.2 (a). If only the probe excites the sample we observe two transmission

peaks at the lower and upper polariton resonance. The lower polariton peak is at 1484.7 meV and the upper polariton at 1488.5 meV. The peak width corresponds to the 0.3 meV resolution of the spectrometer. The upper polariton peak is much less intense since the chosen position on the sample corresponds to a negative detuning between the photon and the exciton resonance of $\simeq$-1 meV (see fig. 2.5). When the pump beam is switched on and tuned to a $\simeq 10°$ incidence angle, the probe transmission is greatly amplified. The spectral position of the gain peak (0.1 meV blue-shifted with respect to the unperturbed lower polariton energy), the pump angle for maximum efficiency ($\simeq 10°$) and the threshold on the pump power (not shown) are in agreement with the model of the polariton parametric amplifier [29].

To get information about the dynamical behavior of the system the probe to pump delay has been scanned. The measurements are presented in fig. 3.2 (b). The pump hits the sample at time zero and the probe is delayed. The emission intensity has been normalized to the transmission intensity of a single probe pulse, whereas $I_{pump} = I_0$ is the approximate threshold intensity for the parametric amplification at delay 0. This measurement is sensitive to the temporal evolution of the pump polaritons since the amount of scattered polaritons is related to the number of pump polaritons remaining available for the scattering when the probe excites the sample. The decay of the time-integrated signal intensity with the probe delay becomes quicker with increasing pump density which can be attributed to the stronger spontaneous parametric scattering and stronger dephasing of the pump polaritons at high pump intensity.

With the pump-single probe experiments the dynamics of the scattering have been probed. In a second step we employ pump-double probe coherent control measurements which are sensitive to the coherence properties of the scattering. Finally we compare

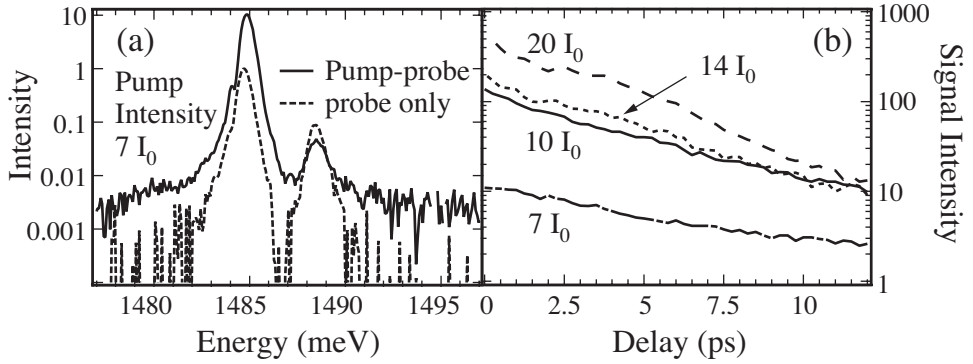


**Figure 3.2:** (a) Probe-Transmission spectra with (full line) and without (dashed line) pump excitation; one probe pulse only hits the sample. At the chosen position on the sample, the energy of the empty-cavity mode (1486.0 meV) is slightly lower than the bare exciton energy (1487.0 meV). (b) Evolution of the time integrated signal emission as the probe to pump delay is scanned for different pump density ($I_0$ is the pump density at which threshold for parametric amplification is reached, i.e. the probe intensity is amplified by a factor of 2. It corresponds to $\simeq 4 \cdot 10^{10} photons/(cm^2 pulse)$). The intensity has been integrated over the whole signal peak width of the LP emission and normalized to the transmitted signal intensity obtained with a single probe in absence of the pump.

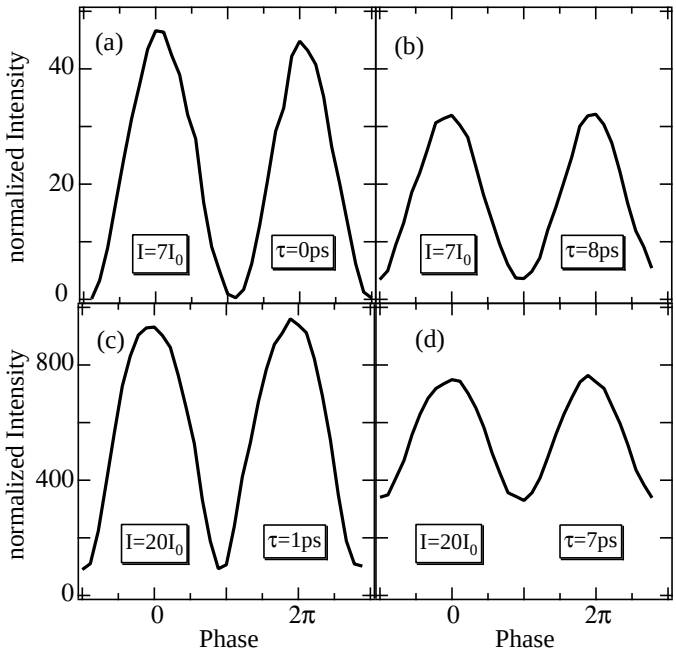


**Figure 3.3:** Results from a pump-two-probe experiment, showing time integrated signal intensities, measured in transmission versus the relative phase of the probe pulses. The signal intensity has been spectrally integrated over the whole peak width of the lower polariton emission. The signal intensity is normalised to the transmitted signal intensity obtained with a single probe in absence of the pump. The first probe pulse hits the sample at the same time as the pump, whereas the second is delayed by $\tau$. In (a) and (b) the pump power is $7I_0$ and $20I_0$ for (c) and (d).

the two measurements. In the coherent control pump-double probe measurements the excitation geometry is as follows (see also fig. 3.1): the pump and a first probe hit the sample at the same time and the second probe excites the sample at a delay time $\tau$ relative to the first one. The relative phase between the two pulses is stabilized and scanned using the interferometer. In fig. 3.3 the transmitted intensity normalized to the intensity of a single probe is depicted versus the relative phase of the two probes. The contrast of the interference fringes is defined as $C = (I_{max} - I_{min})/(I_{max} + I_{min})$ where $I_{max}$ and $I_{min}$ are the respective maximum and minimum intensities of the oscillations. On panel (a) and (b) the pump density is $7I_0$ whereas in (c) and (d) the density is $20I_0$. The second probe pulse is delayed with respect to the first one by $\tau$=0 (a), 8 ps (b), 1 ps (c), and 7 ps (d). At zero delay and low pump power (panel (a)), when the two probes perfectly overlap, the coherent control is complete and the emission goes to zero for destructive interference of the probes. This is due to optical interference of the probes before reaching the cavity. When the second probe is delayed by 8 ps (panel (b)) the oscillations nearly go to zero and the contrast is around 80 %. The phase imprinted onto the polaritons by the first probe is conserved until the second probe enters the cavity and until the scattering process is completed. When the pump power is risen to $20I_0$, the shape of the oscillations becomes slightly asymmetric especially for $\tau = 1ps$ (panel (c)). The minimum of the oscillaton is much sharper than the maximum. When the delay between the probes is $\tau = 7ps$ (panel (d)) the asymmetry of the oscillations is much weaker. The contrast is only about 40 % which is only half of the contrast measured in panel (b).

To map out the coherence properties in detail the coherent control experiment has been performed for various delays and pump powers. The measurements are shown in fig. 3.4. The total coherence time of the lower polariton at k=0 has been determined using only the two probe pulses in the coherent control configuration without the pump. The coherence time, which can be extracted from fitting a calculation for the contrast of the interference oscillations of two probe pulses without pump, is 10 ps[1]. When the pump is switched on and the power is adjusted to approximately 7 times the threshold intensity $I_0$ for the scattering, the contrast decays even more slowly than for the probes alone, evidencing a long lasting coherence of the polaritons [41].

Finally, in order to quantify the degree of coherence and to estimate the influence of non-radiative dephasing we now compare coherent control experiments, sensitive to the coherence, and single probe experiments sensitive to the dynamics of the scattering. We calculate the interference contrast as if the amplification dynamics of the scattering were completely independent[2]. This calculated contrast is shown together with the measured contrast in fig. 3.4.

[1]Under the condition of low excitation density and a homogeneous polariton linewidth, the polariton coherence time can be evaluated. The coherence time is then obtained by fitting the following expression to the lower polariton contrast at $k = 0$:
$C = \frac{I_{max}-I_{min}}{I_{max}+I_{min}} = \frac{(1+e^{-\frac{t}{\tau}})^2-(1-e^{-\frac{t}{\tau}})^2}{(1+e^{-\frac{t}{\tau}})^2+(1-e^{-\frac{t}{\tau}})^2} = \frac{2e^{-\frac{t}{\tau}}}{1+e^{-\frac{2t}{\tau}}}$, where t is the delay of the second probe and $\tau$ the polariton coherence time.

[2]We evaluate the mean amplitude $A(\tau)$ of the polarization at k=0 as the square root of the time integrated signal intensity $I(\tau)$ in a single probe experiment. The calculated contrast is then equal to $C = (|A(0) + A(\tau)|^2 - |A(0) - A(\tau)|^2)/(|A(0) + A(\tau)|^2 + |A(0) - A(\tau)|^2)$

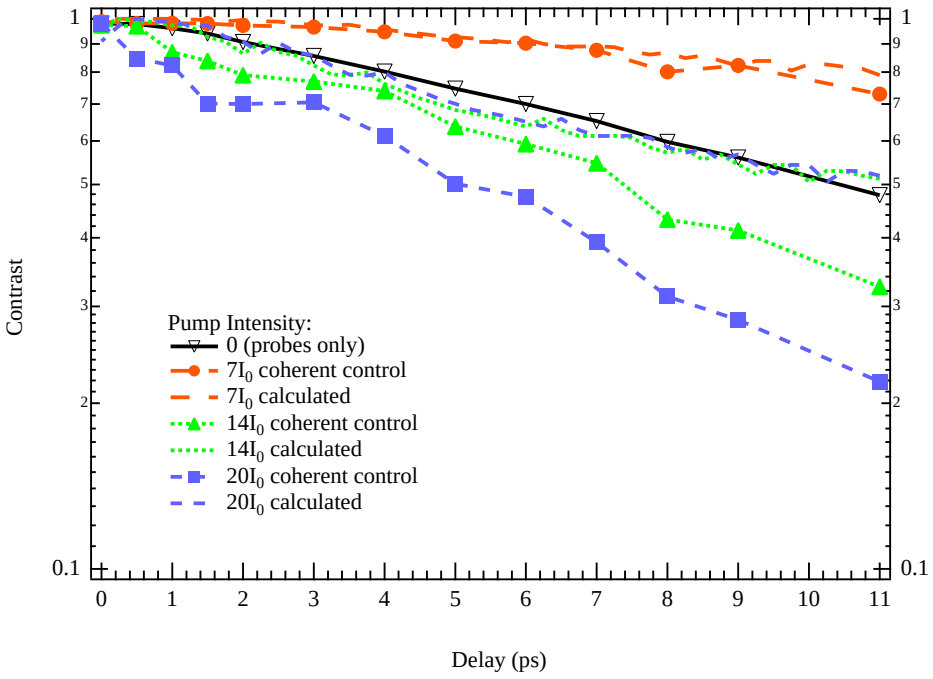


**Figure 3.4:** Contrast of coherent control oscillations versus the delay between the two probe pulses; the first probe pulse is synchronous with the pump. If $I_{max}$ and $I_{min}$ are the maximum and minimum values observed in the coherent-control oscillations, the contrast $C$ is defined as $C = (I_{max} - I_{min})/(I_{max} + I_{min})$. The incident pump photon densities are normalized to $I_0 = 4 \cdot 10^{10} photons/(cm^2 pulse)$ which is the density at which the stimulation threshold is reached. Each curve is measured for a different pump density, as indicated in the legend. The calculated contrast has been obtained from the experimental data shown in fig. 3.2 as explained in the text.

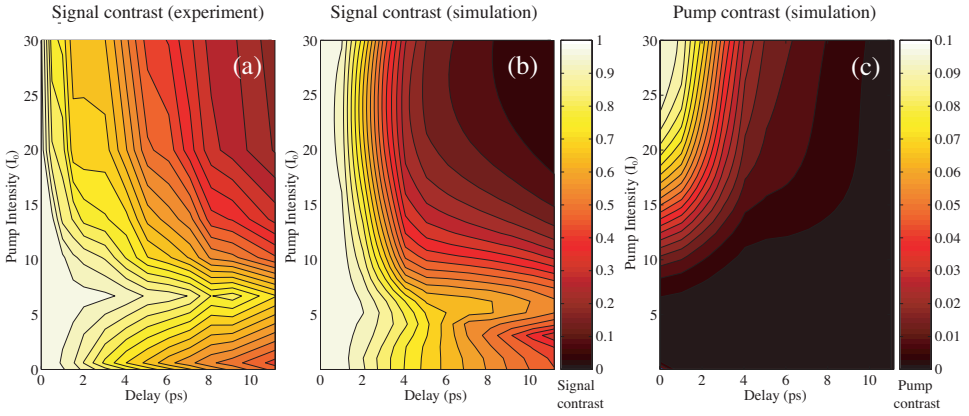


**Figure 3.5:** Signal contrast for the experiment (a) and the simulation (b) and simulated contrast of the pump (c). The left axes depict the pump power and the bottom axes the relative delay of the two probe pulses. The contrast is shown on a false color scale.

For the contrast at $I = 7I_0$ we observe that the measured and calculated contrast curves overlap and it can be concluded that in this low pump power regime the coherent control experiment can be understood in terms of two independent parametric scattering processes interfering with each other. This behavior occurs only if we assume that the signal polaritons have conserved their phase until the second probe arrives; i.e., the dynamics of the polaritons is purely coherent and limited only by the radiative dephasing.

When pump power rises to 14 and $20I_0$ the measured coherent control contrast presents a fast initial decay and deviates from the calculated contrast curve. The corresponding calculated contrast remains near the values of the bare lower polariton contrast. This demonstrates that for a pump power far above threshold the scattering processes are no longer independent. This can be interpreted in terms of excitation induced dephasing [26] or in terms of a depletion of the initial pump reservoir. Indeed the scattering rate into the signal and idler states is proportional to the square of the pump density (see eq. 2.21-2.23 and ref. [29]), and the amplification of the first probe depletes the pump polariton supply.

## 3.3 Modelling of the contrast behaviour

To understand the behaviour of the contrast, simulations using the model of the microcavity parametric amplifier [29] described in section 2.5.3 were performed. Corresponding to the double-probe coherent control experiment, in the modelling a pump and a first probe excite the sample at $t = 0$, whereas a second probe excites at a delay time $\tau$. Equations 2.21-2.23 are integrated numerically to obtain the intensities versus time of signal, pump, and idler. To obtain their time-integrated values, which permit a comparison with the experiment, the three intensities have been integrated over time again and - as in the experiment - the maxima and minima of the oscillations are extracted to calculate the contrast. To fit the decay of the contrast (fig. 3.4 solid line) at zero

pump excitation density, a homogeneous exciton and cavity linewidth of $98\,\mu eV$ has been inserted into the calculation. Fig. 3.5 shows the same contrast data as in fig. 3.4, but depicted on a contour plot (panel (a)). The simulated contrast is depicted on panel (b). As in the experiment, below threshold the contrast immediately decreases, then reaches a maximum above threshold and finally decays with rising pump power. How can these phenomena be explained? To obtain more information we examine the evolution of the pump polariton reservoir, which is the supply of the system. At high pump power we can expect that the pump polariton supply is significantly depleted. A good measure for this is the contrast of the fringes at the pump caused by the pump depletion. For high scattering rates the intensity arising from the pump transmission for constructive signal interference can be expected to be weaker than for the destructive interference (i.e. the oscillations at the pump are in anti phase). Also the contrast of the pump oscillations can be calculated putting the respective maximum and minimum emission intensities from the pump. The pump contrast is depicted in fig. 3.5 (c). At high pump power there is some significant contrast for small delays which means that in this regime the pump polariton reservoir is depleted. The contrast at the pump appears at the same time as when the signal contrast starts to decay more quickly above the contrast maximum. This evidences two things: first, the contrast decays very rapidly in the beginning because the scattering starts to saturate (the pump reservoir is depleted) and thus the scattering processes due to the two respective probes are no longer independent. Second, the poor contrast at longer delays indicates that the process is practically finished before the second probe pulse reaches the cavity at high pump power. If we locate the oscillations shown in fig. 3.3 in the contour plot of the signal and pump contrast we can explain this saturation effect stated earlier. Panel (c) in fig. 3.3 exhibits the highest degree of asymmetry between maximum and minimum and is located at a point in the contour plot where the pump contrast is about 0.07 (see fig. 3.5). Panel 3.3 (d) with the weaker asymmetry is at a point where the contrast is only 0.01. The shape of the two other oscillation plots (fig. 3.3 (a) and (b)) is symmetric and located at points on the pump contrast contour plot where the contrast is approximately zero.

## 3.4 Coherent control of signal, pump, and idler

For energy and momentum conservation, the parametric process has to involve both signal and idler polaritons [29], i.e. two polaritons from the pump being scattered into a signal-idler pair. The effects of the coherent control should therefore appear for signal, pump, and idler and not only in the normal direction, where the signal intensity is detected. Fig. 3.6 shows the angular pattern of the emission of the microcavity from the substrate side, opposite to the excitation side (all the spectrally-integrated emission is collected). The measurements are taken in the coherent control configuration, as a function of the relative phase between the two pulses. The pump power was approximately $I_p = 14I_0$. The coarse delay between the two phase-locked probe pulses is 2 ps. The incidence angle $\theta$ is measured with respect to the normal direction, so that the probe is transmitted around zero angle, while the pump is at $\theta \simeq 9^\circ$ The idler branch is

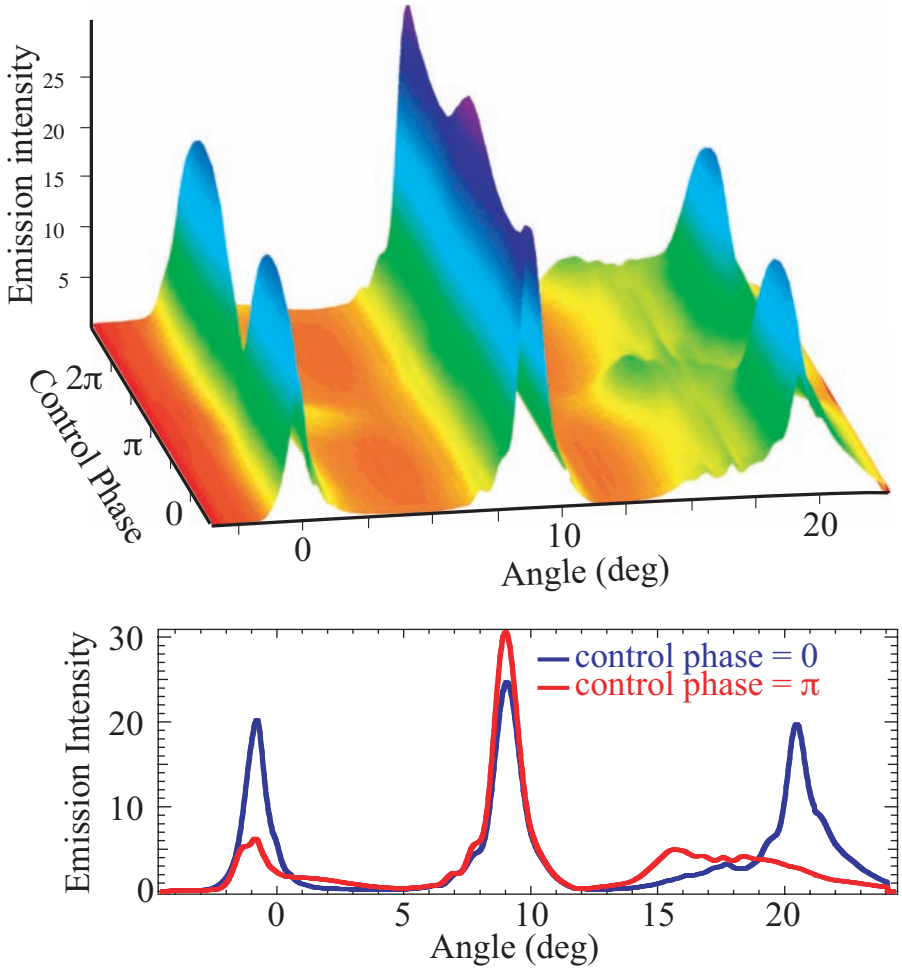


**Figure 3.6:** Angular pattern of the emission in transmission geometry as a function of the control phase. The delay between the two phase-locked probe pulses is 2 ps. The lower panel shows two sections of the surface plot corresponding to a constructive and a destructive control phase. The signal and pump emissions were attenuated (up to 14 deg) by four orders of magnitude with a neutral density filter in order to show the whole angular pattern on the same picture. In order to illustrate the effects of the coherent control on the pump beam, the probe density employed here was higher ($5 \cdot 10^8 polaritons/(cm^2 pulse)$) than that in the measurements in fig. 2, while the pump density was lower ($\simeq 10^{11} polaritons/(cm^2 pulse)$).

also visible at an angle slightly larger than twice the pump angle. This is because the parametric scattering conserves the in-plane momentum of polaritons, which is proportional to $\sin\theta$. Two sections of the surface plot are also shown to quantitatively compare the angular patterns obtained when the two probe pulses are in phase and out of phase. Signal and idler oscillations are in phase, i.e., when the coherent control maximises the emission in the probe direction, the idler also is maximized. Emission from the idler states is thus correlated to the signal emission. Simultaneously, the antiphase with the pump beam is clearly seen on fig. 3.6, as, for energy conservation, the polaritons which are not found in signal and idler branches have to be at the pump angle.

When the two probe pulses are in antiphase, the emission in the probe direction is strongly reduced and the polaritons at the pump angle decay spontaneously (see also fig. 2.8, right panel, dotted line), as in the absence of an external seed, when the parametric scattering can be started by the few pump polaritons that relax into the band bottom, generating an emission around the normal direction [111, 10, 100, 30]. For the measurements in fig. 3.6, the incidence angles of pump ($\simeq 9°$, instead of the optimal $\simeq 10°$ of fig. 3.2) and probe ($\simeq -1°$) have been chosen in order to distinguish the emission stimulated by the probe (occurring at $\simeq -1°$) from that occurring at $\simeq 1.5°$ after the "spontaneous" parametric scattering of the pump polaritons. The "spontaneous" parametric emission of the pump has a broad angular pattern and is correlated to an idler emission at $\simeq 17.5°$ Remarkably, when the second probe interferes constructively, the emission generated by the pump alone is strongly reduced. This directly confirms the pump depletion at $I = 14I_0$, which has also been shown in fig. 3.5.

## 3.5 Conclusions

In conclusion, we have demonstrated the coherent control of the polariton parametric scattering in a semiconductor microcavity. Thanks to the coherence and the stimulation effects in the parametric scattering of polaritons, weak sub-picosecond laser pulses may be used to control a very intense optical emission. Using simulations of the signal and pump contrast it has been shown that the decrease of the contrast at high pump power is due to the depletion of the pump polariton reservoir. The parametric scattering involves polaritons with three different wavevectors, so that the control pulse exciting the sample at normal incidence is able to control the occupation of polariton states with different momentum all over the dispersion. Microcavity polaritons are therefore a model system for studying Coulomb quantum kinetics, as they combine a very efficient interaction, needed for fast manipulation, with a low decoherence.

# Chapter 4

# Dynamics of polariton parametric scattering

In the previous chapter we presented time integrated measurements demonstrating the coherent control of parametric polariton scattering. It was shown that the employed probe pulses could serve to control the signal, pump, and idler emission. As an important feature of the parametric polariton emission it has been demonstrated, that the signal and idler emissions are correlated. In this chapter, we again use our resonant pump-probe setup to measure the emission dynamics of the signal in real time. In particular, we want to investigate the influence of the parametric nature of the scattering on its dynamics.

In the past, there have been studies on the dynamics of parametric polariton scattering both in the stimulated [46] and in the spontaneous regime [46, 68, 59], using momentum resolved streak camera detection [46, 68] or four-wave-mixing [59]. In the present study, we use an angle resolved streak camera setup to get an overview of the pump and signal dynamics and an ultrafast upconversion technique to investigate very fast features of the signal dynamics.

The chapter begins by discussing a measurement of the temporal emission pattern from the microcavity between signal and pump using a streak camera. The dynamical behaviour is monitored for a varying pump intensity. In section 4.2, the dynamical mechanisms in the polariton parametric scattering are discussed using the model [29] introduced in section 2.5.3. The simulations are compared to the measurements presented in section 4.1.

In section 4.3 the following fast dynamics features are investigated using an ultrafast upconversion setup: delayed build-up of the scattering (4.3.1), behaviour with pump and probe intensity (4.3.2), influence of the pump incidence angle (4.3.3), transient de-amplification (4.3.4), and the influence of the shape of the probe pulses (4.3.5). In section 4.4, the dynamics properties of the parametric oscillation in the spontaneous regime (without applied probe pulse) is analysed using an interferometer autocorrelation setup.

## 4.1 Experimental overview: Dynamics in k-space

To obtain an overview of the dynamics happening in k-space, we employed an angle resolved streak camera setup, as depicted in fig. 4.1. The sample is held in a cold finger cryostat at a temperature of $10\,K$. The sample is excited by the pump and probe pulses, the pump hitting the sample at the magic angle, the probe is at normal incidence at $k = 0$. The angular emission is collected in transmission by an objective at its focal distance $f$. The k-space we want to investigate, is located in the conjugated plane at distance $f$ behind the objective. This plane is imaged onto the entrance slit of the streak camera using a second lens. The angular range of the detection covers angles encompassing both the signal and the pump ($-5°$ to $15°$ ). The idler emission could not be time resolved as the idler intensity is about $10^4$ times weaker than the one of signal and pump (see fig. 2.8 in section 2.5.2). The time-resolution of the streak camera setup is approximately $5\,ps$.

Panel (a) of figure 4.2 shows the time-evolution of the signal and the pump in the spontaneous regime on panel (a) and (b). The pump impinges onto the sample at an angle of $10°$, which corresponds to the magic angle of the microcavity. For a delay of $10-16\,ps$, we observe a trace of polaritons emitting between the pump and $k = 0$. This can be attributed to pump polaritons which relax down the lower polariton dispersion by the emission of phonons. The polariton trace starts at about $10\,ps$ at an angle of $8°$ and reaches the signal state at $t \simeq 16\,ps$. The broad emission around the signal state reaches its maximum at $t \sim 20\,ps$. The emission intensity then decays corresponding to the polariton lifetime. The pump polariton emission shows a somewhat strange behaviour: During the decay of the pump intensity, the pump emission shifts from $10°$ at $t = 0$ to around $8°$ at $t \geq 30\,ps$. The whole angular peak shifts whilst conserving its angular width. Thus this cannot be explained by phonon interaction as for the polaritons scattering down to $k = 0$ implying that the shift must be due to a mechanism acting on the whole pump occupation. Such a mechanism could be for example a shift of the polariton dispersion [30] due to the excitonic blueshift or a reduction of the exciton oscillator strength. In both cases, the pump polariton states shift to higher angles (see fig. 4.3 and its caption), which is the opposite behaviour. The reason for the observed behaviour is probably that the pump polaritons relax under the emission of a second phonon species. This process must be less efficient than the one being responsible for the polariton trace between pump and $k = 0$.

On panel (b) of fig. 4.2 the temporal angular behaviour for the parametric amplification in the pump probe experiment is displayed. The probe hits the cavity at

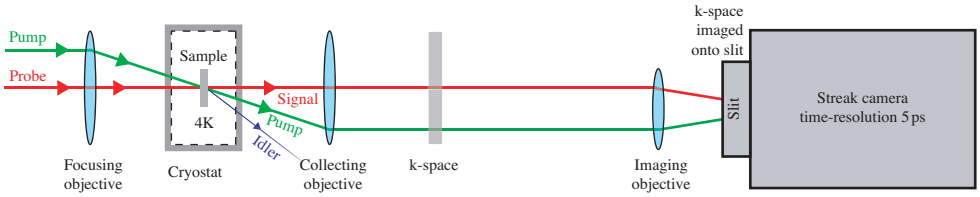


**Figure 4.1:** Streak camera setup.

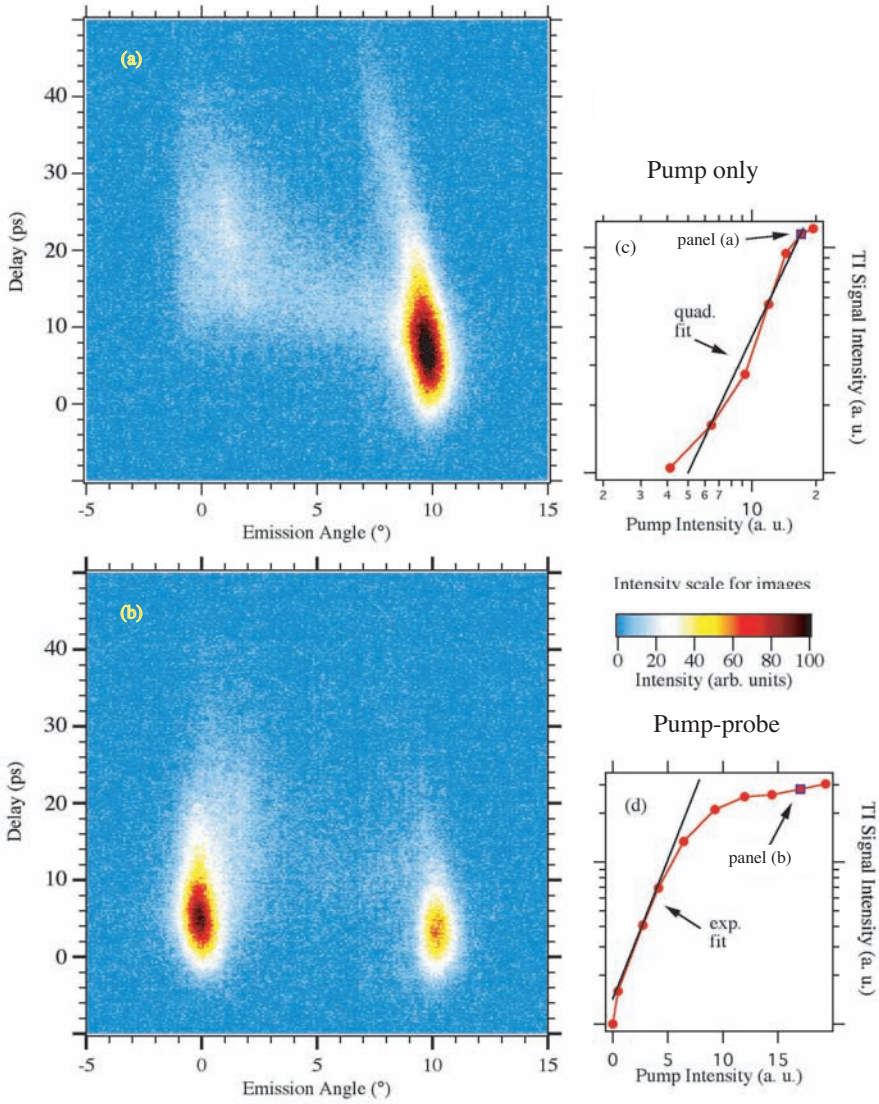


**Figure 4.2:** Images taken with the streak camera showing the evolution of k-space in time. The horizontal scale displays the emission angle, whereas the vertical shows the emission delay. The false colour intensity scales are the same for both panels. Panel (a) shows the angular and time-resolved emission when only the pump hits the sample. The lower panel (b) displays the evolution for the stimulated parametric amplification in the pump probe experiment. The time scale is consistent for all the streak camera measurements (fig. 4.2, 4.4, and 4.5). The zero of the scale has been set to the maximum of the transmitted probe curve in fig. 4.4 (no pump). The pump polariton density is $4 \cdot 10^{11}/cm^2$, and the probe polariton density to $3 \cdot 10^8/cm^2$. Panel (c) and (d) display the time-integrated signal intensity at $k = 0$, when the pump intensity is varied. The data has been obtained analysing streak camera measurements for different pump intensity.

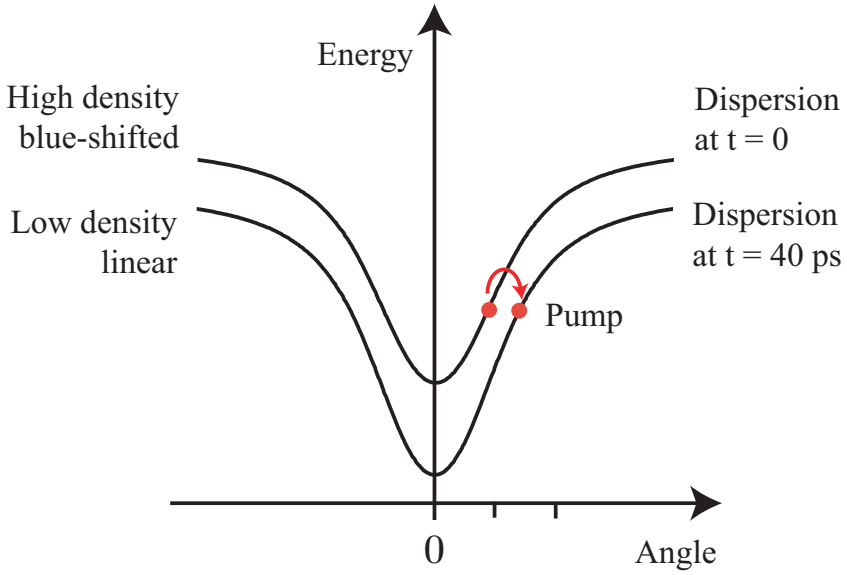


**Figure 4.3:** Schematic illustrating the polariton dispersion shift due to the excitonic blue-shift and the saturation of the exciton oscillator strength (the energy shift is exagerated). The blue-shift shifts the whole polariton dispersion to higher energy. It further increases the depth of the lower polariton dispersion around $k = 0$, since the Hopefield factor of the polaritons around $k = 0$ is smaller than the one for higher in-plane momentum states. The saturation of the exciton oscillator strength tends to decrease the lower-upper polariton splitting and should thus also shift the states inside the dip of the dispersion to higher energies. At $t = 0$ the re-normalisation is strongest. The pump polaritons are generated at the laser incidence angle. As the density decays, the dispersion shifts back to its linear value. The pump polaritons should thus shift to higher angles. This is the opposite behaviour to the one observed in the experiment.

normal incidence at zero delay. The pump-probe delay has been adjusted to obtain a maximum time-integrated signal intensity. The probe is immediately amplified. The emission intensity peaks around $t = 5\,ps$. The probe intensity then decays, since the pump polariton mode has been strongly depleted by the amplification (compare the intensity with panel (a)). The pump peaks at $t \sim 4\,ps$, $3\,ps$ earlier than in the spontaneous case (panel (a)), where no probe is applied. This indicates, that a strong amplification takes place even before the pump reaches its maximum. This observation is similar to what has been observed in reference [46]. For the spontaneous parametric scattering (panel (a)), an appreciable emission from polaritons relaxing from the pump mode is observed. In the stimulated case (panel (b)), the contribution of the phonon mediated relaxation of pump polaritons is much weaker (almost no emission between the pump and signal emission angle is observed), since a large amount of polaritons have already left the pump.

The angle and time-resolved measurements have been performed for a large number of pump intensities. The time integrated signal intensity obtained from the respective

time-resolved measurements are displayed on panel (c) for the spontaneous case and panel (d) for the stimulated case. To measure the time integrated signal emission, the emission intensity is summed for an angular range of $\theta = 0 \pm 0.5°$ and integrated in time. The blue squares on the time-integrated graphs are the data points corresponding to panel (a) and (b). The dependence of the time-integrated signal intensity on pump intensity depicted on panel (c) is quadratic. A quadratic dependence of the time-integrated signal intensity on the pump intensity indicates, that the signal is populated from a process involving two pump plaritons, in our case parametric scattering. The emission around $k = 0$ in the signal, initially started by the pump polaritons which have relaxed to the bottom of the dispersion, is weakly amplified due to the parametric scattering (the dependence of the time-integrated signal intensity on panel (c) is quadratic). On panel (d), we observe an exponential dependence of the signal intensity on the pump intensity, showing that the parametric scattering is stimulated by the polaritons generated by the probe. The measurement presented on panel (b) corresponds to a pump intensity far above threshold, where the signal intensity saturates. From the data presented on panel (c) and (d), we can thus conclude, that the threshold for self stimulated spontaneous parametric polariton scattering is much higher than for the stimulated amplification of a coherent signal polarisation excited by a weak probe pulse. The feature of the two different thresholds for the spontaneous and the stimulated parametric scattering will be addressed again in section 4.4.

In the following section, we analyse in quantitative detail the temporal behaviour of the stimulated signal emission at $k = 0$ when the probe is applied. To enable us to do this, the experiment presented here has been performed for series of different pump intensities.

### 4.1.1 Dynamics of the signal at $k = 0$

Images in the delay-wavevector plane similar to the ones shown in fig. 4.2, lower panel, have been analysed for different pump intensities. To obtain quantitative data, the emission at $\theta = 0 \pm 0.5°$ has been summed to obtain time-resolved signal intensity curves. Some examples of the obtained intensity versus time traces are shown in fig. 4.4. The black curve shows the signal intensity measured when the probe only excites the sample. The probe pulses excite the sample at $t = 0$. Due to the amplification, the signal starts to rise until a maximum is reached. After a maximum, the intensity of the signal decreases and the decay time finally approaches an exponential decay determined by the linear lifetime of $\sim 7\,ps$ of the polaritons at $k = 0$. At $I_{pump} = 4I_{th}$ the signal peaks at $t = 10\,ps$ whereas for higher pump intensities, at $I_{pump} = 14I_{th}$ for instance, the signal peaks at $t \simeq 6\,ps$. To enable a more complete analysis, a number of temporal traces have been stacked together to form a contour plot.

Figure 4.5 shows the temporal evolution of the parametric scattering when the pump intensity is varied. The peak of the signal emission remains constant from $1 - 7\,I_{th}$, at a delay of $\sim 11\,ps$. Above $7\,I_{th}$, the delay decreases slowly from $11\,ps$ to $\sim 4\,ps$ at $19\,I_{th}$. This behaviour already reported in [59] is due to the fact that the scattering rate into the signal becomes non-linear with rising pump intensity. At the same time the scattering depletes the pump reservoir and the maximum is reached at earlier times.

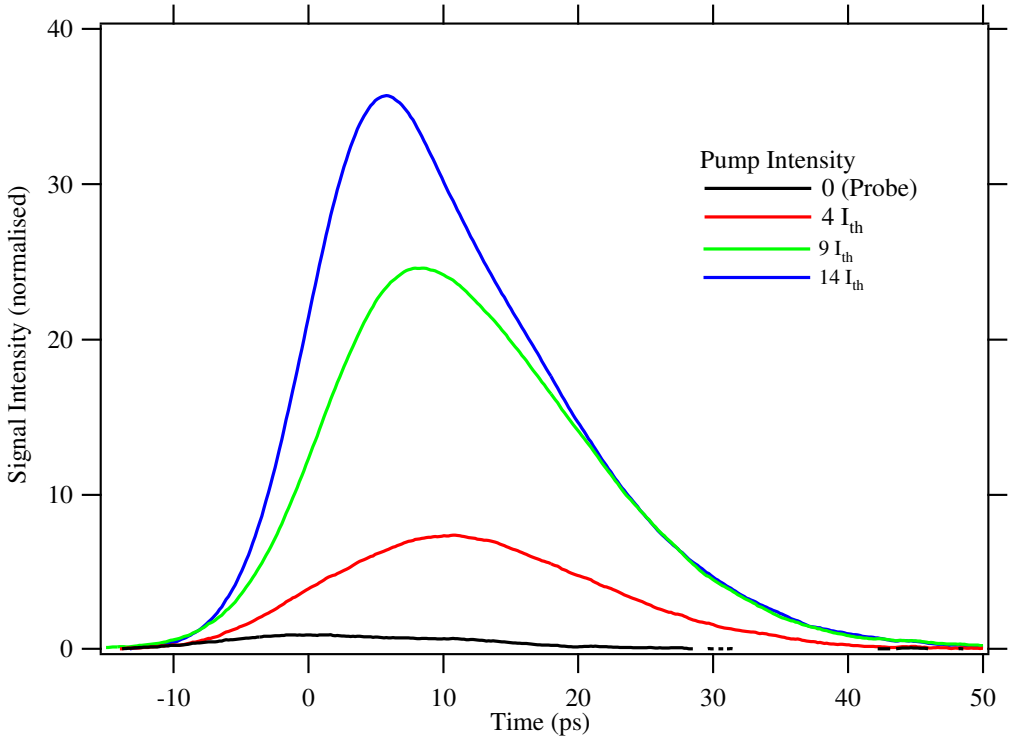


**Figure 4.4:** Time resolved signal emission for three different pump intensities ($4I_{th}$, $9I_{th}$, $14I_{th}$), and for the probe alone. The threshold pump intensity $I_{th}$ is the pump intensity, where the time integrated probe polariton intensity is amplified by a factor of 2. The zero of the timescale has been set to the moment when the transmitted probe intensity (without pump) reaches its maximum. The pump probe delay is zero. For the highest employed pump intensities the signal emission seems to start at negative delays. This is an experimental artefact and due to the time-resolution of $\simeq 5\,ps$ of the streak camera. The pump polariton density at threshold is $\simeq 2 \cdot 10^{10}/cm^2$, and the probe polariton density is $\simeq 3 \cdot 10^8/cm^2$.

The termination of the parametric scattering is reached at $t \sim 20\,ps$, when the polariton intensity obeys an exponential decay governed by the lifetime of the polaritons at $k = 0$, and no more parametric stimulation occurs. The right panel of figure 4.5 shows the dependence of the time integrated signal intensity on the pump intensity, also shown in fig. 4.2, panel (d). The signal of the time-integrated intensity is normalised to the intensity when only the probe pulse is present. The dashed line is an exponential fit to the intensity curve which fits well for pump intensities up to $7\,I_{th}$. In fact, this coincides with the pump intensity, where the peak of the timeresolved signal intensity starts to shift to earlier delays because of the pump depletion. The pump depletion is thus attributed to gain saturation.

Thus far a number of dynamical features have been investigated. Having demonstrated and discussed a number of dynamical features of the cavity polaritons, in the following section we will place these results within a theoretical framework. In order to do this we will qualitatively compare the measured data with the temporal curves

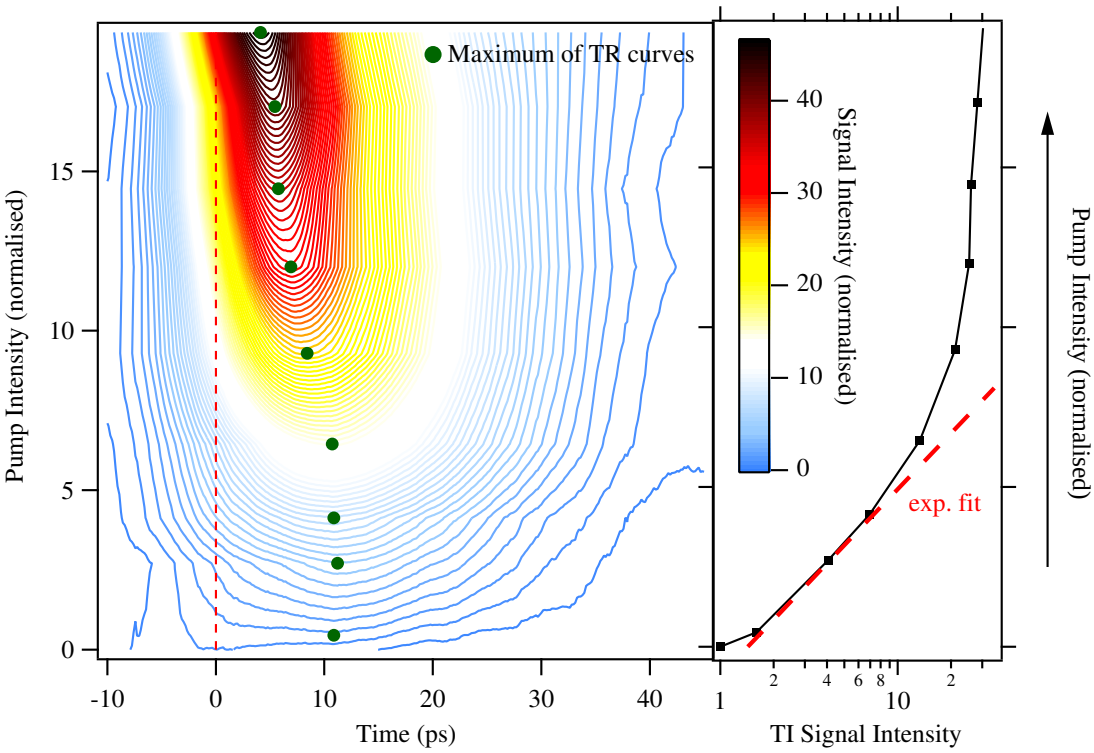


**Figure 4.5:** Evolution of the dynamics of the signal intensity with pump intensity. The image shows a contour plot of the temporal shape of the signal emission intensity versus the incident pump intensity (vertical axis). The pump intensity is normalised to the threshold intensity of the parametric amplification, where the threshold is defined, as the pump intensity where the signal is amplified by a factor of 2: This definition is used for all the pump probe experiments in this thesis. The signal intensity given by a false colour scale is normalised to the intensity of the probe at $t = 0$. The green points display the delay where the time-resolved curves used to build the image have reached their maximum. The red dashed line shows $t = 0$. For the highest pump intensities employed the signal emission seems to start at negative delays. This is an experimental artefact and due to the time-resolution of the streak camera ($\sim 5\,ps$). The right hand panel of the figure shows the dependence of the time integrated signal intensity together with an exponential fit. The pump polariton density at threshold is $\simeq 2 \cdot 10^{10}/cm^2$, and the probe polariton density is $3 \cdot 10^8/cm^2$.

obtained using the rate equation model [29], and carry out the dynamical properties of the parametric polariton scattering.

## 4.2 Modelling of the parametric scattering

In section 2.5.3 we have introduced a model [29] which describes the parametric interaction of the signal, pump, and idler polaritons with three coupled equations describing the evolution of signal, pump, and idler (see equations 2.21-2.23). This simple model has already shown a good fit with the behaviour of the signal contrast, as shown in section 2.5.3. The idea of the modelling in this section is to obtain a qualitative understanding of the dynamics of the parametric scattering. For all the simulations shown in this chapter, the pump excites with a wavevector $k_p$ corresponding to the magic angle of 9.5°. The signal is at $k = 0$ and the idler at $k = 2k_p$. To enable an easy comparison of the decay of the intensity, the linewidth of signal, pump, and idler are all set to $0.05\,meV$ ($\gamma_0 = \gamma_{kp} = \gamma_{2kp} = 0.05\,meV$)[1]. All the intensities in the simulation are intensive quantities normalised per unit surface for an infinitely large spot. The pump intensity, which determines $F_{pump}$ is given in terms of $I_{th}$, the intensity at which the time integrated signal intensity is amplified by a factor of 2. The probe intensity governing $F_{probe}$ is adjusted to give an intra-cavity intensity of $\sim \frac{1}{55} I_{pump}$ at $I_{pump} = I_{th}$.

### 4.2.1 Dynamics of Signal, Pump, and Idler

Figure 4.6 shows the calculated temporal evolution of signal, pump, and idler together with the non-amplified probe. The pump and probe pulses excite the sample at $t \sim 0$ to give a maximum polariton intensity inside the cavity at $t = 0$. The black curve displays the dynamics of the signal, when only the weak probe hits the cavity (no parametric interaction). It peaks at $t = 0$ and decays with a $\tau = 6.6\,ps$ decay time corresponding to its linewidth of $2\gamma_0 = 0.1\,meV$. The signal (red) decays until $t = 0.9\,ps$ and rises until its emission maximum at $t = 7.6\,ps$. The idler, initially having zero intensity, rises until its maximum intensity at $t = 9\,ps$, note this is slightly later than the signal maximum. From $t \sim 15\,ps$, the shapes of both signal and idler are very similar and from $t > 20\,ps$ the signal, pump, and idler curves are parallel since they decay both with their lifetime of $\tau_0 = \tau_{2kp} = 6.6\,ps$. This indicates, that at that time the scattering is concluded and no more parametric interaction occurs.

We now want to focus on the early time behaviour of the amplified signal. After the probe excitation, the signal intensity diminishes, and then rises together with the idler. As discussed in section 2.5, the creation of signal and idler polaritons by parametric scattering from the pump is correlated. A polariton at the signal necessitates a polariton at the idler and vice versa. We now want to check this correlation property of parametric amplification in the modelling. To do this, we subtract the time resolved intensity of the probe from that of the amplified signal (curve "(Signal)-(Probe)"). What we observe is that the curve fits the evolution of the idler perfectly, showing that the stimulated part of the signal emission is perfectly correlated. This correlation indicates that the system goes from the initial state of two pump polaritons into the final state of a signal plus an idler polariton. The initial decay of the signal intensity curve is attributed to

[1] In a real cavity, the linewidth is different for signal, pump, and idler, since the cavity and exciton linewidths are different.

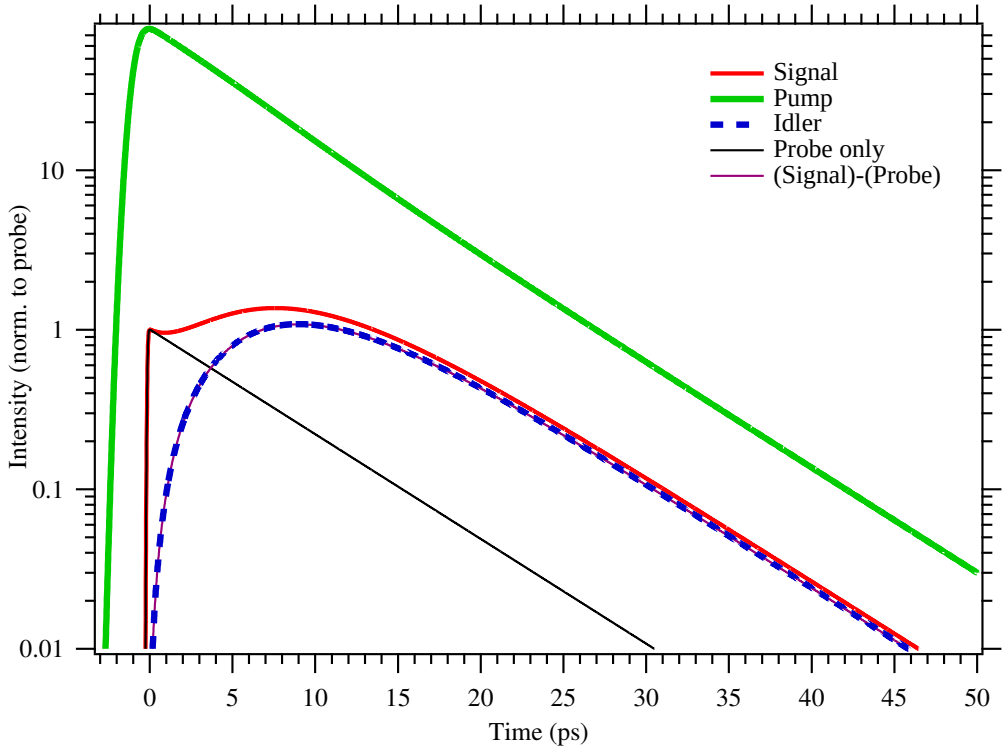


**Figure 4.6:** Modelled signal, pump, and idler real-time dynamics at a pump intensity $I_p = \sqrt{2}I_{th}$. Pump and probe excite the sample at delays, such that the polariton intensity peaks at $t = 0$ (The temporal shape of pump and probe is Gaussian. Since the polariton intensity is the integral of the pulse decaying with a decay rate $\gamma$ (third and first term in eq. 2.21 and 2.22), the maximum polariton intensity is reached after the pulse maximum. The excitation is temporally the same for all the simulations presented in this chapter.). The linewidth of the exciton and the cavity resonance are both set to $0.05\,meV$, so that $\gamma_{Signal} = \gamma_{Pump} = \gamma_{Idler} = 0.05\,meV$. The non-amplified probe is depicted in black. All intensities are the polariton intensities inside the cavity, so that the signal, pump, and idler intensities can be directly compared.

the fact that we only stimulate "one half" of the final state. The signal intensity decays until the loss rate is compensated by the polaritons scattering from the pump into the signal state.

To complete our understanding of the parametric short time phenomena, we discuss directly the coherent parametric interaction contained in equations 2.21-2.23. The scattering rate into the signal (second term in equation 2.21) reads:

$$\left(\frac{\partial P_0}{\partial t}\right)_{par} = \frac{E_{int}}{i\hbar} P^{\star}_{2k_p}(t) P^2_{k_p}(t), \tag{4.1}$$

The scattering rate into the idler corresponds to

$$\left(\frac{\partial P_{2k}}{\partial t}\right)_{par} = \frac{E_{int}}{i\hbar} P_0^{\star}(t) P_{k_p}(t)^2. \tag{4.2}$$

The dynamical equation 2.23 for the idler polariton field can be formally integrated, giving the following analytical result [31]:

$$P_{2k_p}(t) = \frac{E_{int}}{i\hbar} \int_{-\infty}^{t} dt' P_0^{\star}(t') P_{k_p}^2(t') e^{-\frac{i}{\hbar}(\tilde{E}_{2k_p}^{LP} - i\gamma_{2k_p})(t-t')}, \tag{4.3}$$

where $\tilde{E}_{2kp}^{LP}$ is the renormalised idler polariton energy and $\gamma_{2kp}$ the corresponding broadening. By inserting Eq. 4.3 into Eq. 4.1, we obtain the expression for the signal parametric scattering rate in terms of the signal and pump polariton fields, i.e.:

$$\left(\frac{\partial P_0}{\partial t}\right)_{par} = \left(\frac{E_{int}}{i\hbar}\right)^2 \int_{-\infty}^{t} dt' K_{par}(t,t') P_0(t'), \tag{4.4}$$

where the *parametric memory* kernel $K_{par}$ reads

$$K_{par}(t,t') = P_{k_p}^{\star 2}(t') e^{+\frac{i}{\hbar}(E_{2k_p}^{LP} + i\gamma_{2k_p})(t-t')} P_{k_p}^2(t). \tag{4.5}$$

Equation 4.4 shows that the rate of pump scattering into the signal mode is proportional to the signal field itself, i.e. the scattering is stimulated. However, the stimulation is not instantaneous, because the stimulated scattering rate depends on the value of the signal field at all times $t' < t$. This memory effect takes place because the parametric stimulation requires the coherent and correlated build-up of the signal and idler fields [31]. The initial decay of the signal intensity is the manifestation of the parametric memory in our modelling. An instantaneous exponential rise of the signal could only be achieved if the parametric memory kernel were to be [81] $K_{par}(t,t') \propto \delta(t-t')$, i.e. not dependent on its history.

We now want to study the influence of a changing pump intensity on the dynamics. Signal, pump, and idler evolutions are displayed on panel A-C of fig. 4.7. The pump intensity is changed between $0.5I_{th}$ and $4I_{th}$. The pump intensity has the folowing influence on the signal, pump, and idler dynamics:

- At $I_{pump} = 0.5I_{th}$, the signal is weakly amplified (panel A) and it is difficult to distinguish it from the probe, as displayed in fig. 4.6. At higher pump intensity (2 and $4I_{th}$), the signal shows a peak, which shifts to earlier times with increasing pump intensity.
- The idler (panel C) has less than 10 % of the signal intensity at $I_{pump} = 0.5I_{th}$. For increasing pump intensity, it approaches the signal intensity. The temporal shapes of signal and idler also become similar. In fact, the higher the pump intensity, the larger the number of scattered polaritons and the smaller the relative contribution of the external probe to the signal intensity.

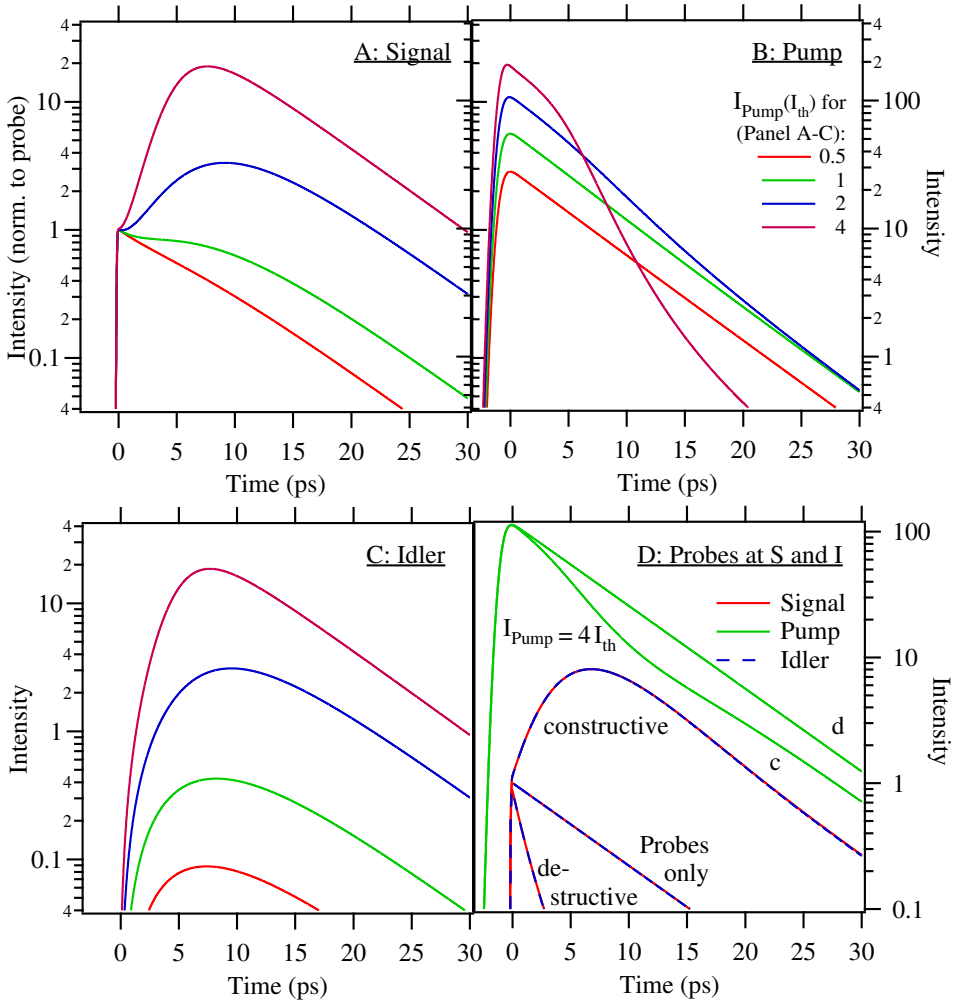


**Figure 4.7:** Signal, pump, and idler real-time evolution for different pump intensities (panel $A$, $B$, and $C$). All the intensities are normalised to the signal intensity at $t = 0$ without pump. Panel $D$ displays the evolution for signal, pump, and idler at a pump intensity of $2I_{th}$, when probes are applied at both the signal and the idler. Since the scattering is phase-coherent, the relative phases of the two probes have to be adjusted to obtain a constructive or destructive interference. The upper pump curve, $d$, depicts the destructive case, whereas the lower one corresponds to the constructive interference of signal and idler probe, where the pump is depleted.

- The pump mode (panel B) shows a mono-exponential decay at low intensity governed by the polariton lifetime. At higher pump intensities, the pump is strongly depleted, as already discussed in section 3.3. The depletion of the pump is clearly demonstrated in the experiment and displayed in fig. 4.2, lower panel, and it has also been reported in references [59, 46].

The signal and idler equations 2.21 and 2.23 are symmetric with respect to the

pump equation 2.22. In the previous simulation and in the experiments we apply a probe only to the signal but not to the idler. As a consequence, the signal and the idler are unbalanced (see panel A and C). On panel D, a simulation is shown, where probes are applied to both signal and idler. The parametric amplification is phase coherent, which is shown in section 2.5.4, equation 2.28.

To obtain constructive interference in the simulation in fig. 4.7, panel D, eq. 2.28 must be satisfied and for destructive interference, a phase factor of $\pi$ was added to the signal or the idler probe to obtain $2\phi_{k_p} - \phi_{2k_p} - \phi_0 = \pi$. When the two probes are constructive, i.e. the final signal-idler state is stimulated symmetrically, the signal immediately rises exponentially demonstrating instantaneous final state stimulation. The simulation shows, that indeed the final state is a signal-idler polariton pair, a fact which is of the same origin as the entanglement of signal-idler pairs below the stimulation threshold demonstrated in references [96, 77]. The signal idler curves for the case of destructive interference clearly shows that signal and idler can almost be completely de-amplified due to the parametric interaction. The whole process can be interpreted as superposition of two independent parametric scattering processes, stimulated by the signal and the idler probe respectively. It demonstrates a coherent control in theory with phase-locked probe pulses at signal and idler. It is somehow similar to the coherent control discussed in chapter 3, with the difference that one of the probes is at the idler. Putting one probe at the signal and another at the idler would be a complex experimental task. This experiment has been performed for a $\chi^{(2)}$ non-linear crystal parametric amplifier in reference [63].

### 4.2.2 Behaviour with the pump intensity

The previous section discussed the fundamental features of the time resolved emission as calculated theoretically. In the following, we compare the calculated signal dynamics to the measurements presented in fig. 4.5. The simulation was done for varying pump intensities between $I_{pump} = 0$ and $I_{pump} = 6I_{th}$ for the same simulation parameters as before and the results are shown in fig. 4.8.

The left panel shows an image plot of the signal intensity dynamics, when the pump intensity is varied. The right panel displays the time-integrated signal intensity. We observe the following features:

- Just above threshold, the delay of the emission maximum in the signal curves grows from $4.9\,ps$ to about $9.4\,ps$ at approximately $2I_{th}$. This is in contrast to the measurement (fig. 4.5), where the delay of the maximum remains constant up to $7I_{th}$. From $I_{pump} = 2I_{th}$, the delay diminishes to $6.2\,ps$ at $8I_{th}$. The initial augmentation of the delay can be understood as follows. For rising pump intensity, the time at which the pump density becomes too small to maintain the scattering increases. Consequently, the signal intensity peaks later. From about $I_{pump} = 2I_{th}$ a new behaviour sets in. As displayed in fig. 4.7, panel B from this intensity an appreciable depletion of the pump starts. The maximum of the signal intensity curves indicate the point, where the rate of scattered polaritons from the pump to the signal equals the cavity loss rate, which itself is proportional to the signal intensity. As the signal becomes more intense, this occurs earlier and

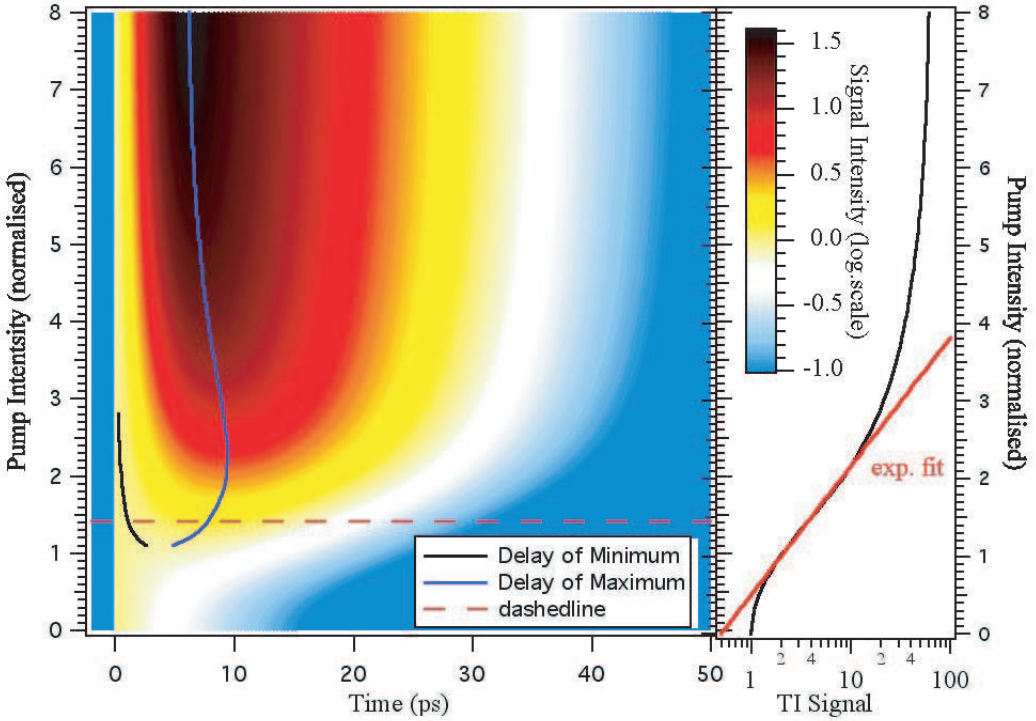


**Figure 4.8:** Contour plot of the time evolution of the signal versus the pump intensity. The colour scale is the logarithmic scale of the signal intensity, where zero corresponds to the intensity of the probe at $t = 0$. The dashed line at $I = \sqrt{2}I_{th}$ indicates the location of the signal curve shown in fig. 4.6. The black curve represents the delay of the minimum of the signal curve after the probe has hit. The blue curve indicates the delay at which the maximum of the signal emission appears. The panel on the right shows the time integrated signal intensity versus the pump intensity. It follows over about one decade an exponential behaviour.

consequently the maximum occurs earlier. Qualitatively this corresponds to what has been observed in fig. 4.5. However, the variations of the delay in the observed intensity interval are much stronger in the simulation.

- The minima in the signal curves (black curve, left panel) occur earlier with rising $I_{pump}$ and even disappear at $2.8\, I_{pump}$. The minimum occurs, when the scattering rate from the pump stimulated by the idler overcomes the cavity loss rate. With rising pump intensity the scattering rate grows. The cavity loss is thus overcome at earlier times [109]. Above $2.8 I_{th}$, there is no minimum, since at $t = 0$, the scattering rate into the signal is already larger than the cavity losses.

- The time-integrated signal intensity displayed on the right panel, grows exponentially with pump intensity. The exponential rise is illustrated by the fit and is applicable from $I_p \sim 0.7$ to $\sim 2.2\, I_{th}$, i.e. over a decade in signal intensity. Above $I_{pump} = 2.2\, I_{th}$ the intensity of the signal saturates due to the pump depletion as discussed before and already shown in section 3.3. This intensity roughly coin-

cides to that where the peak in signal intensity shifts to smaller values. The initial exponential rise followed by a saturation is clearly observed in the experimental data presented in figure 4.5.

We summarise, that the delay of the emission maximum as well as the exponential dependence and the saturation behaviour of the signal intensity on the pump intensity is qualitatively reproduced by the model.

### 4.2.3 Limits of the model

To conclude the modelling presented, we discuss the limitations of the model [29].

- The model considers the interaction of three wavevectors only. Signal, pump, and idler modes are thus respectively described by plane waves of infinite dimensions. This clearly does not correspond to the conditions in the experiments, in which finite spot size lasers with a gaussian intensity distribution are used [8].

- The model treats the polariton interactions to lowest order. Especially at high pump field intensities also the signal and idler intensities become strong and higher order scattering mechanisms set in [101]. The dynamical solution of the parametric modes in presence of second order mechanisms appears however a very complex task (the equations in [101] are solved for the steady state).

- In stimulated parametric scattering experiments, the probe and the pump wavevectors determine the idler wavevector. The conversion of two pump polaritons into a signal-idler pair conserves energy ($2E_{k_P} - E_0 - E_{2k_p} = 0$). The model satisfies this condition only at the magic angle and in the degenerate regime (signal, pump, and idler at $k = 0$). When the system oscillates slightly away from the angular resonances, the model [29] fails. A model describing the system oscillating outside the angular resonances has been developed in reference [9] and is used to reproduce bistability effects in parametric scattering.

- The exciton interactions as described in reference [92] lead to very strong renormalisation of the polariton dispersion. At some point, the magnitude of the renormalisation becomes of the order of the polariton splitting. This happens in the simulations at intensities between 4 and 8 $I_{th}$. A more adequate description of the polariton interaction would thus be required. Such a model including many-body effects and correlation between excitons has been developed by Savasta and co-workers in [95]. Their model works particularly well for cavities with large polariton splittings.

- The model treats the cavity without accounting for disorder related effects for example, thickness fluctuations of the quantum well. In reference [46] it has been shown, that disorder in the quantum well can strongly influence the dynamics of the scattering: In a strongly disordered cavity, the delay of the maximum signal emission intensity remains almost constant, whereas for a very homogeneous sample the delay shifts to earlier time at high pump intensity. In our case, the cavity

appears to have a very weak disorder (the signal maximum shifts to earlier time in fig. 4.5) and this problem seems thus less important for the cavity investigated here.

Concluding, despite the simplicity and the limitations of the theoretical model used here, it permits a qualitative understanding of several features observed with our streak-camera setup. However this setup has a timeresolution of $5\,ps$ and does not allow for the observation of the short time phenomena observed in the modelling. In the next section we will study the short time phenomena using an upconversion setup with a time-resolution of the order of $200\,fs$.

## 4.3 High resolution upconversion measurements

The upconversion setup is shown in fig. 4.9. Pump and probe are focussed by a lens onto the sample as in the previous experiments. The amplified signal in the transmitted normal direction is focused onto a non-linear BBO-crystal together with a $150\,fs$ gating pulse. The non-linear crystal emits light in the "upconverted" direction ($\mathbf{k}_{up} = \mathbf{k}_{signal} + \mathbf{k}_{gate}, \omega_{up} = \omega_{signal} + \omega_{gate}$) between the two incoming beams. The time-integrated intensity of the cross-correlation beam reads,

$$I_{crosscorrelation} \propto \int_t I_{signal}(t')I_{gate}(t')\mathrm{d}t'. \tag{4.6}$$

The gate pulse follows a gaussian shape with a $150\,fs$ width which is short as compared to the signal dynamics. Thus, the crosscorrelation beam measures the intensity of the signal at time $t$ when the gating pulse excites the sample. Scanning the optical delay of the gating pulse allows to reconstruct the real-time shape of the signal. The cross correlation signal is selected by a diaphragm and detedcted by a Hamamatsu alkali photomultiplier tube with very low dark current. With the gating pulse duration being $150\,fs$, the time-resolution of the setup is $250\,fs$.

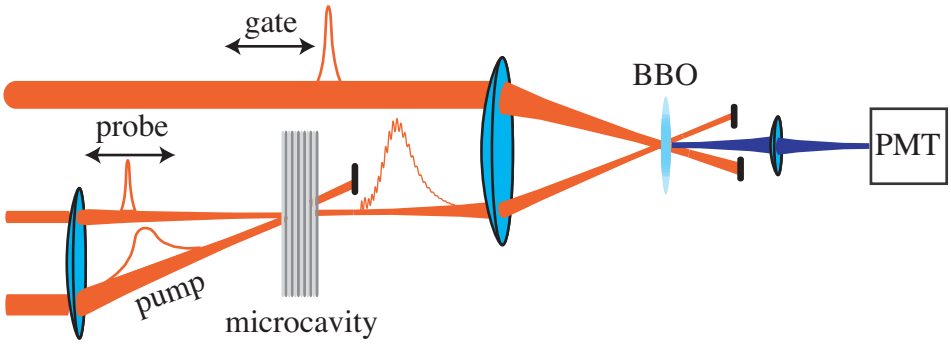


**Figure 4.9:** Upconversion setup.

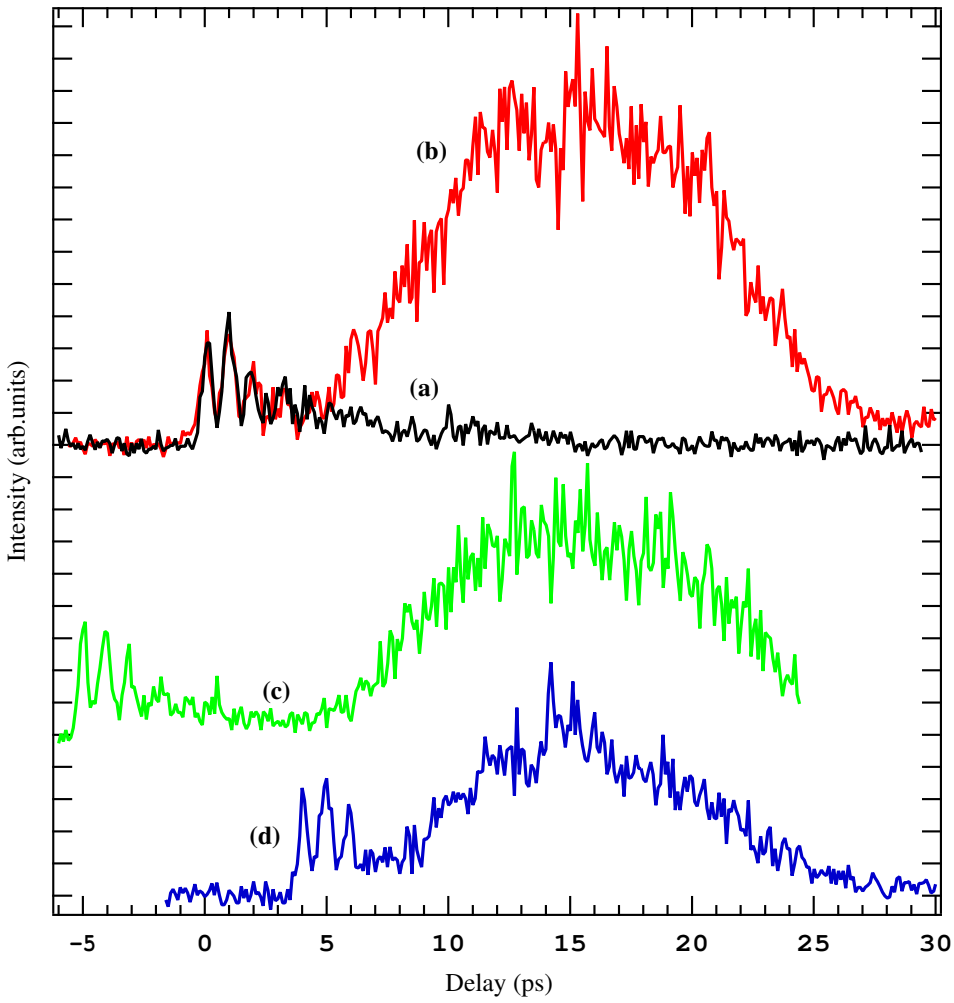


**Figure 4.10:** Temporal evolution of the signal at $k = 0$ as measured with the upconversion detection. The pump excites at zero delay. The probe arrival is varied from $t = 0$ ($b$) to $t = -4\,ps$ ($c$) to $t = +4\,ps$ ($d$). The black curve (a) displays the evolution of the probe alone. The pump polariton density is $3 \cdot 10^{11}/cm^2$, and the probe polariton density is $2 \cdot 10^8/cm^2$. All the measurements in this chapter are carried out with the probe exciting at normal incidence and the pump hitting the sample at the magic angle of $\sim 9.5°$ (with exception of fig. 4.13).

### 4.3.1 Different probe-pump delays

In a first experiment, the time-resolved upconversion experiment has been performed for different pump probe delays.

Figure 4.10 shows the real time evolution of the parametric scattering with the probe at different delays. Curve $a$ shows the evolution of the probe in absence of the pump. The curve decays with the cavity lifetime of $\simeq 10ps$. The intensity oscillations are due to the fact that we excite both the lower and the upper polariton at $k = 0$ [15, 108]. When the pump hits the sample together with the probe at $t = 0$, the intensity decays at first and then starts to grow from $\simeq 4\,ps$ (curve $b$) and reaches maximum intensity at a delay of $15\,ps$. This is the behaviour we expected from the model. However, the delay is longer than in the simulation, where it amounts to $1 - 2\,ps$.

To further investigate this, additional measurements for different probe arrival times were performed (curves $c$ and $d$). When the probe hits the cavity at about $-4\,ps$ (curve $c$), the intensity diminishes as observed for the probe alone. At a similar delay as for curve $b$ the signal starts to rise. The intensity of the signal is smaller, since the amount of polaritons contributing to the signal at $t = 0$ when the pump arrives is smaller than for $b$. Curve $d$ shows the intensity of the transmitted probe when it hits $4\,ps$ after the pump. We observe here, that even when the probe hits after the pump, the signal has a $3\,ps$ rise time. The amount of scattered polaritons is considerably smaller than for curve $b$ because at the moment when the scattering is started here, already a large quantity of polaritons have already left the pump reservoir, thus there are no more available for the scattering.

In the following, we want to investigate the influence of the excitation parameters such as pump and probe intensity, pump angle, and probe pulse shape on the observed build up and the whole signal dynamics.

### 4.3.2 Behaviour for different pump and probe intensities

Figure 4.11 shows the behaviour of the timeresolved signal emission when the pump intensity is varied. Curve $a$ is the probe alone. Curve $b$, $c$, $d$, and $e$ show the pump probe experiment for a pump intensity of 1, 1.3, 1.6, and $2I_{th}$ respectively. In all cases we observe, that it takes some time for the signal to start to rise as shown in the inset. For the lowest pump intensity this takes about $7\,ps$, and for the highest approximately $5\,ps$. For curve $e$ the intensity rises very quickly and exhibits a sharp peak at $t \simeq 10\,ps$. The intensity then decays and rises again to form a second peak at $t \simeq 20\,ps$. The other curves, $b$ to $d$, show a similar double peak structure. The sharpness of the first peak diminishes with decreasing pump intensity. The double peak structure could not be reproduced by the model employed before. The symmetry of the equations suggests oscillations between the pump and the signal-idler state [108], a behaviour well known in classical OPOs [5]. Such oscillations should be triggered by the second term in eq. 2.21 - 2.23, and the oscillation frequency should thus be different for changing pump intensity. As it can be seen on the graph, the oscillation period does not change with pump intensity. Therefore, the oscillations are not due to initial-final state oscillations. A simpler explanation of the double peak could be a temporal replica in an optical device, i.e. an artefact. In this case the shape of the signal and its replica should be the same which is clearly not the case. The second curve in the inset shows the time-integrated signal intensity. It obeys an approximate exponential behaviour as observed both in the experiment (fig. 4.5) and the simulation (fig. 4.8).

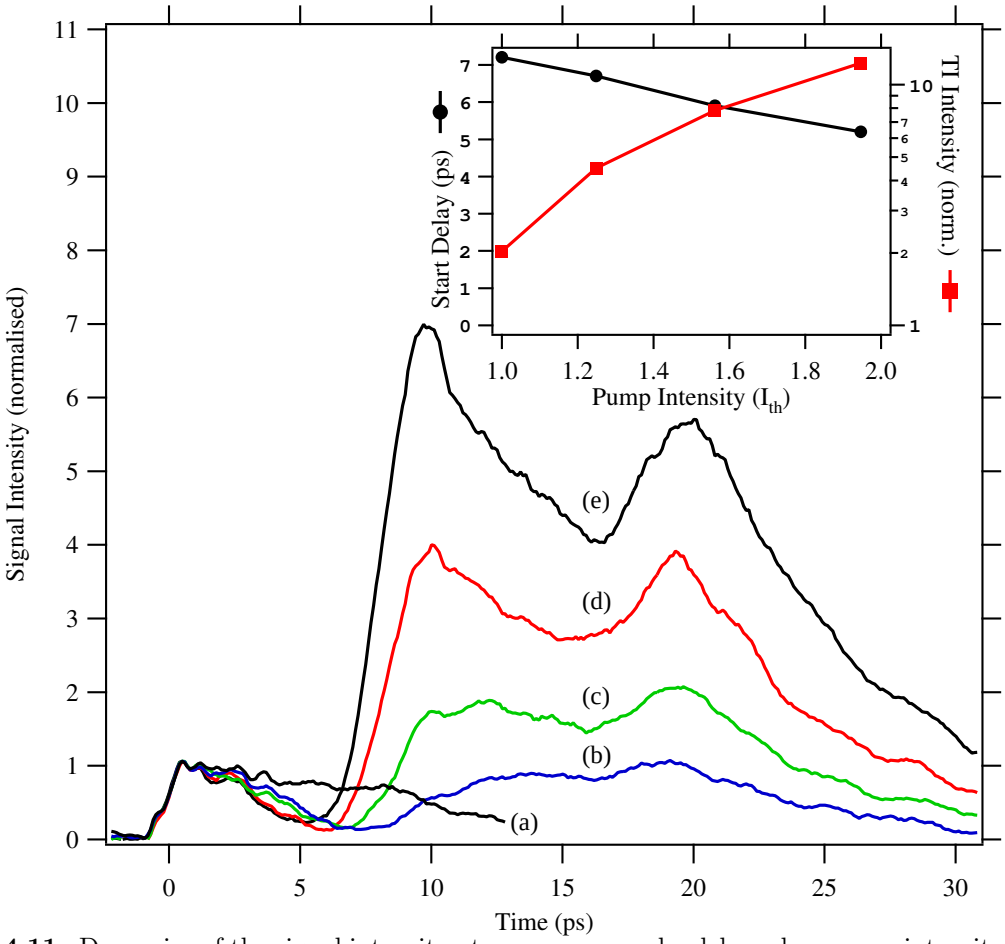


**Figure 4.11:** Dynamics of the signal intensity at zero pump-probe delay when pump intensity is changed. The time averaged pump intensity is normalised to the threshold intensity, where the probe signal is amplified by a factor of two (time-integrated). The probe (curve a) has a time averaged intensity of $0.5\,W/cm^2$. The signal intensity scale is normalised to the intensity of the probe polaritons at $t = 0$. The probe duration is $\simeq 100\,fs$, which results in a spectral width of $6.6\,meV$, whereas the lower polariton linewidth is of the order of $0.1\,meV$. The effective absorbed intensity is thus of the order of $7.5\,mW/cm^2$. Since the probe also excites the upper polariton the curves feature beating oscillations at early times (similar to fig. 4.10). In order to clearly observe when the signal starts to rise, the curves have been smoothed over a time interval of $1.2\,ps$ ($I_{smoothed} = \overline{I}(t \pm 1.2\,ps)$), which is slightly longer than the period of the beating oscillation. The inset shows the delay when the signal starts to rise as well as the time-integrated signal intensity normalised to the time-integrated probe intensity. The pump polariton density at threshold is about $1.5 \cdot 10^{11}/cm^2$, and the probe polariton density is $1.5 \cdot 10^8/cm^2$.

In figure 4.12 we evaluate the effect of a varying probe intensity on the parametric scattering emission. The pump intensity corresponds to $\sim 2I_{th}$, the highest value shown

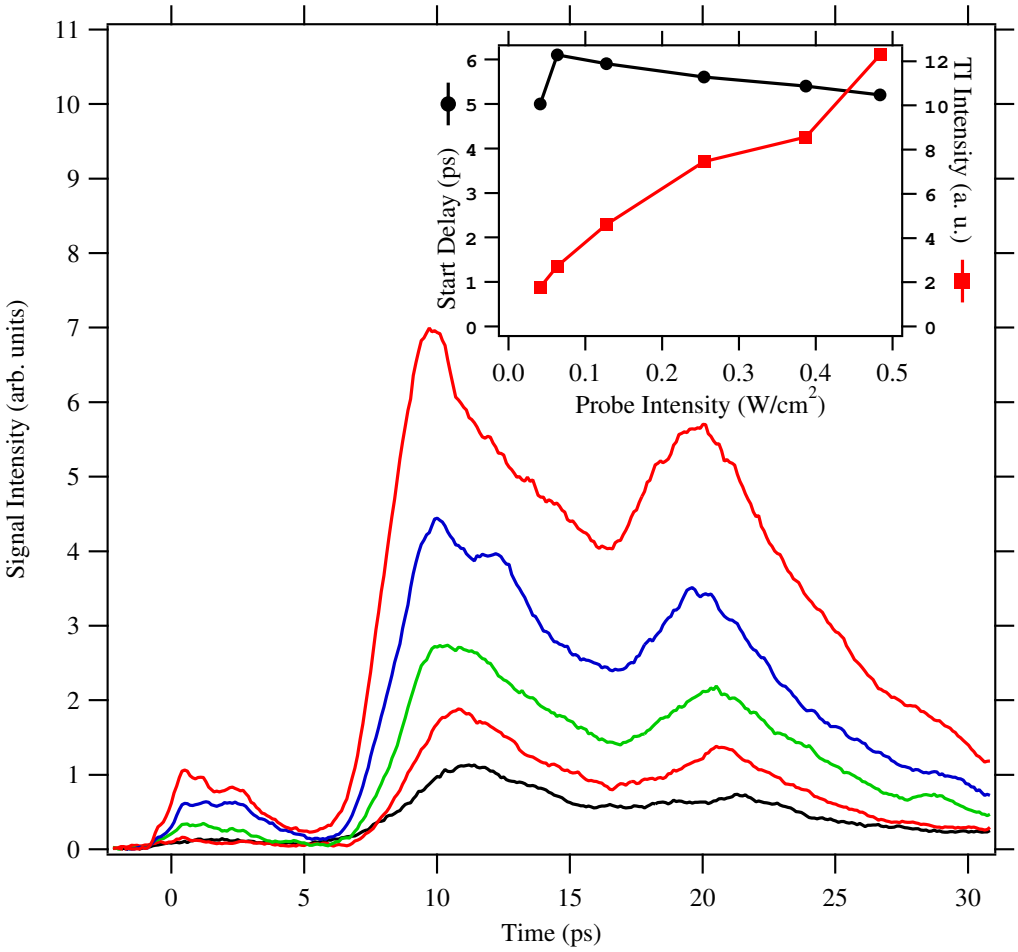


**Figure 4.12:** Signal dynamics as probe intensity is varied, at $I_{pump} = 2I_{th}$. The intensity scale is the same as in fig. 4.11. The inset shows the delay when the signal starts to rise as well as the time-integrated signal intensity normalised to the time-integrated probe intensity. The pump polariton density is about $3 \cdot 10^{11}/cm^2$, and the probe polariton density for the strongest probe ($0.5W/cm^2$) $1.5 \cdot 10^8/cm^2$ and the weakest probe ($0.04W/cm^2$) $1.5 \cdot 10^7/cm^2$.

in fig. 4.11. One observes, that the double peak structure is conserved over the whole range of employed probe intensities and it does not flatten at lower probe intensities (as was observed for low pump intensities). The time-integrated intensity is linear with the probe intensity, which is also found in the model [29]. The delay to when the signal starts to rise remains between 5 and 6 $ps$ and thus stays almost constant. It was observed that the temporal shape of the emission is governed by the pump intensity. This results from the fact that the parameters which act on the scattering system is governed by non-linear effects generated by the pump.

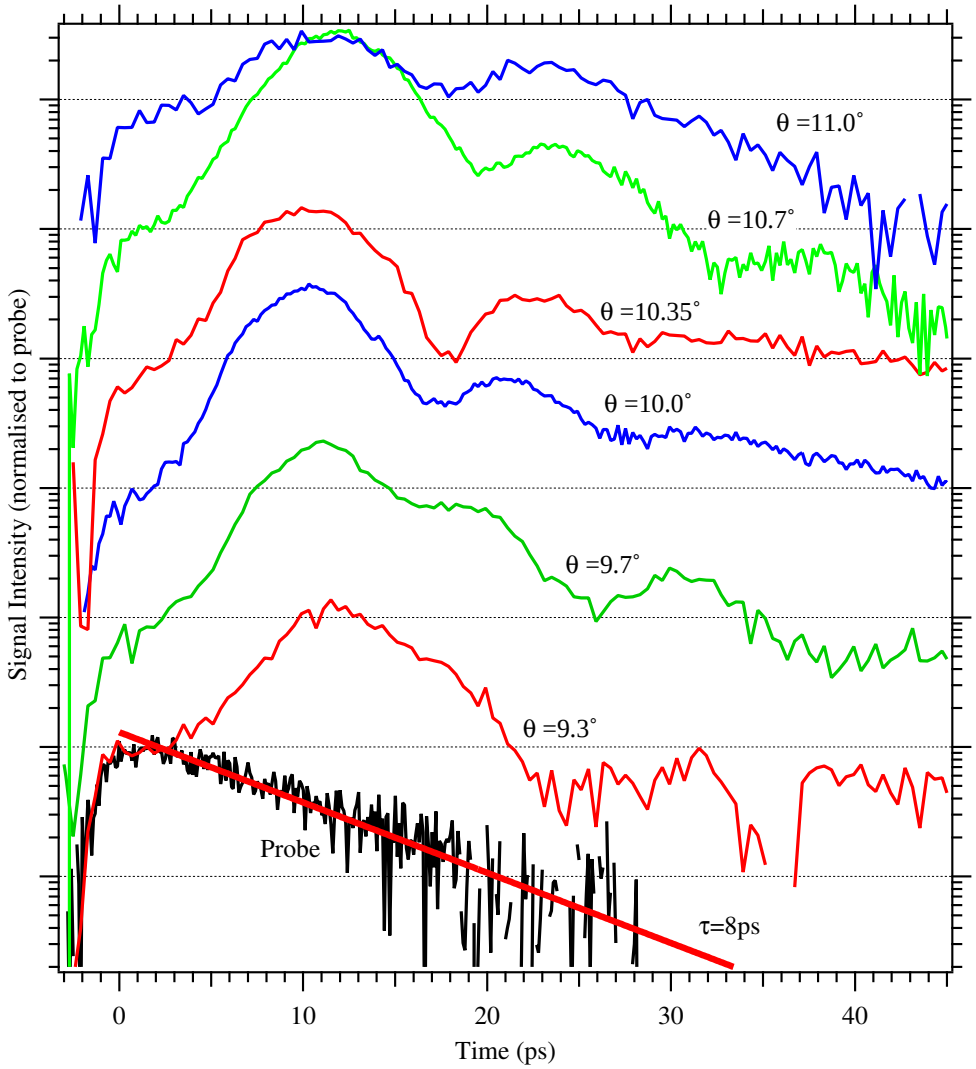


**Figure 4.13:** Signal intensity with time depicted on a logarithmic scale for different pump incidence angles around the magic angle. The signal intensity is normalised to the signal intensity of the probe at zero delay. The curves are multiplied by factors of 1, 10, 100, ... to separate them. The probe features a mono-exponential decay representing a lower polariton lifetime of $8\,ps$. Since we use here a bandpass filter for the probe, the lower polariton only is excited at $k = 0$ and hence no beating between upper and lower polariton is observed. For all the pump incidence angles, the pump pulse centre wavelength has been adjusted to fit the lower polariton dispersion at the respective angle. The pump polariton density for all pump angles amounts to $10^{12}/cm^2$, and the probe polariton density to $6 \cdot 10^8/cm^2$.

### 4.3.3 Variation of the pump incidence angle

Upconversion measurements were performed for a varying pump angle (figure 4.13). To avoid the beating oscillations between lower and upper polariton, the probe pulses were filtered with a band pass filter, so that only the lower polariton resonance is excited.

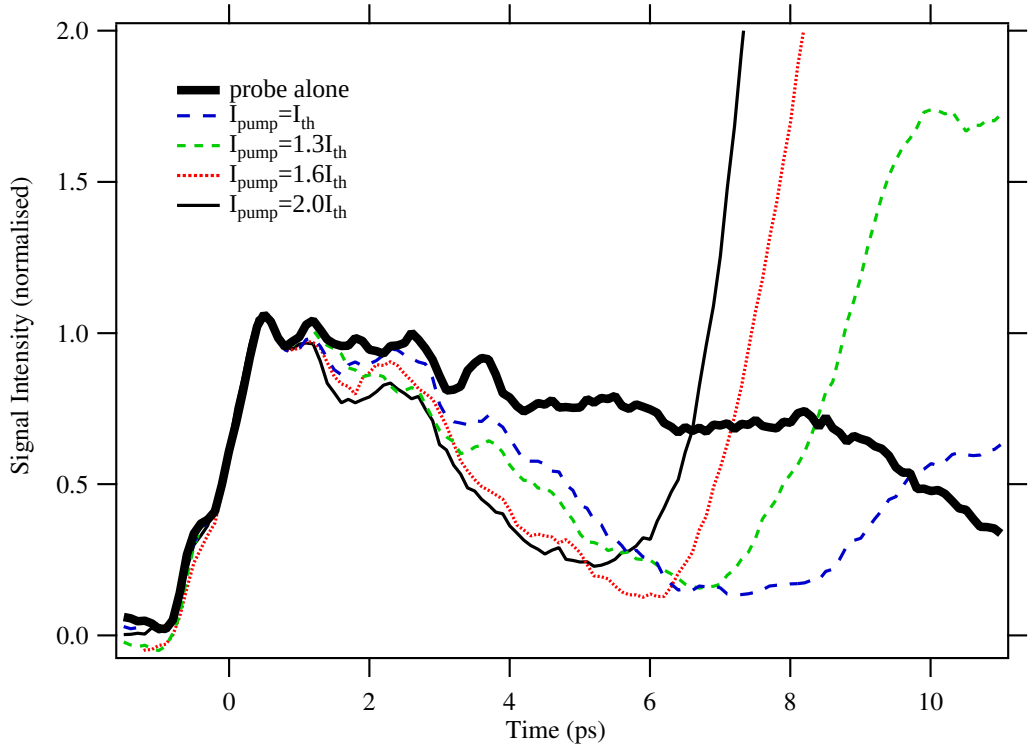


**Figure 4.14:** Zoom of the early time dynamics of the signal of fig. 4.11. The probe is the bold black curve. All the amplified signal curves transiently pass below the intensity of the probe alone.

Consequently, the probe polariton intensity (black curve) decays without beating oscillations. From the exponential fit we extract the lower polariton lifetime at $k = 0$ of $\tau = 8\,ps$. The upper six curves show the time evolution of the signal intensity in a pump-probe experiment, when the pump angle is varied between 9.3° and 11°. The maximum of the amplified signal emission takes place between 10 and 12 $ps$. The decay of the signal intensity shows oscillations, which are particularly clear at the central pump angles around the magic angle. The time period of the oscillations is almost constant for the different angles. The fact that the oscillation period is static with the pump angle could be interpreted in terms of a defect in the sample.

### 4.3.4 Transient deamplification

Figure 4.14 shows a zoom of the early time evolution of the signal in figure 4.11. The probe curve is depicted by the bold black curve. If the pump is switched on and adjusted to the threshold intensity, we observe that the intensity of the amplified signal clearly passes below the probe intensity. When the pump intensity is increased to 1.3, 1.6, and $2I_{th}$, the effect becomes weaker and the signal intensity starts to rise earlier. The signal amplification factor transiently goes below unity, a phenomenon known as de-amplification. This is a well known feature for OPOs using transparent non-linear

crystals. De-amplification is observed for a triply resonant OPO, when the cavity is detuned for the idler [63]. In this case the light put into the signal is transferred to the pump mode. The model [29] is very close to the standard model of a "classical" OPO (see section 2.5.3). It has however not been possible to reproduce any de-amplification phenomenon in the simulation using a single probe, even by pushing the model to the limits of its validity (using pump angles $\neq$ the magic angle, increasing the pump intensity to very high values). The behaviour could also be attributed to the influence of higher order scattering processes as presented in [101]. Higher order processes become more important at higher pump intensities. Here we observe, that the transient de-amplification diminishes with rising pump intensity. The de-amplification is thus not due to the stated higher order processes. The ultimate reason for the transient de-amplification could be the very complex renormalisation dynamics of the dispersion governed by the pump polarisation but also the signal and idler polarization [30].

### 4.3.5 Shaping the probe pulses

The parametric amplification experiments presented have partly been done using the large band laser spectrum for the probe, and a spectrally filtered probe exciting only the lower polariton at $k = 0$ (section 4.3.3). An argument for the large band probe is the higher time-resolution of the experiment and the fact to have one optical instrument less which could harm the results with its imperfections (temporal replicas, ...). Moreover, the large band probe excites both lower and upper polariton resonance, which causes a beating of the temporal curves. Monitoring the beating one can make sure that the experiments are made in the strong coupling regime. On the other hand, the beating between the lower and the upper polariton makes it more difficult to analyse the early time phenomena (section 4.3.2). Furthermore it cannot be completely excluded, that the upper polaritons excited by the probe influence the parametric scattering. To check this last point, we performed the parametric amplification experiment using both large and narrow band probes, maintaining all other experimental conditions exactly identical. To generate the shaped probe, we did not use the picosecond Fabry-Perot filter, because the filter changes the pump probe delay, spatially slightly changes the alignment of the beams, and introduces its imperfections. The experiment is done using the stabilised interferometer (see fig. 3.1) employed in the coherent control experiments presented in chapter 3.

Fig. 4.15 shows an explanation of how the pulse shaped probe pulses are generated. The aim is to have on the one hand a large band probe and on the other hand a narrow band probe only exciting the lower polariton. The right panel shows the Gaussian spectrum of the laser (black), which covers both lower and upper polariton resonance (green). The large band pulse is obtained by only using one arm of the interferometer and blocking the other. To generate the narrow probe, we have to use the interferometer. From the convolution theorem in Fourier analysis it is known, that the spectrum of a pulse can be sinusoidally modulated using two pulses temporally seperated by the inverse of the spectral modulation frequency. This case is shown by the red curve: the lower polariton is excited, without exciting the upper polariton. The position of the spectral fringes can be set by adjusting the relative phase of the two pulses, i.e. tuning

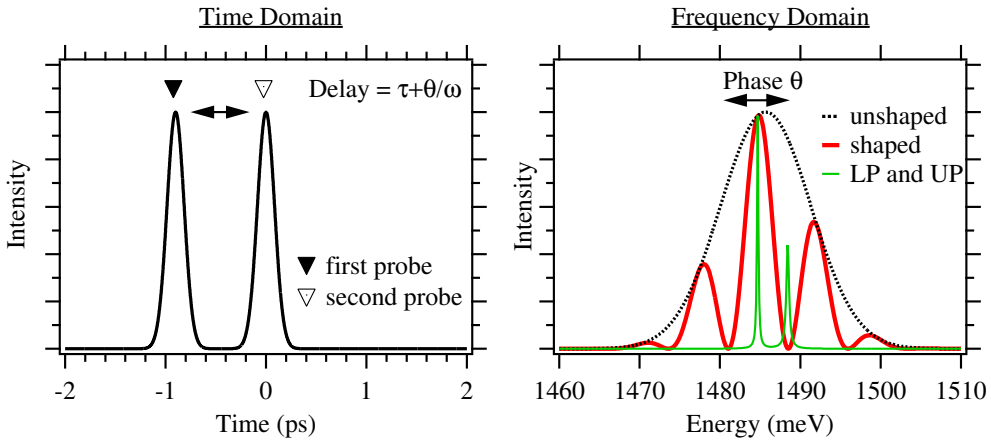


**Figure 4.15:** Temporal and spectral characteristics for pulse-shaped probe pulse and the unshaped broad band probe pulse.

their optical path difference corresponding to fractions of the optical wavelength. The left panel shows the two probe pulses in the time domain. The temporal separation in fact corresponds to the beating period of the polaritons. The intensity entering the interferometer was adjusted to obtain the same time integrated lower polariton signal transmission intensity looking at the spectrometer.

Fig. 4.16 shows the signal dynamics measured with the broad band probe (black curve) and the pulse shaped probe, which excites only the lower polariton (red curve). The inset shows a zoom into the early time dynamics of the signal emission on a linear scale. In the large band case (black), the dynamics show a LP/UP beating as also observed in fig. 4.10. The red curve displays the behaviour for the narrowband probe. The first $100\,fs$-pulse (filled triangle) impinges about $1\,ps$ before the second (empty triangle) and the pump. The first pulse excites both the upper and the lower polariton. The second one has the appropriate phase and delay to only enhance the intensity at the lower polariton and to put out the upper polaritons by destructive interference.

The main panel of fig. 4.16 shows the signal emission for the two cases on a logarithmic scale. The signal intensity is normalised to the probe intensity at $t = 0$. Similarily to the previous experiments, the curves first decay and then grow to a maximum at $t \simeq 10\,ps$. Since the pulse-shaped probe only excites the lower polariton resonance, no beating oscillations are observed for the red curve. From the maximum, the curves both show an exponential decay governed by the lower polariton lifetime. The two curves perfectly overlap from $t \simeq 5\,ps$ for the entire time interval investigated which corresponds to over one order of magnitude in intensity. This demonstrates that the upper polariton has no influence at all on the parametric scattering. It clearly justifies that it is a good approximation to neglect the contribution of the upper polariton in the model [29], which is written in the lower polariton basis.

The perfect mono-exponential decay has not been observed in all the preceding

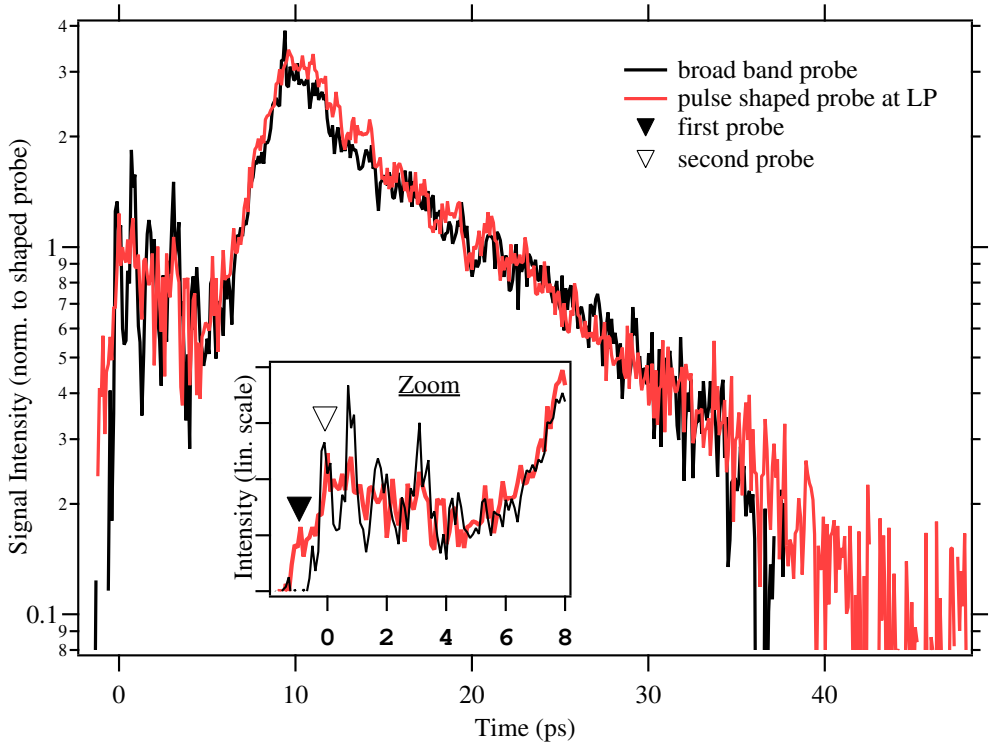


**Figure 4.16:** Temporal evolution for signal intensity with a broad-band (black) and a pulse-shaped probe pulse (red). The signal intensity scale has been normalised to the transmitted signal intensity of the shaped probe pulse around $t = 0$. The pump density amounts to $7 \cdot 10^{11}/cm^2$ and the probe density to $1 \cdot 10^8/cm^2$. The inset shows a zoom into the early time dynamics on a linear scale.

experiments. In section 4.3.2 and 4.3.3 double peak structures and even oscillations have been observed. These may be due to some structural imperfection of the sample (the point investigated on the sample was not always the same), excitation conditions also changed slightly.

## 4.4 Scattering dynamics in the spontaneous regime

In the previous sections, the dynamics of the polariton parametric scattering has been discussed in the stimulated regime, when an external probe is applied. In section 4.1, the kinetics of the pump polaritons was analysed when only the pump beam is applied to the sample (fig. 4.2, panel (a)). In the following, we want to analyse the non-linear properties of the spontaneous parametric scattering and pay special attention to the kinetic properties of the system in vicinity of the threshold where the stimulation begins in the spontaneous regime. The spontaneous parametric scattering will be investigated both under cw and pulsed excitation to explore the steady-state properties of the process on the one hand, and to allow for the comparison with the pulsed experiments

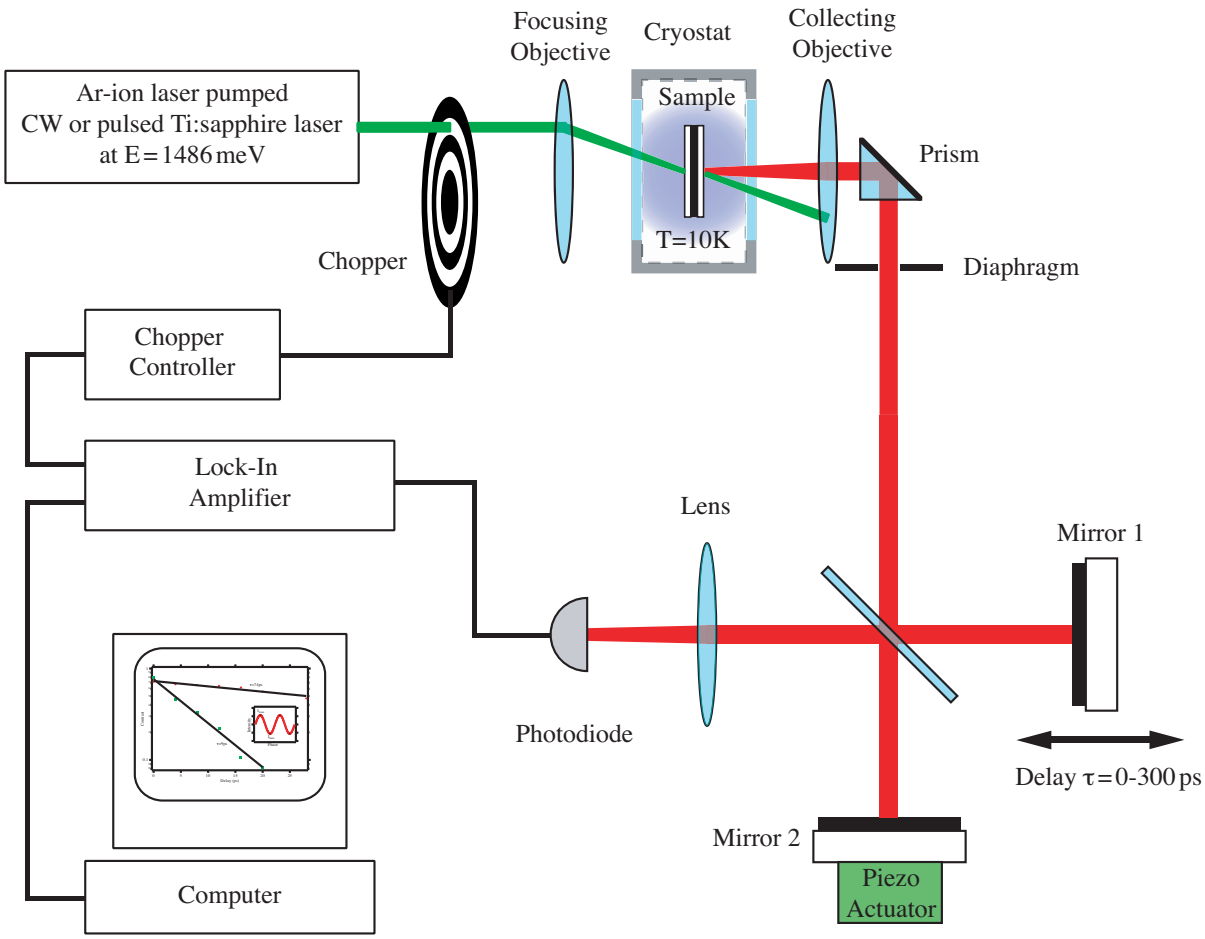


**Figure 4.17:** Setup for the autocorrelation measurements

earlier in this chapter on the other hand.

### 4.4.1 Autocorrelation setup

The goal of the presented measurements is to enable a comparison of the measurements made in both the cw and the pulsed regime. In cw, the use of a streak camera setup as in section 4.1 is not possible. We thus employed an auto-correlation setup to obtain precise information about the dynamics of the spontaneous parametric scattering. The auto-correlation setup is depicted in fig. 4.17. The sample is excited by laser light impinging at the magic pump angle which has been focussed by a photography objective. As a laser source, a cw or a pulsed Ti:sapphire laser is used with a wavelength centred at $\sim 1486meV$ which corresponds to the pump polariton energy. The laser beam is modulated by a mechanical chopper to allow a synchronous detection using a photodiode and a lock-in amplifier. The emission of the sample around normal incidence is collected by a second photography objective. The diaphragm selects the emission from the sample at $\theta = 0 \pm 2.5°$, which covers the signal polariton emission. The signal beam is sent

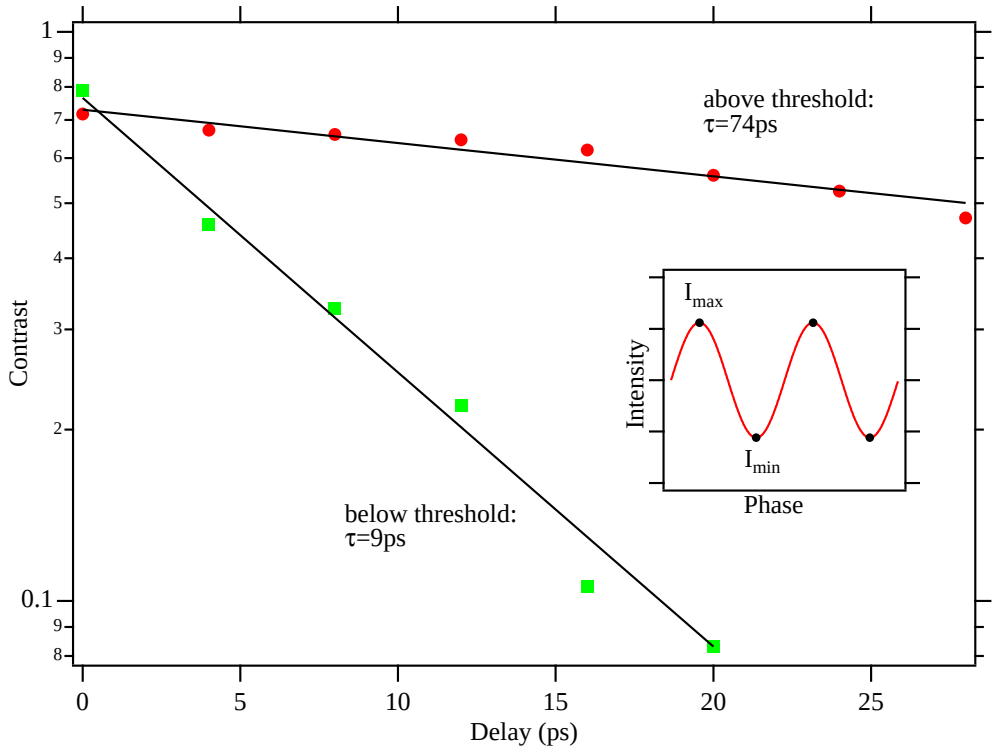


**Figure 4.18:** Contrast of the intensity oscillations versus delay between the interferometer paths below and above threshold. The inset shows an intensity oscillation.

into a Michelson interferometer, passes a lens and is detected by a photodiode. An active stabilisation of the interferometer (see appendix A) stabilises the relative path difference of the two interferometer arms within a precision of $10\,nm$. Using the active stabilisation, the relative path difference can be scanned and the resulting intensity variations (the interference fringes) can be detected on the photodiode (see fig. 4.18, inset). The relative delay of the two interferometer arms can be varied from $0-300\,ps$, this corresponds to moving mirror 1 about $3\,cm$. The signal intensity can be detected by simply blocking one of the interferometer arms. The diode is part of a synchronous detection and allows the detection of very weak signals, which is especially important for measurements below the non-linear threshold.

The setup represents a Fourier transform spectrometer. When the relative position $x$ of the two mirrors is scanned, an interferogram $I(x)$ can be recorded, which corresponds to the Fourier transform of the investigated signal $I(k)$ [16]. In our case, we are able to greatly simplify the detection, since the spectrum we want to detect consists of a single line of approximate Lorentzian shape. The Fourier transform of a Lorentzian is an exponential. The constant characterising the exponential is the (intensity) coherence time of the signal polaritons which is proportional to the inverse of the spectral linewidth. The principle of the measurements is explained in fig. 4.18. When the relative path difference of the two interferometer arms is scanned on a scale corresponding to the signal wavelength, interference fringes are recorded (see the inset).

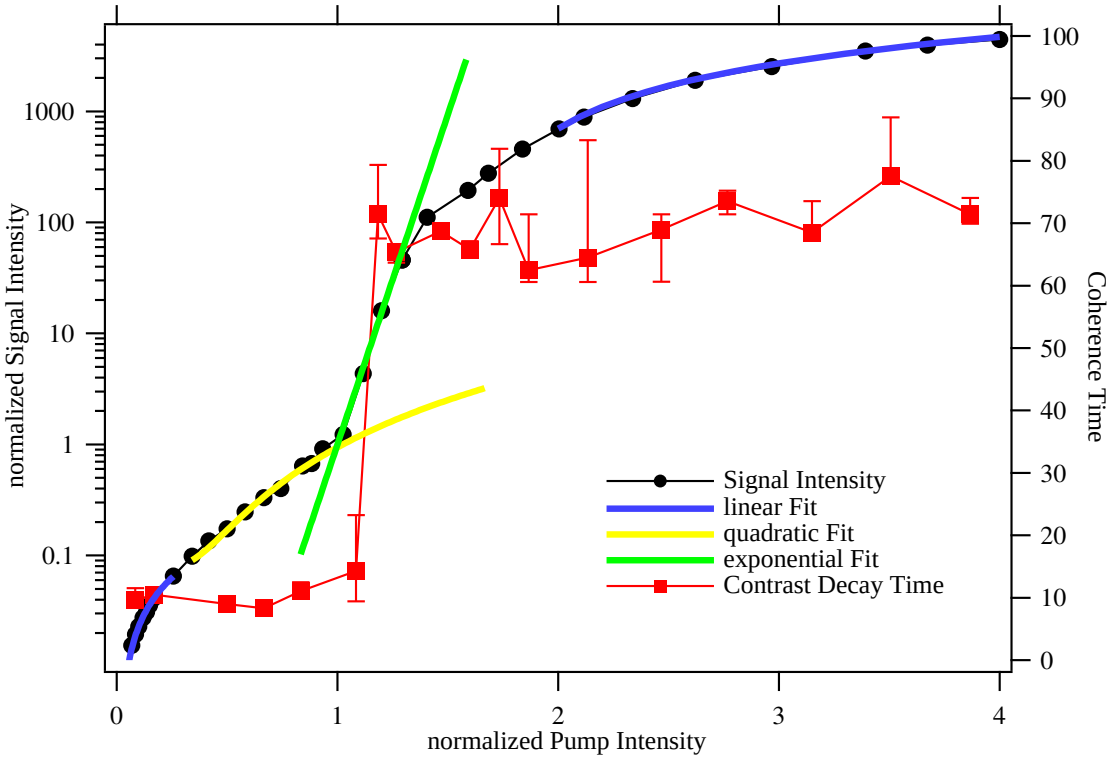


**Figure 4.19:** Signal intensity and decay time of the Contrast versus the pump intensity. The cavity is excited by a cw laser. The red, green, and blue curves show a linear, a quadratic, and an exponential dependence of the signal intensity on pump intensity. The contrast decay time gets about eight times longer at the exponential threshold, which occurs for a threshold polariton density of $\sim 4 \cdot 10^{10} polaritons/cm^2$.The pump and signal intensity scales are normalised to the pump and signal intensity at threshold.

The minimum and the maximum of the fringes are used to calculate the fringe contrast, which is defined as $C = (I_{max} - I_{min})/(I_{max} + I_{min})$. The contrast can be measured for different relative delays of the interferometer arms. This is represented on a logarithmic scale versus the delay of the interferometer arms. The measured points are then fitted by an exponential ($I = I_0 \cdot exp(-t/\tau)$) with a time constant $\tau$ corresponding to the coherence time of the signal. In fig. 4.18, decay curves for two different pump intensities below and above threshold are depicted with contrast decay times of 9 and 74 $ps$. In the following experiments, this contrast decay time is recorded together with the signal emission intensity versus the incident pump intensity.

### 4.4.2 Coherence build-up under CW excitation

Figure 4.19 displays the evolution of the signal output intensity together with the coherence time versus the pump intensity under cw excitation. For weak excitation intensities, the dependence of the signal intensity on the pump intensity is linear. In section 4.1 we observed that a considerable amount of polaritons relaxed down to the

bottom of the lower polariton dispersion by the emission of phonons. The relaxation by the emission of phonons is independent of the pump intensity. The linear dependence can thus be attributed to this process. The contrast decay time of $\tau = 10\,ps$ (red curve) corresponds in this regime to the lifetime of the polaritons at $k = 0$. At about 1/3 of the threshold intensity, the dependence becomes quadratic, indicating the onset of a polariton-polariton interaction, i.e. when the wavefunctions of the polaritons start to overlap. In this regime, which corresponds to the regime explored in fig. 4.2, polaritons scatter spontaneously from the pump into a signal-idler pair. The polariton lifetime slightly decreases to $\tau = 8\,ps$. From 1 to $1.3 I_{th}$, the signal intensity rises exponentially by a factor of about 100, indicating the onset of the self stimulation of the polariton parametric scattering. Near threshold, the contrast decay times increase sharply by a factor of 7 to $\sim 70\,ps$. The contrast decay times stay almost constant to $I_p = 2 - 4_{th}$, the pump intensity again increases linearly.

### 4.4.3 Simple model for the spontaneous parametric scattering

The spontaneous parametric scattering has been modelled in different theoretical works treating the Heisenberg equations of motion for the Hamiltonian described in section 2.5.3. In this section we model the system using a very simple phenomenological approach in order to understand some dominant features observed in the measurements shown in fig. 4.19. The polariton populations at signal ($N_0$), pump ($N_{k_p}$), and idler ($N_{2k_p}$) are modelled, having a radiative linewidth of $\gamma_0, \gamma_{k_p}$, and $\gamma_{2k_p}$. Pump polaritons are created with a rate $\alpha$ by a cw laser. The pump polaritons can relax down the dispersion via the emisson of phonons described by the constant $\epsilon$. This relaxation rate scales linearly with pump intensity and the polaritons go from the pump (negative term) to the signal (positive linear term). The second channel for the polaritons to go from the pump to the signal is the polariton-polariton scattering, which scales with the square of the pump intensity. It is caracterised by the polariton scattering constant $\beta$. The factor of $\frac{1}{2}$ for the polariton-polariton scattering process represents the fact that half of the polaritons leaving the pump mode go to the signal and the idler respectively.

$$\frac{\partial N_0}{\partial t} = -\gamma_0 N_0 + \epsilon N_{k_p} + \frac{\beta}{2} N_{k_p}^2 \tag{4.7}$$

$$\frac{\partial N_{k_p}}{\partial t} = -\gamma_{k_p} N_{k_p} - \epsilon N_{k_p} - \beta N_{k_p}^2 + \alpha \tag{4.8}$$

$$\frac{\partial N_{2k_p}}{\partial t} = -\gamma_{2k_p} N_{2k_p} + \frac{\beta}{2} N_{k_p}^2 \tag{4.9}$$

In the steady state regime corresponding to the cw-measurement, the variation of the respective populations is zero and the equations can be solved analytically giving

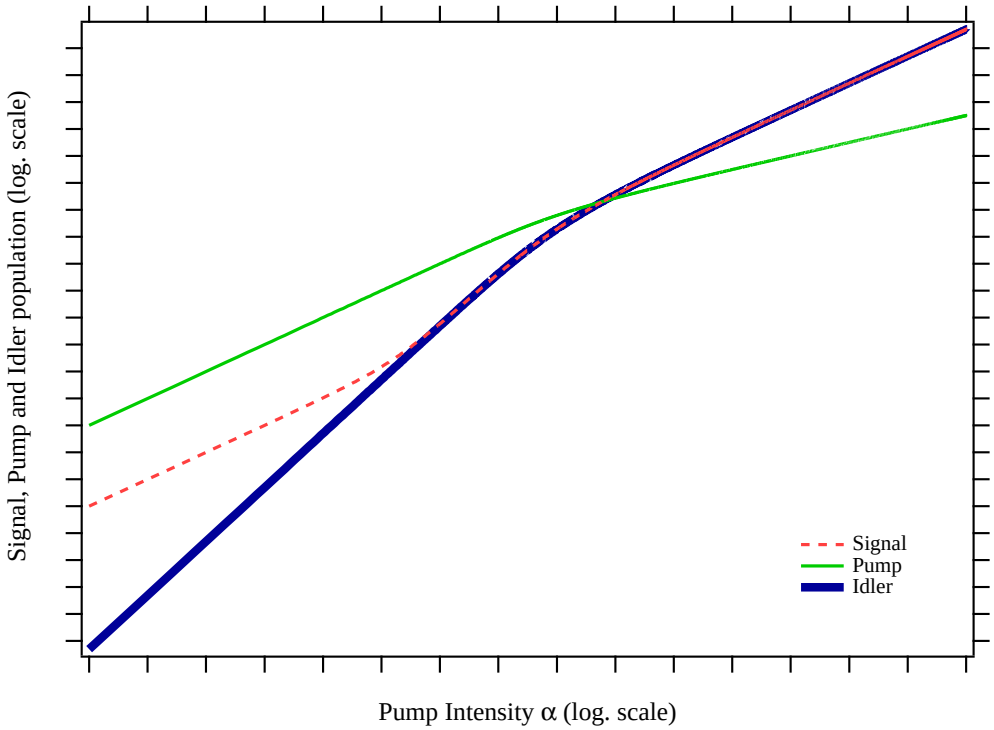


**Figure 4.20:** Plot of the analytical solutions of equations 4.10-4.12 for the signal, pump, and idler populations as a function of the pump intensity $\alpha$.

$$N_0 = +\frac{\beta}{2\gamma_0} N_{k_p}^2 + \frac{\epsilon}{\gamma_0} N_{k_p} \tag{4.10}$$

$$N_{k_p} = -\frac{\gamma_{k_p} + \epsilon}{2\beta} + \sqrt{(\frac{\gamma_{k_p} + \epsilon}{2\beta})^2 + \frac{\alpha}{\beta}} \tag{4.11}$$

$$N_{2k_p} = +\frac{\beta}{2\gamma_{2k_p}} N_{k_p}^2. \tag{4.12}$$

The signal, pump, and idler intensities are plotted in figure 4.20 versus the intensity of the incident laser field $\alpha$. The plot is represented on a log-log-scale over several orders of magnitude. As expected the intensity of the signal scales linearly with the incident laser power for low incident laser intensities. In an intermediate regime, the quadratic dependence on the pump density starts to govern and the signal intensity grows quadratically. At $I_{sat}$, the signal grows again linearly with the laser intensity, since the pump starts to be depleted. The behaviour of the idler is similar to that of the signal with the exception, that the linear dependency at low laser intensity is not observed since the phonon relaxation channel does not exist for the idler. The pump polariton density shows a linear behaviour with laser intensity and grows at high laser intensity with the square root, since it starts to be depleted by the parametric

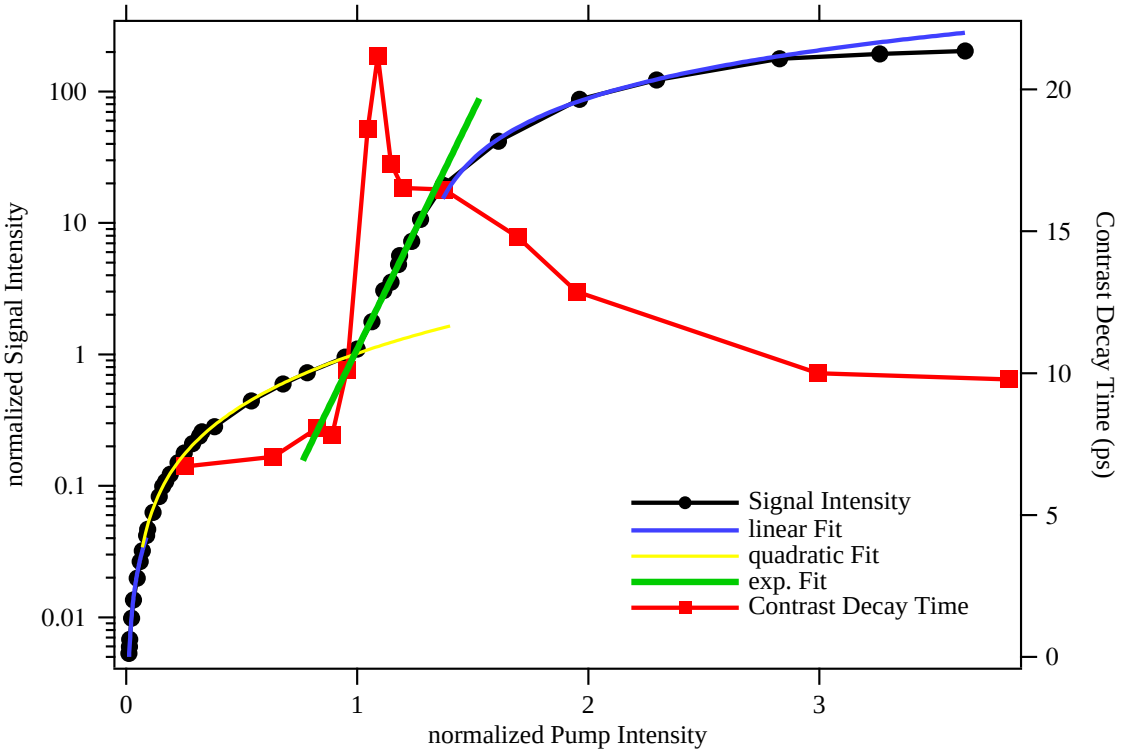


**Figure 4.21:** Signal intensity and decay time of the contrast versus the pump intensity. The cavity is excited by laser pulses with a $1\,ps$ duration. The red, green, and blue parts of the curve show a linear, a quadratic, and an exponential dependence of the signal intensity on pump intensity. The contrast decay time gets about eight times longer at the exponential threshold. The pump intensity has been normalised to the exponential threshold pump density of $\sim 10^{13}/(pulse \cdot cm^2)$. The logarithmic signal intensity scale has been normalised to the signal intensity at threshold. The red triangle point corresponds roughly to the experimental conditions of the streak camera measurement shown in panel (a) of fig. 4.2.

scattering. The model presented is clearly only a phenomenological approach which neglects any stimulation effects and the build-up of a coherent signal polarisation. A modelling including stimulation and the transition to a coherent signal polarisation has been developed for example in reference [98] and reference [25]. In reference [98] a set of 12 coupled differential equations have been solved. In [25] the system was modelled by quantum Monte Carlo simulations. Both approaches are quite complex. The exponential threshold of the signal intensity, which is not reproduced in fig. 4.20 is expected to occur in the quadratic regime of the signal emission.

### 4.4.4 Coherence build-up under pulsed excitation

In section 4.1, the polariton emission under resonant excitation was investigated using a streak camera. As the streak camera requires a periodic time-base, the measurements were done in the pulsed regime. To compare these data with the auto-correlation mea-

surements, the experiment has been repeated under pulsed excitation. Qualitatively the behaviour of the signal intensity curve in figure 4.21 is the same as that in the cw experiments shown in figure 4.19). The signal intensity starts to grow linearly due to the phonon interaction followed by a quadratic increase because of the polariton-polariton interaction. The signal emission becomes self-stimulated at $I_p = I_{th}$ and grows exponentially from $1 - 1.3I_{th}$ over one order of magnitude in signal intensity. At high pump intensity, the signal intensity again saturates and becomes linear, which can be attributed to the pump depletion. From $2.8I_{th}$, the signal intensity increases more slowly than the linear fit. This could be attributed to the fact that we are working at very high pump densities ($\sim 10^{13}/(pulse \cdot cm^2)$ at threshold) and we should expect additional loss mechanisms of pump polaritons by for example higher order scattering mechanisms or even the beginning of the break down of the strong coupling regime.

Finally we analyse the behaviour of the coherence decay time. The coherence time starts again at the value of the linear lifetime of the polaritons at $k = 0$ of $7\,ps$[2]. At threshold it triples to $\sim 21\,ps$. With further increasing pump intensity it begins to decrease, and at $I_p = 3.8I_{th}$ it has almost recovered the linear polariton lifetime. The lower maximum value of the contrast decay time and its decrease above threshold is the main difference from the measurements under cw excitation. It is clear, that in the pulsed regime, the characteristic signal emission time cannot be very much longer than the pump lifetime. Under pulsed excitation, the lifetime thus only triples in contrast to the cw measurement, where the contrast decay time is multiplied by a factor of 7 at threshold. The second difference is harder to explain. Above threshold, the dynamics of the polaritons is governed by the coherent polarisation at signal, pump, and idler [98, 102]. This experiment can be compared, with some prudence, to the dynamics measured in the pump-probe experiments, since the process in the stimulated exponential regime can be seen to be stimulated by a probe provided by the relaxed pump polaritons. In fig. 4.11, the time-resolved signal dynamics are presented in the pump probe experiment for a changing pump intensity. If we were to do an auto-correlation measurement in this experiment, it's clear that an auto-correlation of the complex curves would not result in a simple mono-exponential decay. The approximated decay time for the contrast would be larger around $I_p = I_{th}$ than at the highest pump intensity value. Around threshold, the pump mode is almost not depleted, and the parametric scattering from the pump into signal and idler can be maintained for a long time. When the pump intensity increases, the signal intensity grows very quickly and strongly depletes the pump mode at the same time. The depleted pump mode can no longer maintain the parametric scattering, and the signal escapes from the cavity with the polariton lifetime. The decrease of the contrast decay time at high pump intensity can thus be attributed to the depletion of the pump mode in that regime.

In this section, we have analysed the different regimes occuring when a microcavity is excited by a pump beam at the magic angle. At low pump intensities the signal emission intensity around normal incidence scales linearly with pump intensity, this is attributed to the relaxation of polaritons by phonon emission. The linear regime is

[2]The value is slightly different from the one in the cw experiment. This is attributed to the fact that the two experiments in the cw and the pulsed regime are not performed at exactly the same point on the sample: The lasers have been changed between the measurements.

followed by a quadratic regime, when the polaritons start to interact with each other. At the exponential threshold, the decay time of the contrast strongly increases due to the onset of the self-stimulation of polariton scattering. As already shown in section 4.1, the phonon mediated relaxation of pump polaritons plays an important role for the spontaneous scattering dynamics (see fig. 4.2, panel a). This relaxation channel is not included in the models [98, 102] and it should be included in future investigations.

# Chapter 5

# Bose-Einstein-Condensation of Polaritons

## 5.1 Introduction to Bose-Einstein Condensation

Nearly 80 years ago the Indian physicist Satyendra Nath Bose published a paper in the Zeitschrift für Physik [17], where he derived Planck's law of black body radiation from a gas of indistinguishable photons. The translator of the paper, Albert Einstein, recognised the impact of this work and extended Boses theory to a theory for an ideal gas of bosons [43]. In his work he claimed that such an ideal Bose gas could undergo "something similar to what happens to a vapour under isothermal compression above the saturation volume. A separation occurs: one part "condenses", the rest remains a "saturated ideal gas"...."[1] His famous claim, later known as Bose-Einstein Condensation (BEC) triggered an enormous amount of very beautiful and interesting works to show Bose-Einstein Condensation in different physical systems, and an intense research is still going on until today.

In 1938 Kapitsa, Allen, and Misener found that liquid helium ($He^4$) showed some strange behaviour when cooled down below the so-called $\lambda$-point, at a temperature of $2.17\,K$ [61, 1]. The liquid dramatically changed its properties. Especially the viscosity of the liquid vanished, a phenomenon now known as superfluidity. Already in the same year F. London sensed that this phase-transition must be due to a Bose Einstein Condensation phenomenon [73]. The theory formulated by Bose and Einstein for a non-interacting ideal quantum gas was adapted to an interacting fluid by Landau in 1941 [66]. In 1947 Bogoliubov developed a microscopic theory for superfluidity [13]. The concept of off-diagonal long-range order, describing the coherence properties of condensates, was introduced in the fifties by Landau and Lifshitz [67], Penrose [85], and Penrose and Onsager [86].

Since the 70s increasing sophisticated methods have been developed to cool down dilute atomic gases [27, 28]. It took more than twenty years to experimentally observe

[1] The original text in German reads: "Die Behauptung geht also dahin, daß etwas Ähnliches eintritt wie beim isothermen Komprimieren eines Dampfes über das Sättigungsvolumen. Es tritt eine Scheidung ein; ein Teil >>kondensiert<<, der Rest bleibt ein >>gesättigtes ideales Gas<< ($A = 0$ $\lambda = 1$). ..."

BEC in 1995. In very complex setups combining several cooling techniques the groups of Cornell and Wiemann at Boulder [2] and Ketterle at MIT [38] suceeded in producing condensates of $^{87}Rb$ and $^{23}Na$ respectively. Soon after condensates were achieved using other atomic species such as $^{7}Li$ [19], spin polarized hydrogen [48], metastable $^{4}He$ [40, 91], and $^{41}K$ [78].

In parallel to the atom community, semiconductor physicists started to search for the condensation of quasi-particles in solids. The idea of Bose-Einstein condensation of excitons was risen in 1962 by Moskalenko [79] and Blatt [11]. The theoretical work was continued by Keldysh [62] and Zimmermann [119] and the experimental work in the field started with the investigation of bulk excitons in $Cu_2O$ [58, 106, 105, 47, 72], in AgBr [32], and biexcitons in $CuCl$ [52]. With the improving quality of semiconductor nanostructures, quantum wells have been subject to intense research [118, 104, 22, 21] and as well as exotic electron-electron bilayer structures [44]. The problem of a purely excitonic system is that, normally the density needed to achieve quantum-degeneracy is of the order of the Mott transition, where the fermionic character of the exciton constituents appears. This problem could be seen to be overcome with the realisation of microcavity exciton polaritons in 1992 [117]. The polaritons have a much lighter mass than excitons: The density of states per unit energy is orders of magnitude smaller than the exciton's and this facilitates the observation of collective boson phenomena. In 1996, Imamoglu proposed the existence of a non-equilibrium bose condensate, and a polariton laser [60]. The most common microccavity samples at that time where realised in the GaAs material system. The existence of a polariton laser or a polariton condensate was claimed in reference [83], however it turned out that the observed non-linear threshold behaviour was due to the onset of lasing from electron hole pairs as occurs in vertical cavity surface emitting lasers [24]. In 2002 Deng *et al.* claimed the observation of Bose-Einstein condensation of polaritons occuring in a GaAs based microcavity showing a large polaritons splitting due to the presence of 12 strongly coupled quantum wells [39]. The claim was supported by a Hanbury-Brown-Twiss measurement suggesting the transition of the system from a thermal to a coherent state. This transition should be observable as a quick change of the second order temporal coherence function $g^{(2)}$ from 2 to 1 at the transition threshold for Bose-Einstein condensation. The value in reference [39] changed very slowly from $\sim 1.8$ at threshold to $\sim 1.6$ at $\sim 15 I_{th}$, where a break-down of the strong coupling is likely to have appeared.

## 5.2 Experiments on CdTe cavities under non-resonant excitation

The onset of a spontaneous stimulation phenomenon in GaAs based cavities is unlikely to appear as the strong coupling in such cavities becomes saturated before the apparition of a non-linear transition. In 1996, Andre *et al.* realised the first microcavity in the CdTe material system working in the strong coupling regime [3]. The CdTe system appeared to be very promising, due to the large exciton oscillator strength, the Mott density of the exciton transition is about one order of magnitude above the one of GaAs. In fact, two years later Dang *et al.* demonstrated a non-linear stimulated effect

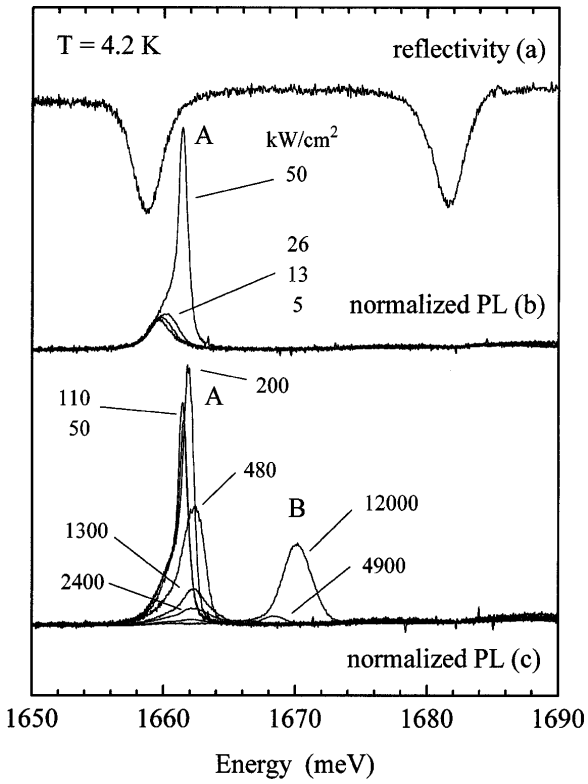


**Figure 5.1:** Reflectivity spectrum of a CdTe microcavity (curve (a)). Curves (b) show a set of normalised photoluminescence curves when pump intensity is varied between 5 and 50 $kW/cm^2$. Above 26 $kW/cm^2$ a non-linear threshold occurs. Curves (c) depict the appearance of an emission peak at the uncoupled cavity energy corresponding to the break down of the strong coupling regime. Data taken from ref. [33].

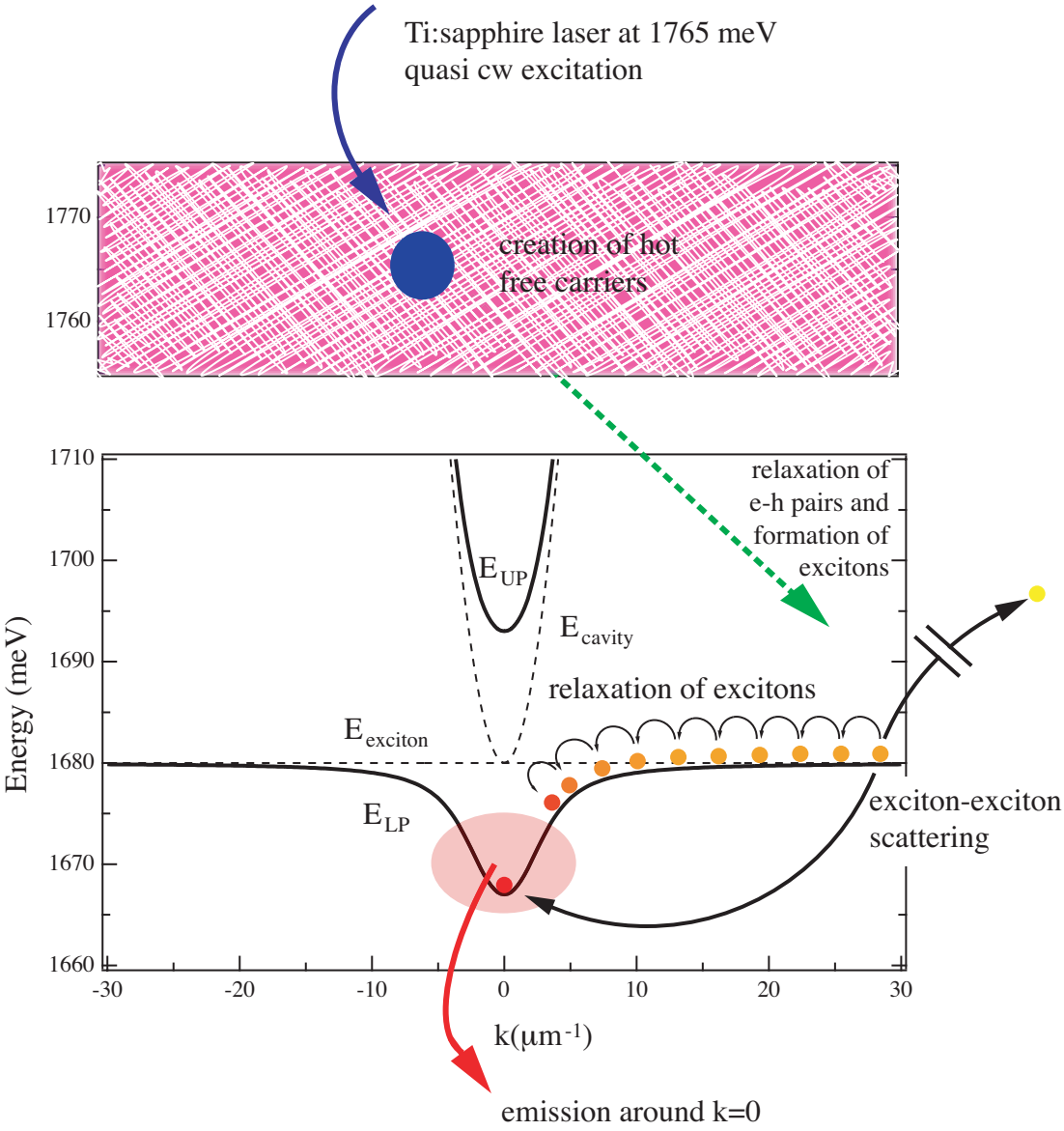


**Figure 5.2:** Relaxation mechanism in a II-VI CdTe microcavity. Hot free carriers are created by laser excitation. The electron-hole pairs cool down and form excitons with high in-plane momentum. The excitons relax emitting phonons and decay radiatively in the radiative region of the lower polariton dispersion. Porras *et al.* propose in reference [87] that at high pump intensity, an efficient exciton-exciton scattering mechanism supplies the $k = 0$ polariton state directly.

occurring in the strong coupling regime [33]. The measurement is shown on fig. 5.1. Curve (a) depicts the reflectivity spectrum of the employed cavity. It has a splitting of $26meV$, similar to the CdTe sample employed in the present work (see section 2.4.2). The sample was pumped non-resonantly at an energy of $\sim 1.8eV$, above the reflectivity stop band of the cavity. The normalised photoluminescence curves (b) show the photo-

luminescence spectrum from the cavity, when pumped between 5 and $50kW/cm^2$. At low excitation intensity ($5, 13, 26kW/cm^2$) the luminescence is emitted at the slightly blue-shifted lower polariton energy with a linewidth corresponding to the linear polariton linewidth as measured in reflectivity (curve (a)). Between 26 and $50kW/cm^2$, the photoluminescence emission shows a first non-linear threshold behaviour, accompanied by a line sharpening. This non-linear threshold clearly occurs in the strong coupling regime. The strong coupling regime breaks down about two orders of magnitude above the first non-linear threshold, as is manifest by the appearance of an emission peak at the energy of the uncoupled cavity energy ($\sim 1670meV$). This second emission also shows a non-linear threshold, which corresponds to the laser threshold of a conventional electron-hole pair vertical cavity surface emitting laser. The principle of the underlying relaxation mechanism for the non-linear emission in the strong coupling regime is depicted in fig. 5.2. A laser excites the cavity entering above the stop band of the Bragg-reflectors and creates electron hole pairs. The electron hole pairs cool down and form excitons with very large in-plane momentums. During this relaxation, the excitations lose any phase-coherence of the incident laser light. The excitons relax towards the bottom of the lower polariton dispersion at $k = 0$ by phonon emission. In the radiative region of the lower polariton dispersion, the polaritons decay radiatively and emit light. Porras and co-workers have proposed a non-linear mechanism for the relaxation of the hot excitons [87]. At high densities excitons with high energy and momentum can scatter with each other conserving both energy and momentum. Above the non-linear threshold, one exciton scatters into the $k = 0$ polariton state and another one to a high in-plane momentum state (see fig. 5.2). This process is similar to the parametric polariton scattering process investigated in chapter 3 and 4, with the difference that, here the scattering mechanism also involves states outside the lower polariton dispersion dip. The process becomes stimulated when the stimulated scattering rate into the $k = 0$ state becomes larger than its loss rate.

The transition was characterised by the measurement of the photoluminescence decay time. Below the stimulation threshold shown on curves (b) in fig. 5.1, the characteristic decay time was of the order of $100\,ps$, which is much longer than the radiative lifetime of the polaritons ($\sim 1\,ps$). Above threshold the photoluminescence decay-time dramatically decreased by about 30 times to $\sim 3\,ps$ [80].

Richard *et al.* characterised the coherence properties of the non-linear emission in the far-field [90]. They excited the cavity with a very small laser spot. At lower intensity, the directional emission in the Fourier plane was quite homogeneous, whereas at the non-linear threshold a well defined ring structure in the far-field built up. It was demonstrated, that the far-field emission of the cavity was strongly correlated in the Fourier plane above threshold, i.e. there was a spontaneous apparition of coherence. In a second paper [89], the intensity distribution of the emission spot was analysed using a large laser spot (fig. 5.3). Below threshold, the emission came from a large homogenous spot corresponding to the size of the laser spot ($22\,\mu m$, see panel (a)). Above threshold, the emission came from a number of bright spots with $\sim 3\,\mu m$-diameter (panel (b) and (c)). At the same time the angular width in the far field was measured for the non-linear emission (panel (b) and (c)). Corresponding to the laws of diffraction, a $3\,\mu m$-spot in real space, should present a broad angular width of at least $10°$. The measured angular

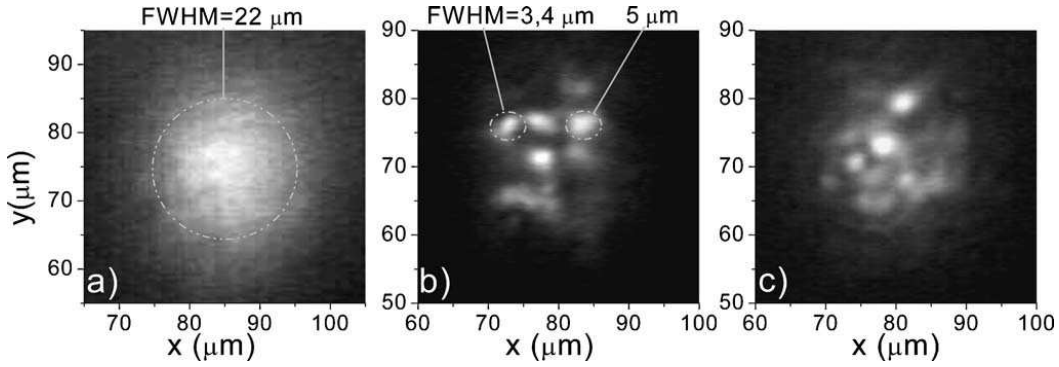


**Figure 5.3:** Images of the emission spot below threshold (panel a) and above threshold from two different points of the sample (panel b and c). The data is taken from [89].

width amounted to only 3.6°. This fact suggests, that there must be some correlation between the bright spots, i.e. a macroscopic phase-coherence over the whole spot. This feature of the non-linear emission is strongly connected to the present work. In the following we will discuss the basic properties of Bose-Einstein condensation of dilute atom gases and their relevance for the polariton system. Special emphasis will be put on the concept of long-range order.

## 5.3 Theoretical basics

### 5.3.1 Long-range order

A system which is charactersised by a statistical ensemble of states can be conveniently treated in the density matrix formalism [70]. The one-body density matrix can be defined as follows:

$$n^{(1)}(\mathbf{r},\mathbf{r}') = \langle \hat{\Psi}^\dagger(\mathbf{r})\hat{\Psi}(\mathbf{r}')\rangle, \tag{5.1}$$

where $\hat{\Psi}^\dagger(\mathbf{r})$ and $\hat{\Psi}(\mathbf{r}')$ are the field operators creating and annihilating a particle at point $\mathbf{r}$. The diagonal elements of the one-body density matrix describe the density of the system:

$$n^{(1)}(\mathbf{r}) = \langle \hat{\Psi}^\dagger(\mathbf{r})\hat{\Psi}(\mathbf{r})\rangle = n^{(1)}(\mathbf{r},\mathbf{r}) \tag{5.2}$$

The diagonal density and thus the field operators are normalised to the total number of particles ($N = \int \mathrm{d}\mathbf{r} n^{(1)}(\mathbf{r}) = \int \mathrm{d}\mathbf{r} n^{(1)}(\mathbf{r},\mathbf{r})$).

In our case, we study the properties of polaritons in a microcavity. The polaritons cannot be observed directly. Polaritons are coupled states between quantum-well excitons and cavity photon modes. These photon modes are coupled to the external world and can be measured by using optical methods. This light emitted by the cavity is a direct part of the polariton wave-function and thus carries the coherence and statistical

properties of the polaritons. For the experiments as presented in section 5.2, the microcavity emits light from a small spot. The intensity distribution of the light field $I(\mathbf{r})$ is equivalent to the diagonal elements of the density matrix 5.2. The spatial correlations of the polaritons are described by the first order coherence function $g^{(1)}$, which is the density matrix for the emitted photons. The first order spatial coherence function is defined to be,

$$g^{(1)}(\mathbf{r},\mathbf{r}') = \frac{\langle \mathbf{E}^*(\mathbf{r})\mathbf{E}(\mathbf{r}')\rangle}{\langle \mathbf{E}^*(\mathbf{r})\rangle\langle \mathbf{E}(\mathbf{r}')\rangle}. \tag{5.3}$$

The formal difference between $g^{(1)}$ and $n^{(1)}$ is that $g^{(1)}$ is normalised to the field values at $\mathbf{r}$ and $\mathbf{r}'$. In the case of $\mathbf{r} = \mathbf{r}'$, i.e. on the diagonal, $n^{(1)}$ corresponds to the particle density $n(\mathbf{r})$, the numerator in equation 5.3 is the emitted light intensity $I(\mathbf{r})$ and is proportional to $n(\mathbf{r})$ and thus $g^{(1)}$ equals 1.

The characteristic of Bose-Einstein Condensation is, that a large number of particles are in the same state and represented by the same wavefunction. The momentum distribution can be represented by the diagonal elements of the density matrix in momentum space

$$n^{(1)}(\mathbf{p}) = \langle \hat{\Psi}^\dagger(\mathbf{p})\hat{\Psi}(\mathbf{p})\rangle. \tag{5.4}$$

The momentum distribution $n^{(1)}(\mathbf{p})$ is often discussed in literature in the framework of the description of the ideal Bose gas. For high temperatures the momentum distribtuion can be described by the Maxwell-Boltzmann distribution. For low temperature, the distribution is described by the Bose-Einstein distribution. When the system is cooled down below a characteristic temperature $T_c$, the condensation temperature, the lowest energy state of the system is populated macroscopically, i.e. the occupation $N_0$ of this state becomes $>> 1$. The occupation of all the other states is of the order of or below unity. The momentum distribution then reads

$$n(\mathbf{p}) = N_0\delta(\mathbf{p}) + \tilde{n}(\mathbf{p}). \tag{5.5}$$

The observation of such a momentum distribution was the first clear evidence for Bose-Einstein Condensation in dilute atomic gases [2]. The momentum distribution measured in [2] is shown in fig. 5.4. Above $T_C$, the system is classic and a smooth momentum distribution is observed (front surface plot). For $T < T_C$, a sharp peak at zero momentum appears in the middle of the particle momentum distribution corresponding to the condensate (middle surface plot). When the thermal cloud "around" the condensate is evaporated, only the peak corresponding to the condensate remains (rear surface plot). The finite width of the condensate peak is due to the fact that the system has finite dimensions in real space corresponding to the size of the atom trap.

The measurement of the momentum distribution is also possible for the case of the microcavity. The in-plane momentum of the polaritons is proportional to their in-plane

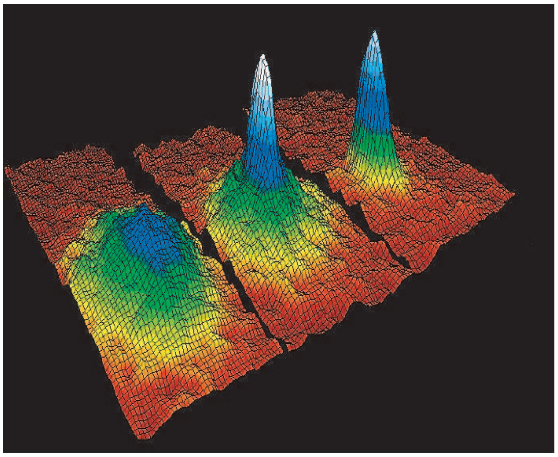

**Figure 5.4:** Atomic Bose Einstein Condensates. Momentum distribution of the condensate as measured by Anderson *et al.* in 1995 [2].

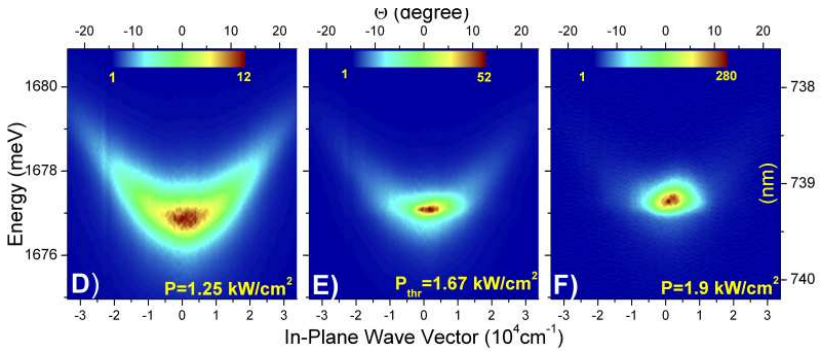


**Figure 5.5:** Luminescence from a CdTe microcavity measured under non-resonant excitation as explained in section 5.2. The horizontal and vertical scale depict respectively in-plane wavevector and energy. The intensity corresponds to a false colour scale shown on the top of each image. The first panel shows the emission at very low pump intensity, the second just below the non-linear threshold, and the third above the non-linear threshold. The data is a courtesy of Jacek Kasprzak of the University of Grenoble.

wave vector ($p = \hbar k$). Fig. 5.5 shows the momentum and energy-resolved photoluminescence of a CdTe-microcavity. The vertical axis displays the emission energy, whereas the horizontal axis shows the in-plane wavevector of the polaritons. At low intensity, the emission appears all along the lower polariton dispersion, and is broadly distributed in k-space. At higher intensity, below threshold, the emission becomes more concentrated around $k = 0$ (panel E). Above threshold, the emission comes almost exclusively from $k = 0$ (panel F), which corresponds to the appearance of a macroscopically occupied state at $k = 0$. This feature corresponds to the mid plot of figure 5.4 in which the momentum distribution of a Bose-Einstein condensate of atoms is shown.

The coupling of the polariton modes depends on their respective wavevectors. To measure the occupation number of the polariton states, the photoluminescence intensity in fig. 5.5 was normalised using the Hopfield factors $C_k$. The occupation of the states

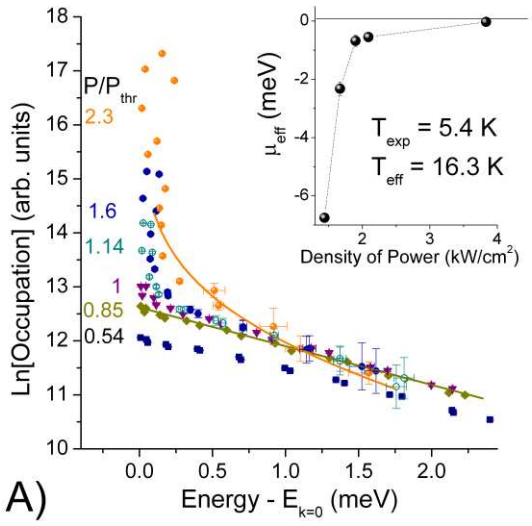


**Figure 5.6:** Population of the polariton states versus $E - E_{k=0}$ normalised accounting for the Hopfield factors. To obtain the data, measurements similar to those presented in fig. 5.5 have been used. The data is a courtesy of Jacek Kasprzak of the University of Grenoble.

was calculated corresponding to $n = I_{PL}(k)/C_k^2$. The occupation of the polariton states at different pump intensities is depicted in fig. 5.6 on a logarithmic scale. At low pump intensities, which corresponds to a boson gas below the condensation density, the distribution exhibits an exponential behaviour corresponding to a Maxwell-Boltzmann distribution. When the pump intensity reaches threshold, the distribution features a shape corresponding to a Bose-Einstein distribution. At low energies and high pump intensities, a macroscopic occupation of the lowest energy state at $k = 0$ is observed. The fit of a Bose-Einstein distribution to the experimental points does not work at small energy. The occupation of the lowest energy states is much higher than the value of the Bose-Einstein distribution fit. This behaviour is also observed in numerical calculations and can be attributed to the strong interactions of the polaritons[2]. Before retrieving the basic theoretical discussion, we point out, that the two presented data sets presented in fig. 5.5 and 5.6 qualitatively correspond to the behaviour observed in the dilute atomic system (fig. 5.4).

The singularity of the momentum distribution of the particles has a profound consequence for the properties of the one-body density matrix $n^{(1)}(\mathbf{r}, \mathbf{r}')$ in real space, which is the appearance of off-diagonal long-range order. This concept was introduced in the 1950s by Penrose and Onsager [85, 86]. The diagonal elements of the one-body density matrix can be written in momentum space as in eq. 5.4. It is convenient, to consider a system in the thermodynamic limit, which is uniform and isotropic [3]. In such a case,

[2] private communication with Davide Sarchi

[3] This discussion is useful to understand the origin of the spatial coherence of a 3-dimensional ideal Bose-Einstein condensate. The reader should keep in mind, that the polariton system is basically a non-uniform 2-dimensional system.

the one-body density matrix depends only on the modulus of the relative displacement $s$ between points $\mathbf{r}$ and $\mathbf{r}'$ ($s = |\mathbf{r} - \mathbf{r}'|$) and reads

$$n^{(1)}(\mathbf{r}, \mathbf{r}') = n^{(1)}(s) \tag{5.6}$$

The dependence of $n^{(1)}(s)$ on the momentum distribution can be written as (see chapter 2 of [70]),

$$n^{(1)}(s) = \frac{1}{V} \int \mathrm{d}\mathbf{p}\, n(\mathbf{p}) \mathrm{e}^{-\mathrm{i}\mathbf{p}\cdot\mathbf{s}/\hbar}. \tag{5.7}$$

When the momentum distribution equation 5.5 is inserted into equation 5.7, we get

$$n^{(1)}(s) = \frac{N_0}{V} + \frac{1}{V} \int \mathrm{d}\mathbf{p}\, \tilde{n}(\mathbf{p})\, \mathrm{e}^{-\mathrm{i}\mathbf{p}\cdot\mathbf{s}/\hbar} \tag{5.8}$$

The contribution of the condensate is a constant term, whereas the second term characterises a smooth distribution with a width of about the thermal wavelength of the non-condensed particles. For large distances $n^{(1)}(s)$ tends to a constant value $n_0 = N_0/V$, which is a consequence of the momentum singularity of the condensate. The macroscopic occupation of a single particle state is a general definition of a BEC and the off-diagonal long-range constancy of the density matrix $n^{(1)}(\mathbf{s})$ is a direct consequence of that. This property of the density matrix reflects the presence of a long-range order in the system.

In a beautiful experiment, the long range order, i.e. the decay of $n^{(1)}(s)$ towards a non-zero constant value was demonstrated in reference [12]. The measurement is shown in fig. 5.7. In the experiment, two parts of a $\sim 1\mu m$ large condensate have been extracted at a distance $\Delta z = z_2 - z_1$ containing $N_1$ and $N_2$ particles. The two condensates carrying the phase of the original $1\mu m$-condensate at positions $z_1$ and $z_2$ were then superimposed. Because of the correlation in the original condensate, the superposition showed interference fringes having a contrast

$$\gamma^{(1)}(s) = \frac{n^{(1)}(s)}{\sqrt{N_1}\sqrt{N_2}}, s = |\Delta z| \tag{5.9}$$

In a thermal non-condensed gas having approximately a Maxwell-Boltzmann distribution, the density matrix and thus $\gamma^{(1)}(s)$ shows a Gaussian shape corresponding to,

$$\gamma^{(1)}(s) \propto e^{-\frac{\pi s^2}{\lambda_T^2}}, \tag{5.10}$$

for the curves with the open symbols ($T = 450\,nK, T = 290\,nK$) in figure 5.7. $\lambda_T$ is the thermal wavelength of the classical gas corresponding to $\lambda_T = \sqrt{\frac{2\pi\hbar^2}{m k_B T}}$ [70].

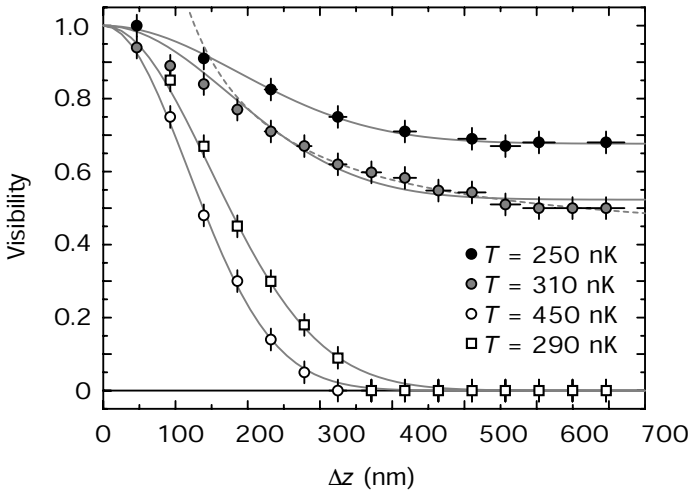


**Figure 5.7:** Decay of the visibility (contrast) of interference fringes of two condensates cut at distance $\Delta z$ out of a larger condensate. Data taken from [12], for different temperatures and densities.

When the temperature of the gas was lowered below $T_c$, the contrast $\gamma^{(1)}(s)$ of the fringes between the cut condensates decayed to a constant non-zero value (see fig. 5.7, curves with solid symbols). The visibility for the condensed gas on fig. 5.7 approaches in fact values $> 50\%$ for distances $\Delta z$ more than four times the thermal wavelength of the non-condensed atoms. The data in fig. 5.7 agree with the behaviour displayed in equation 5.8 and directly demonstrates the appearance of long range order, a concept developed more than 50 years ago.

### 5.3.2 Order parameter of the condensate

Let us consider a system consisting of an ensemble of bosons. It is possible to find an otrtho-normalised basis of single-particle wavefunctions $\varphi_i(\mathbf{r})$ for the system [70]. The field operator $\hat{\Psi}(\mathbf{r})$ used in eq. 5.1 can then be written in terms of these wavefunctions $\varphi_i$ and the corresponding annihilation and creation operators $\hat{a}_i$ and $\hat{a}_i^\dagger$:

$$\hat{\Psi}(\mathbf{r}) = \sum_i \varphi_i\hat{(}\mathbf{r})a_i, \tag{5.11}$$

where $\varphi_0$ is the wavefunction of the lowest energy state. In a condensed system, it characterises the wavefunction of the condensate. It is convenient to write the field operator with the condensate wavefunction separate from the rest of the sum:

$$\hat{\Psi}(\mathbf{r}) = \varphi_{i,0}(\mathbf{r})\hat{a}_{i,0} + \sum_{i\neq 0} \varphi_i(\mathbf{r})\hat{a}_i. \tag{5.12}$$

When the system is condensed, the occupation of the lowest energy state is macroscopic and the corresponding operators ($\hat{a}_i$ and $\hat{a}_i^\dagger$) can be replaced by c-numbers$\sqrt{N_0}$.

This approximation is known as the Boguliubov approximation and the field operator reads,

$$\hat{\Psi}(\mathbf{r}) = \Psi_0(\mathbf{r}) + \delta\hat{\Psi}(\mathbf{r}) \tag{5.13}$$

where $\Psi_0(\mathbf{r}) = \sqrt{N_0}\varphi_0$ and $\delta\hat{\Psi}_0(\mathbf{r}) = \sum_{i\neq 0}\varphi_i(\mathbf{r})\hat{a}_i$. $\Psi_0$ is a classical field, whereas $\delta\hat{\Psi}(\mathbf{r})$ is a field operator. $\Psi_0(\mathbf{r})$ is the so-called wavefunction of the condensate and plays the role of an order parameter. It can be written as a complex quantity characterised by a modulus and a complex phase factor:

$$\Psi_0(\mathbf{r}) = |\Psi_0(\mathbf{r})|\, \mathrm{e}^{\mathrm{i}\mathbf{S}(\mathbf{r})} \tag{5.14}$$

The order parameter given in equation 5.14 can be multiplied by an arbitrary phase factor $e^{i\alpha}$ without changing the physical properties of the system. This reflects the gauge symmetry of the system. Choosing a specific phase corresponds to the formal breaking of the gauge symmetry.

The wavefunction of the expected polariton condensate is observable outside the cavity as a classical electromagnetic field. Being a transverse field, this light field is also characterised by a polarisation. The scalar wavefunction given by 5.14 must thus be replaced by a vector field characterising magnitude and direction of the field components.

### 5.3.3 Quantum statistical properties of the condensate

A non-condensed thermalised system in a thermal state is described by a Maxwell-Boltzmann distribution. At the phase-transition, the lowest energy state of the system becomes macroscopically populated. The field operators of the lowest energy state can be replaced by a classical field $\Psi_0$, which is a coherent state representing the condensate [13]. The Bose-Einstein condensation is thus a transition from a thermal to a single mode coherent state. As stated before, the polaritons decay into photons, carrying information about the quantum statistical properties of the polaritons. The statistics can be investigated performing Hanburry-Brown-Twiss or noise measurements. When the system is in a thermal state, the value of the second order coherence function $g^{(2)}$ is expected to be 2, whereas for a coherent state, $g^{(2)}$ equals 1 [75, 4]. In a concrete experiment, $g^{(2)}$ should jump from a value between 1 and 2 below threshold to $\sim 1$ just above threshold in an abrupt way. In [39], the second order coherence of the polariton emission has been studied. In this study the condensate transition is not conclusive, since the behaviour of $g^{(2)}$ with exciting intensity is very smooth and the minimum value of $g^{(2)}$ is 1.5 at $I_{pump} = 18I_{th}$. Furthermore, at very high densities ($I_{pump} = 18I_{th}$), strong interactions in the condensate are expected. These interactions (Coulomb interaction between excitons, etc.) tend to add noise to the signal, such that $g^{(2)}$ should increase at high density.

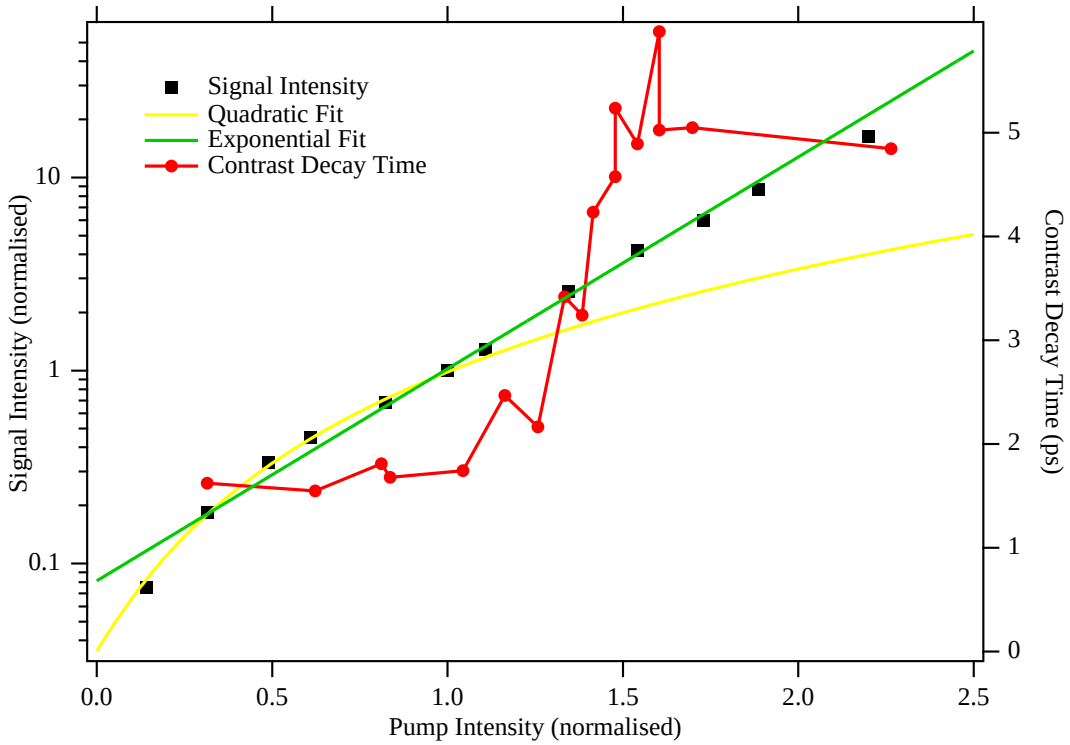


**Figure 5.8:** Signal intensity and contrast decay time versus pump intensity. The signal intensity is fitted by a quadratic fit below threshold and by an exponential fit above threshold. The decay time of the contrast makes a jump approximately at the threshold intensity.

## 5.4 Life time of the polaritons

In the previous introduction in section 5.3, the basic properties of Bose-Einstein condensation were discussed illustrated by their relevance for Bose-Einstein condensation in dilute atomic gases and the polariton system. One issue not yet adressed is the finite lifetime of the condensed phase. The lifetime of atomic Bose-Einstein condensates is of the order of a few seconds. In these condensates, the loss mechanism is the evaporation of atoms out of the condensed phase. During the whole time (before, during condensation, during evaporation, and after), the system consists of a condensed phase plus a bath of non-condensed atoms.

The polariton system is fundamentally different. The polaritons form from ionised electron-hole pairs created by a non-resonant laser excitation (see section 5.2). Due to their coupling to external light modes, a large amount of polaritons decay into light during their relaxation towards the lowest energy state at $k = 0$. When the threshold for the non-linear relaxation of the polaritons is passed, the relaxation time of the polaritons becomes quicker than their lifetime [80] and polaritons accumulate in the lowest energy state at $k = 0$. The coherence time of this state is expected to change at threshold, since it is continuously re-supplied by the non-linear relaxation.

To measure these dynamical features, an interferometric measurement of the decay

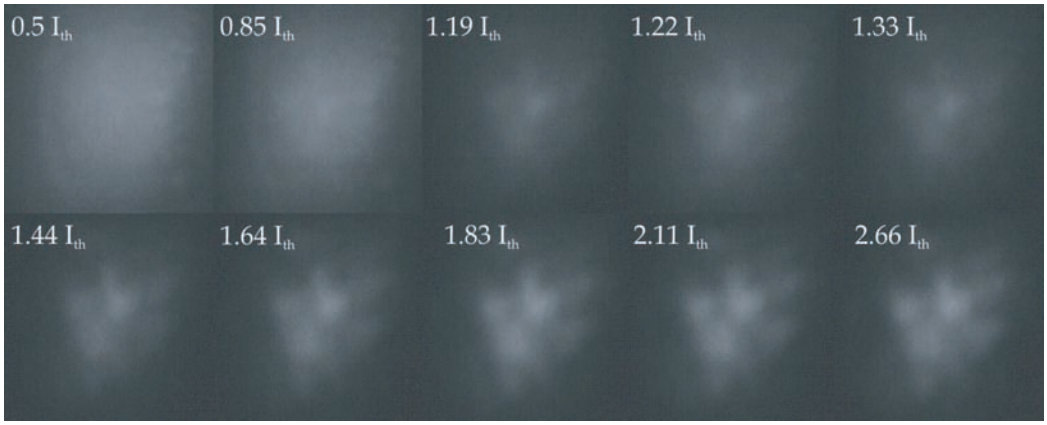


**Figure 5.9:** This series of images show real-space images of the excited area on the sample when the pump intensity is varied ($I_{th}$ is the threshold pump intensity for the non-linear emission). The intensity scale has been adjusted differently for each image to show the intensity profile of the emission. Above threshold a structured emission pattern builds up with three distinct bright spots.

time of the contrast has been performed, similar to that in section 4.4. The employed setup is the same as the one depicted in fig. 4.17, with the difference, that the laser excites the sample non-resonantly and the signal is detected in reflection and not in transmission geometry (see fig. 5.10). In this geometry, the stray laser light co-propagates with the signal through the whole detection setup. To remove the contribution of the stray laser light, the output of the interferometer is filtered using a $30\,cm$ monochromator before it reaches the photodiode.

The measurement of the signal emission intensity around $k = 0$ and its contrast decay time versus the incident pump intensity is depicted in fig. 5.8. The signal intensity (black squares) fits well with a quadratic evolution at low pump intensity and has an exponential shape above the stimulation threshold. A quadratic behaviour is the signature of a scattering process. It is probable that the scattering process is an exciton-exciton scattering process as proposed by Porras *et al.* in reference [87]. The process cannot be identified in the experiment, since the high in-plane momentum exciton states cannot be investigated in the experiment. At low intensity, one would expect a linear dependence of the signal intensity (as measured in [33]), as the polaritons will relax by phonon emission. Our measurement setup was not sensitive enough to record in this regime. The coherence time, which corresponds approximately to the polariton radiative lifetime is around $1.7\,ps$ at low pump intensity. This agrees well with the linear polariton linewidth of the cavity. Above the threshold the lifetime rises strongly to about $5\,ps$. The behaviour seems to be quite similar to the one observed in the parametric scattering of polaritons (section 4.4). The difference here is that the phase coherence of the laser has been completely lost by the incoherent relaxation mechanism. This enhancement of the lifetime must then be connected to the spontaneously acquired coherence of the polaritons.

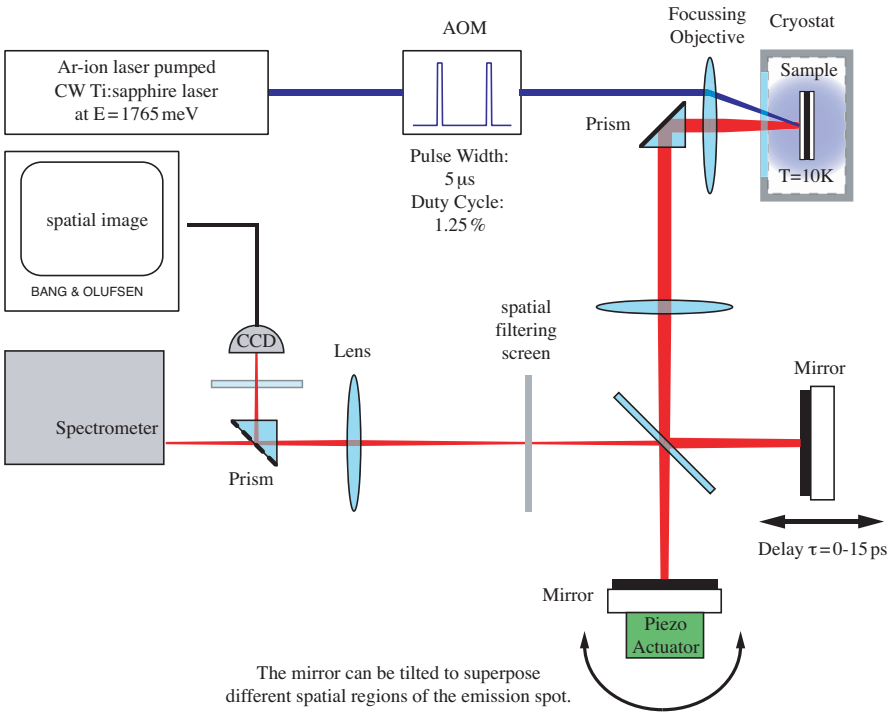


**Figure 5.10:** Setup for the measurement of the spatial and temporal correlations.

## 5.5 Spatial correlations of the condensate

As it has been pointed out in section 5.3, the appearance of long-range order is a key feature of Bose-Einstein condensation. Initially, we analyse the intensity distribution of the emission spot.

### 5.5.1 Real space shape of the intensity distribution

Fig. 5.9 shows the intensity distribution of the emission spot when the pump intensity is varied. Below threshold we observe a uniform circular emission spot with the dimensions of the laser spot (diameter $25\,\mu m$). For a rising pump intensity a pattern forms, giving rise to three distinct spots above threshold. The angular width of the emission in k-space (not shown here) is of the order of $3-4°$. This corresponds to the observations in reference [89] shown in fig. 5.3, and is an evidence for a correlation between the spots. The non-uniformity of the spot can be attributed to the strong static disorder present in the sample (fluctuations of the cavity width and the Bragg mirror quality). A detailed discussion can be found in [89].

### 5.5.2 Setup for the spatial coherence study

To probe directly the spatial coherence of the spot, we need to look at the interference between the bright spots. To do so the interferometer setup used before for the lifetime

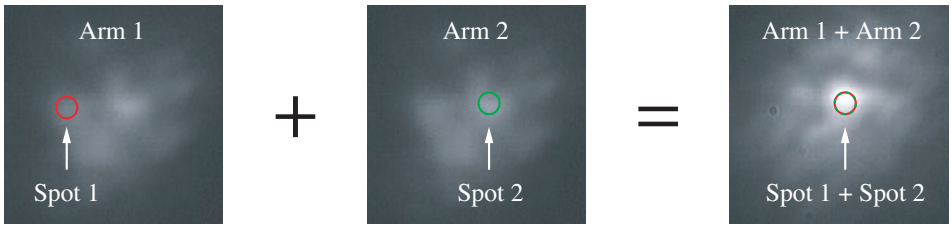


**Figure 5.11:** Superpostion of the real-space images of the two interferometer arms.

measurements has to be modified. Fig. 5.10 shows the setup. As in the previous experiments, the pump laser hits the sample at an angle of $\sim 10°$. The off-normal incidence of the laser is chosen to avoid laser light to be reflected to the detector by the setup (this does not influence the physics of the relaxation since we excite non-resonantly). The laser beam is chopped by an acousto-optic modulator to avoid heating the sample. The duty cycle for the illumination is 1.25% and the pulse duration is quasi CW since it amounts to $5\,\mu s$, which is long compared to the time scales of the relaxation and the emission. The polariton emission is collected by a focusing objective and sent by a prism to a lens. This lens, together with the objective, images a real space image of the sample surface onto the spatial filtering screen. Between the lens and the screen, the converging beam passes a Michelson interferometer. The orientation of the interferometer mirrors enables us to move the relative position of the two images on the screen. If the two out-coming beams of the interferometer are collinear, we superpose each point of the whole emission spot with itself (as done for the measurement in section 5.4). Tilting a mirror shifts one image with respect to the other and thus superposes different points of the sample. Points can be selected using a double slit spatial filter in the image plane. The plane of the spatial filter is re-imaged by a third lens onto a CCD video camera or the entrance slit of a spectrometer (by using or not a prism). The real space image of the spot can be monitored on the CCD. The spectrometer is equipped with a Si-diode connected with a synchronous detection with a high sensitivity. The spectrometer is needed to be able to measure the correlations in the spot below threshold. In this case, the stray-light of the laser captured by the optics is stronger than the polariton signal to be measured. The CCD is used to look at the emission at much higher signal intensities, and thus a simple polariser is sufficient to cut out the stray laser light.

In figure 5.11 we explain how the differrent parts of the image are superimposed. The emission zone contains three bright spots. Initially we choose to make interfere the two horizontally distributed ones. We superpose the first arm of the interferometer with the left spot with the right spot of arm 2. The spatial filtering double slit is used to select only the region of interest, where the two spots overlap ("Spot1 + Spot2" on the right panel in fig. 5.11).

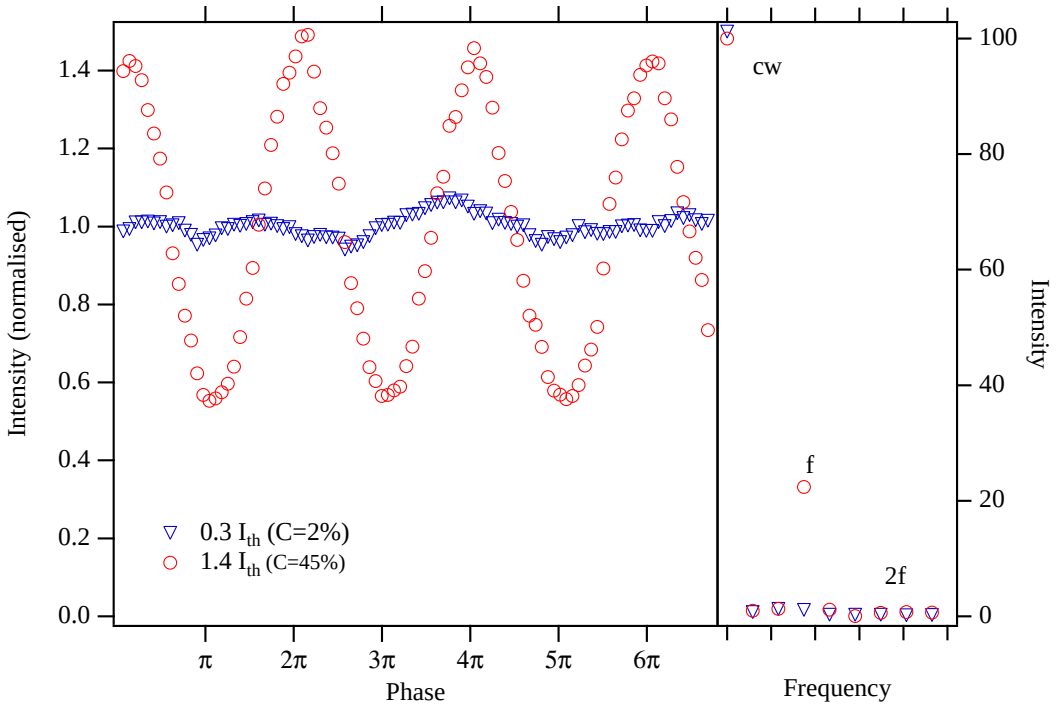


**Figure 5.12:** Normalised intensity of the signal at the output of the interferometer at "Spot1 + Spot2" when the relative phase between the interferometer arms is scanned (left panel). The right panel shows a Fourier transform of the data on the left.

### 5.5.3 Spatial long range order of the emission

First, it is qualitatively explored how the first order correlation between spot 1 and spot 2 evolves (configuration third panel, fig. 5.11). To do so, we show a measurement of the detected intensity after the spectrometer when the relative phase of the two arms of the interferometer is scanned. The phase is changed using the piezo actuator and the PI-stabilisation as in the former experiments (see appendix A). The measurement is shown in fig. 5.12. The left panel shows the intensity oscillations when the relative phase is scanned. The right panel displays the fast Fourier transform of the left panel. When the pump intensity is adjusted to $0.3\,I_{th}$, no distinct interference fringes are observed. When the pump intensity is increased to $1.4\,I_{th}$ perfect sinusoidal oscillations are observed, implying a strong correlation of the two emission spots. The contrast of the oscillations representing $g^{(1)}(Spot1, Spot2, I_{pump})$ is calculated using the Fourier spectrum on the right panel. The spectrum has a strong cw component and a strong component at the fundamental frequency of the oscillations. The spectrum also contains negative frequencies, but it is symmetric with respect to the zero frequency ($I(-f) = I(f)$). To compute the contrast, one has to use the cw intensity and the intensity at $f$ corresponding to

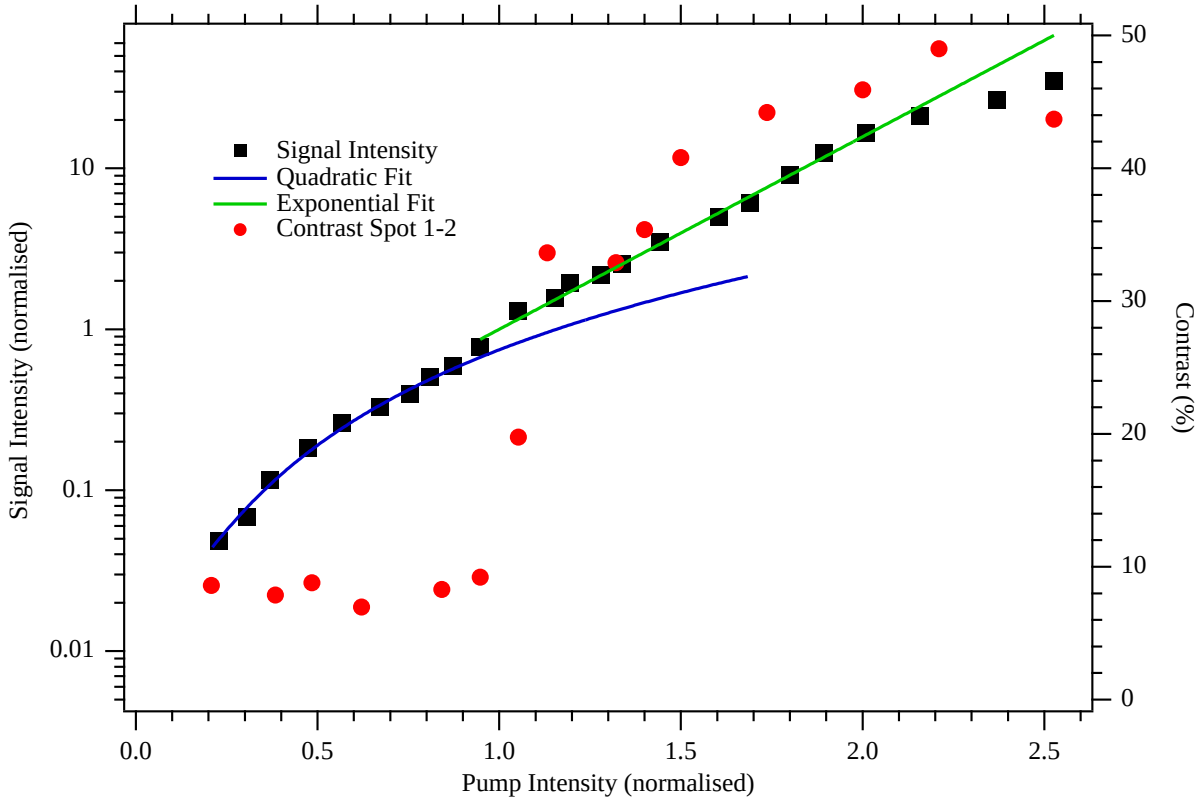


**Figure 5.13:** Signal emission intensity and contrast versus pump intensity. Signal emission intensity and pump intensity are normalised to their respective values at threshold. The signal intensity is fitted by a quadratic fit below threshold and by an exponential fit above threshold. The contrast between the two spot 1 and 2 makes a jump at about the threshold intensity.

$$Contrast = g^{(1)}(Spot1, Spot2, I_{pump}) = \frac{2I(f)}{I(cw)} \tag{5.15}$$

Using this method, the contrast is approximately 2% below and 45% above threshold. This means that the correlation $g^{(1)}(Spot1, Spot2, I_{pump})$ is multiplied by a factor of more than 20 at threshold for the two spots having a distance of $\sim 15\mu m$.

To do a more detailed quantitative analysis, the contrast measurements are repeated for several different pump intensities, and the contrast values are represented in graph 5.13 which also shows the signal intensity behaviour. In this plot the contrast has been evaluated by simply taking the minimum and the maximum of the interference fringes ($C = \frac{I_{max}-I_{min}}{I_{max}+I_{min}}$ ). This technique leads to an overestimation of the contrast below threshold, since the noise which is not correlated to the fringes enhances the contrast value (using this technique one obtains 5% of contrast at $0.3\,I_{th}$ in fig. 5.12 and 46% above threshold).

As in the former measurements, the intensity has a quadratic behaviour below, and an exponential behaviour above threshold. The exponential rise occurs between 1 and

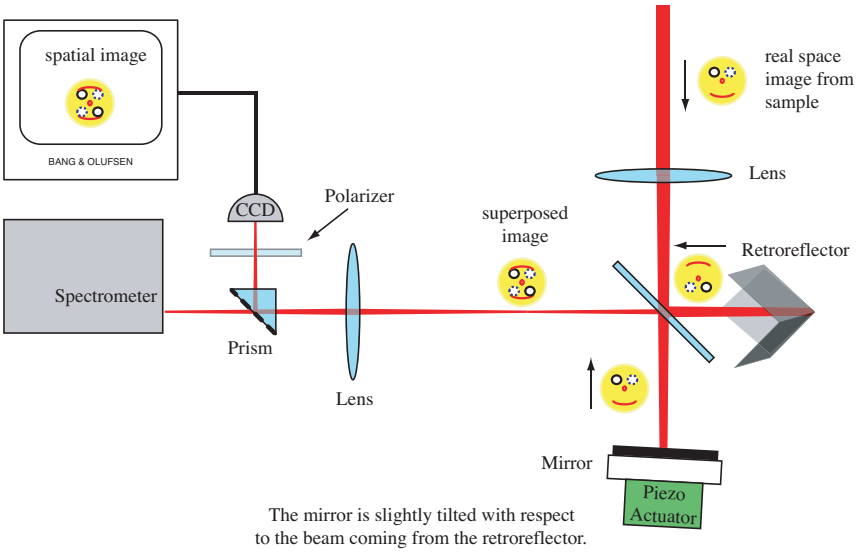


**Figure 5.14:** Setup for the mapping measurement of the spatial correlations. The mirror in one of the interferometer arms is replaced by a retroreflector. This has the effect that the image is reflected point-symmetrically in the arm containing the retroreflector. At the output different regions of the emission spot are superimposed, and the spatial correlation can be measured using the CCD camera.

$2\,I_{th}$. Above $2\,I_{th}$, the signal intensity slightly saturates. Below threshold the contrast stays constant at $\sim 8\%$ (this value is strongly overestimated as stated before). At threshold it quadruples to more than 30% and grows to almost 50% around $2\,I_{th}$[4]. The presence of interference of the light emitted by two spatially distant spots is a direct evidence of coherence, i.e. long-range order inside the excited volume. The contrast of the fringes is a quantitative measure of this order. The appearance of long-range order is a very strong argument for the occurrence of Bose-Einstein condensation in the polariton system.

### 5.5.4 Mapping of the spatial long range order

The correlation between spot 1 and spot 2 change dramatically from almost zero below threshold to a value of almost 50% above threshold. To obtain a more complete mapping of the first order correlation, the interferometer setup must be modified. As indicated in fig. 5.14, the mirror in one of the interferometer arms is replaced by a retroreflector, whilst the rest of the setup in fig. 5.10 remains unchanged. The effect of the retroreflector is indicated by the smiling face in fig. 5.14. The retroreflector changes the orientation of the face point-symmetrically with respect to the nose. This means, that at the output of the interferometer, we superimpose point $\mathbf{r}$ of the image with point $-\mathbf{r}$ of the other with the origin $\mathbf{0}$ being the centre of the retroreflector. As before, the relative delay of the two arms is zero, and we can thus measure the quantity

[4]The measurement presented in fig. 5.12 does not fit into graph 5.13 as the data are not from the same set of measurements.

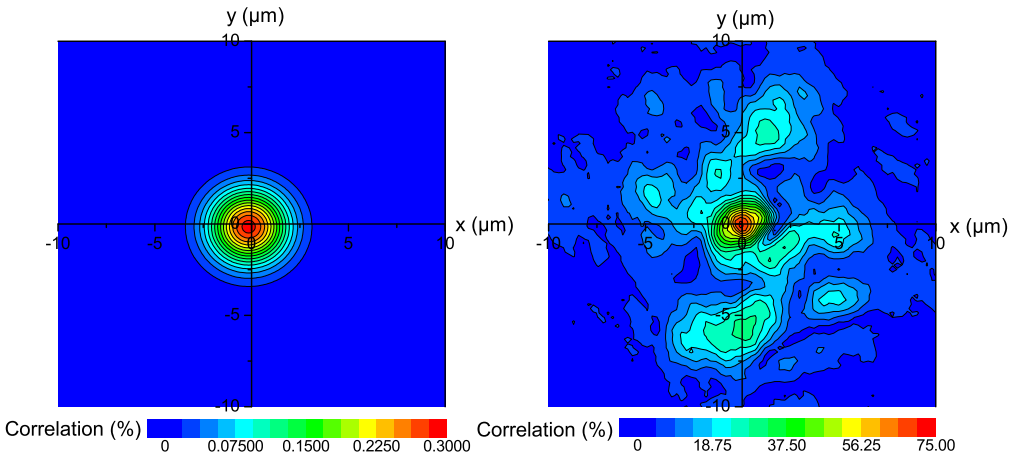


**Figure 5.15:** Mapping of the first order spatial coherence $g^{(1)}(\mathbf{r}, -\mathbf{r}, \mathbf{0})$ above (left panel) and below threshold (right panel). The false colour scales depict the correlation contrast.

$g^{(1)}(\mathbf{r}, -\mathbf{r}, \mathbf{0})$. To measure $g^{(1)}$, the two superimposed images are detected by a CCD video camera. When scanning the phase, the intensity versus phase on each pixel is recorded and the contrast value is computed using the same method as in fig. 5.12.

The $g^{(1)}$-mapping is depicted in fig. 5.15. The origin of the axes correspond to the symmetry centre of the retro-reflector. At this point, the image shows the auto-correlation $g^{(1)}(\mathbf{0}, \mathbf{0}, \mathbf{0})$. The correlation amounts here to $\sim 75\%$, which is not too far from the ideal value of 100%, if we take into consideration the triple reflection in the retro-reflector. The image is point symmetric with respect to the centre. The two horizontal maxima at $x = \pm 5\,\mu m$ correspond to the superpostion of spot 1 and spot 2 in the former measurement. We can identify two additional maxima of about 40% in the vertical direction, $\sim 7\,\mu m$ away from the origin, corresponding to a $\sim 14\,\mu m$ distance between the corresponding areas. These long-range spatial correlations have to be compared to the spatial correlation below threshold.

To get the spatial correlation below threshold, we have to use a different method, since the superimposed pictures of arm 1 and 2 were not scanned in phase. An image of the superimposed two images is shown on the left in fig. 5.16. We observe a more or less uniform spot with a region in the middle featuring vertical fringes, corresponding to the centre of the retro-reflector. The fringes are approximately vertical, since the planar mirror is slightly tilted with respect to the direction of the beam coming from

the retro-reflector. This allows for the evaluation of the contrast in a single image. An intensity profile of the image following the white line is taken and displayed on the right in fig. 5.16. The image intensity of one interferometer arm has a Gaussian shape

$$I(\mathbf{x}) = I_0 \cdot e^{-\frac{x^2}{r_{spot}^2}} \tag{5.16}$$

modulated by the spatial correlation $g^{(1)}(x)$. For $g^{(1)}$ we suppose a Gaussian shape (eq. 5.10)

$$g^{(1)}(x) = a \cdot C(x) = a \cdot C_{max} \cdot e^{-\frac{\pi x^2}{(\lambda_T)^2}}. \tag{5.17}$$

$g^{(1)}(x)$ is related to the measured contrast by a constant $a$ accounting for the imperfections of the interferometer setup. The intensity of the interference image is given by the interference formula for partially coherent light [16]

$$I(\theta) = I_1 + I_2 + \sqrt{I_1}\sqrt{I_2}\frac{g^{(1)}(\mathbf{x})}{a} cos\theta. \tag{5.18}$$

Inserting 5.17 into 5.18 and supposing $I_1 = I_2$, the resulting expression reads:

$$I(x) = I_0 \cdot e^{-\frac{x^2}{r_{spot}^2}} \cdot (2 + C_{max} \cdot e^{-\frac{\pi x^2}{(\lambda_T)^2}} \cdot cos(kx + \theta)), \tag{5.19}$$

where $k$ characterises the fringe separation and $\theta$ is a constant phase factor. The intensity behaviour in fig. 5.16 can be fitted (red line) by putting $d_{spot} = 2r_{spot} = 24\mu m$ and $\lambda_T = 4\mu m$. According to equation 5.17 we can plot $g^{(1)}(\mathbf{r}, -\mathbf{r}, \mathbf{0})$ because of the central symmetry:

$$\frac{g^{(1)}(\mathbf{r}, -\mathbf{r}, \mathbf{0})}{a} = C_{max} \cdot e^{-\frac{\mathbf{r}^2}{(1/2\lambda_{th})^2}} \tag{5.20}$$

The plot is shown in fig. 5.15 right panel. According to the theoretical introduction in section 5.3, the width of the central maximum corresponds to the thermal wavelength which amounts to $\lambda_T = 4\,\mu m$. Using the relation for $\lambda_T$ presented in section 5.3, the effective energy can be estimated. The estimation gives a temperature of $\sim 20K$ which is approximately the same as that found from the fit of the Bose distribution in fig. 5.6.

### 5.5.5 Spatial correlation and condensate fraction

In secton 5.3 experimental data for the spatial correlation of atomic Bose-Einstein condensates has been shown (fig. 5.7). As predicted from theoretical considerations of an infinite and homogeneous system, the contrast of the intensity fringes between the two cut condensates approached a constant value. The populations of the two

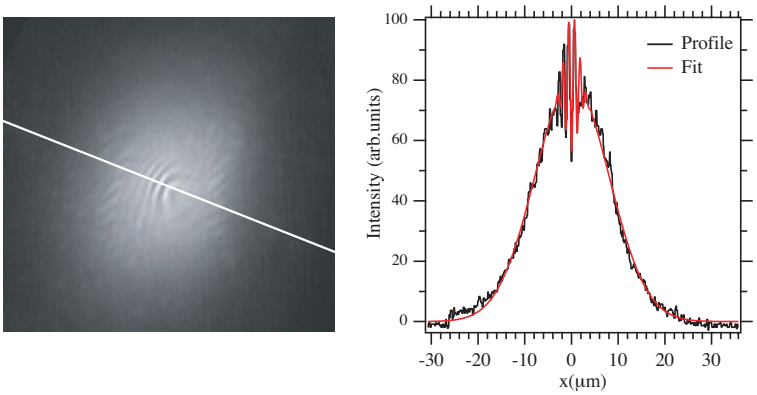


**Figure 5.16:** Image of the emission spot at the output of the interferometer. On the right, a profile of the image intensity along the white line in the image is shown. The image intensity profile (black) can be fitted corresponding to equation 5.18 (red curve).

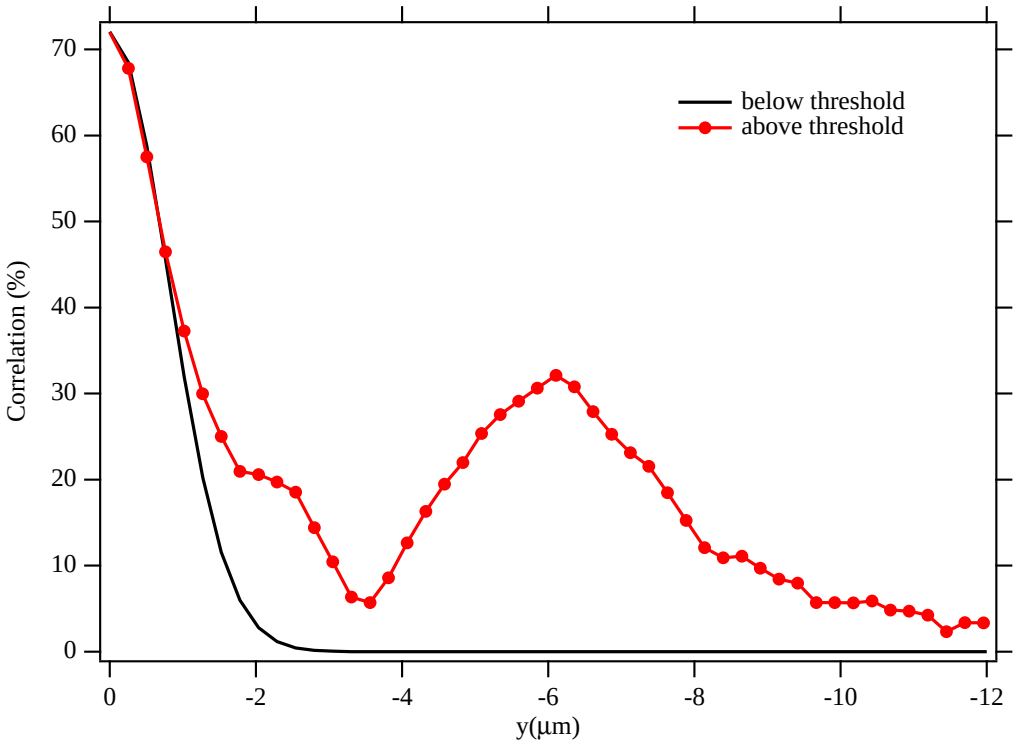


**Figure 5.17:** Transverse profile of the correlation function $g^{(1)}(\mathbf{r}, -\mathbf{r}, \mathbf{0})$ below and above threshold, extracted from the data presented in figures 5.15 and 5.16.

interfering condensates were equal ($N_1 = N_2$) and also the condensate fraction could be assumed to be the same at points $z_1$ and $z_2$. This allowed the visibility $\gamma^{(1)}(s)$ to be related directly to the condensate fraction $N_0/N$.

For the microcavity system the condition of homogeneity is not fulfilled (see fig. 5.3 and 5.9). Nevertheless, we still can analyse the transverse profile of the correlation

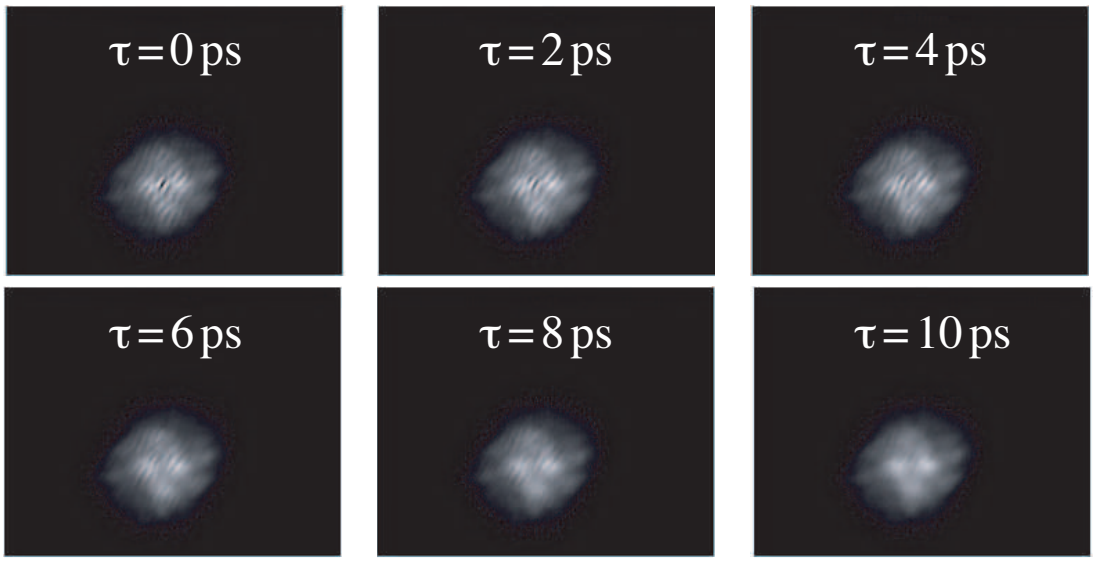


**Figure 5.18:** Images of the superimposed pictures of the two interferometer arms, when the delay between the arms is varied. At zero delay distinct fringes are observed. With increasing delay, the fringe contrast diminishes and at $\tau = 20\,ps$ the contrast is almost zero.

which is shown in fig. 5.15. The profile for the negative y-axis in fig. 5.15 is plotted in fig. 5.17. Below threshold, the correlation decays corresponding to the thermal wavelength of the polaritons of $4\mu m$. Above threshold, the correlation shows a peak value of more than 30% at $y = -6\mu m$. At this distance there is no correlation at all in the non-condensed case (below threshold). Between zero and the maximum correlation value, the correlation has a minimum of 5% and below $y \sim -8\mu m$ the correlation amounts to less than 10%. In the measurement, a point at $\mathbf{r}$ has been superimposed with a point at $-\mathbf{r}$ and the emission intensity at $\mathbf{r}$ and $-\mathbf{r}$ were generally not equal. Consequently the value of the correlation does not directly represent the condensate fraction. Nevertheless, it is a lower bound for the condensate fraction at $\mathbf{r}$ or $-\mathbf{r}$. At $-6\mu m$ the correlation amounts to 30%, which means that in one of the two regions ($\mathbf{r} = (0; 6\mu m)$ or $\mathbf{r} = (0; -6\mu m)$) the condensate fraction is at least 30%. To overcome the problem of the inhomogenous intensity, one would need to normalise the correlation using the respective intensity shapes of the images from the two interferometer arms. There is no reason why in an inhomogeneous system that the condensate fraction does not vary in space. To get a mapping of the condensate fraction, the origin of the retroreflector would need to be scanned so to superpose $\mathbf{r}$ with a different $\mathbf{r}'$ and thus obtain information about the relative condensate fraction between two different points $\mathbf{r}'$.

### 5.5.6 Temporal and spatial coherence of the condensate

In section 5.4 the evolution of the decay of the temporal coherence $g^{(1)}(\tau)$ has been measured. It was found, that the coherence time of the condensate was $\sim 5\,ps$. The spatial coherence is expected to decay corresponding to this characteristic time, when the delay between the interferometer arms is increased starting from zero. To qualita-

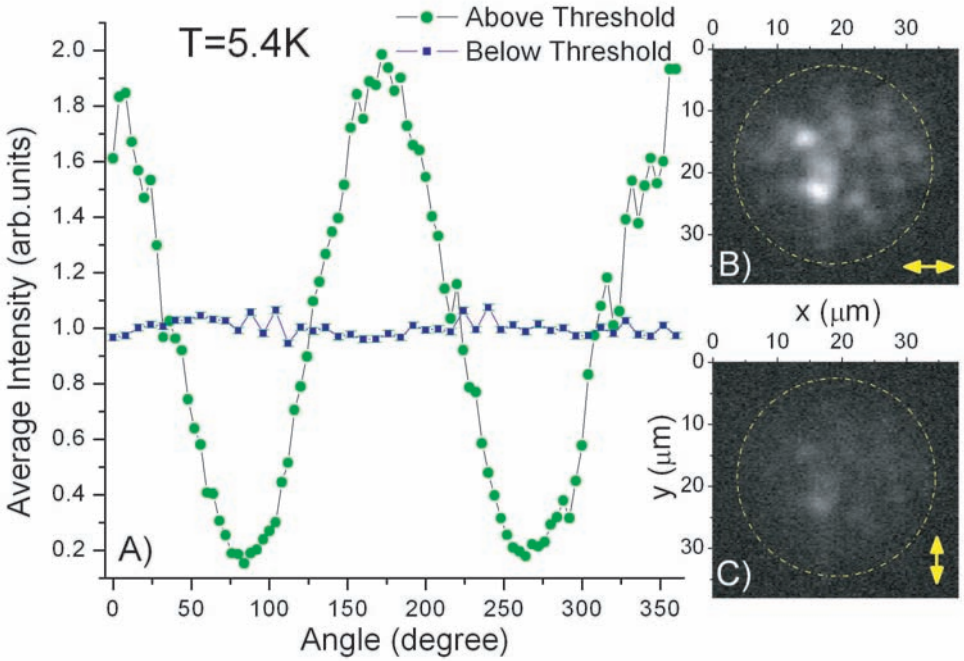


**Figure 5.19:** Polarisation of the polariton emission. On panel A the intensity of the polariton emission is depicted versus the orientation of a linear polariser. Below threshold no oscillations are observed whereas above threshold, the oscillations correspond to a linear polarisation degree of 80%. On the images, the emission pattern of the spot above threshold is shown parallel to the signal polarisation (panel B) and normal to its polarisation (panel C). The data is a courtesy of Jacek Kasprzak of the University of Grenoble.

tively explore this effect, images of the two superimposed spots are taken at a delay between 0 and 10 $ps$. The images are depicted in fig. 5.18. The planar mirror in figure 5.14 is tilted in order to slightly misalign the direction of the beam coming from each interferometer arm. This generates spatial fringes in the image and allows an evaluation of the contrast from a single image. On the image for $\tau = 0\,ps$ a very high fringe contrast is observed in the centre of the spot. The contrast of the fringes is not uniform over the spot (see fig. 5.17) and some regions (four points around the centre) show a locally higher contrast (see fig. 5.18). When the delay is increased, the fringe contrast diminishes $(2, 4, 6\,ps)$ and almost disappears at $\tau = 20\,ps$.

## 5.6 Polarisation of the condensate

The polarisation of the emission from the sample was analysed by a linear polariser. The measurement is displayed in fig. 5.19. The intensity of the emission is plotted versus the angle of the polariser. Below threshold, the emission is completely unpolarised. Above threshold, the intensity oscillates when the polariser orientation angle is scanned.

From the contrast of the oscillations, a polarisation degree of 80 % is deduced. Image B shows the emission spot when the polariser is set to the direction of the polarisation of the signal emission. Several bright emission spots as in fig. 5.3 and 5.9 are observed. In the perpendicular direction, the signal is much weaker (image C). The pattern of the spots seems to be similar to the one in image B. The direction of the polarisation is in the direction of one of the crystal symmetry axes. A dependence of the signal polarisation direction on the laser polarisation direction can be excluded, as the polarisation direction of the emission does not change when the input laser polarisation direction is changed.

## 5.7 Second order coherence of the condensate

As discussed in section 5.3.3 a polariton condensate is characterised by a coherent state, whereas the emission below threshold should have a thermal character. In the Grenoble group, a Hanburry-Brown-Twiss type measurement was performed on the emission from the polaritons. In doing this, the emission is split by a beamsplitter and sent to two single photon detectors. The temporal coincidences are measured and the second order coherence function $g^{(2)}(\tau)$ is measured. Below threshold, a bunching of the order of a few percent is observed[5], whereas above threshold $g^{(2)}(\tau)$ is completely flat demonstrating no quantum correlation as expected for a coherent state. This measurement is a further feature supporting the evidence of the observation of a condensate.

There is a situation known from the theory of Bose-Einstein condensation, where several states are coherently macroscopically populated at the same time. This is known as fragmentation of the condensate (see chapter 15 in [70]). In principle this effect can be excluded, since the interaction potential of the polaritons is positive and thus prevents from a fragmentation [70, 92]. Nevertheless, it would be interesting to check whether the system is in a single-mode coherent state or a multimode coherent state, which would correspond to a fragmentation of the condensate. To do this, the spatial second order coherence $g^{(2)}(r, r', 0)$ would need to be investigated. Such an experimental study has been done for the signal emission in polariton parametric scattering [7] and the same experimental technique could be employed here.

## 5.8 A Bose-Einstein Condensate in a solid state system

We have presented a set of experiments investigating the coherence properties of the emission arising from a non-linear incoherent relaxation mechanism of polaritons in CdTe microcavities. When the threshold for the non-linear relaxation is passed, a spatial correlation spanning over several times the thermal wavelength of non-condensed polaritons at low temperature is observed. This appearance of long-range order is a manifestation of the appearance of a macroscopic wavefunction for the condensed polaritons. A macroscopic wavefunction acts as an order parameter of a condensate and is the most important fundamental property of Bose-Einstein condensation. Since the

[5]The value of the bunching is pretty low since the time-resolution of the detectors is $\sim 100\,ps$, which is about 50 times longer than the coherence time of the emission.

claim of the existence of Bose-Einstein condensation in excitonic systems [11], various works have claimed its actual observation, concentrating on the spectral distribution of exciton photoluminescence. A few years ago, some papers attracted a quite considerable attention [22, 21, 104] reporting a particular spatial distribution of the photoluminescence emission from quantum well excitons. In reference [21], Bose-Einstein condensation was claimed, however up to now, the appearance of long-range order has not been shown in the investigated system. At the same time, Deng *et al.* claimed the observation of Bose-Einstein condensation in a polariton system based on the measurement of the temporal second-order coherence function. The measurement of the spatial long-range order was bypassed. The claimed transition from a thermal to a coherent state was not clearly demonstrated. We have presented for the first time the observation of long-range order in the framework of Bose-Einstein condensation in a solid state system.

In conclusion, the experiments performed in Grenoble in the Le Si Dang group and in our group in Lausanne have presented the following experimental findings:

- **Bose-Einstein statistics of the polaritons:** The energy distribution of the polariton emission shows a Bose-Einstein distribution shape when the threshold for the non-linear polariton relaxation is approached. Above threshold, the distribution features a Bose-Einstein distribution and displays a sharp peak at $E = 0$ corresponding to a macroscopic population of the lowest energy state.

- **Polarisation build-up of the polaritons independent from the laser polarisation:** The emission of the polaritons is unpolarised below threshold whereas above threshold a linear polarisation of 80% is observed. This polarisation does not change when the polarisation of the exciting laser beam is changed, showing that the phase coherence of the laser is lost by the incoherent relaxation of the polaritons. This implies that the coherence of the polaritons at $k = 0$ is a spontaneous coherence.

- **Build-up of long-range order in the polariton emission:** A spatial correlation spanning several times the thermal wavelength of non-condensed polaritons at low temperature is observed above threshold. This is the most pertinent feature for the appearance of Bose-Einstein condensation of excitons. The build-up of the long-range order indicates the build-up of the order parameter of the condensate.

- **Transition from a thermal to a coherent state for the polaritons:** Below threshold the emission of the polaritons is bunched, since the system is in a thermal state. When the threshold is passed, the correlation vanishes showing that the system is characterised by a thermal state.

Based on all these experimental observations, we can conclude, that we have demonstrated Bose-Einstein condensation of microcavity polaritons. After 40 years of intense research this is the first irrefutable observation of Bose-Einstein condensation in a solid state system.

# Chapter 6

# Conclusion and Outlook

The thesis presents an experimental analysis of the coherence and dynamics properties of polariton non-linearities in semiconductor microcavities. A number of different experimental techniques essentially pump-probe (including coherent control), but also resonant and non-resonant photoluminescence have been performed. To investigate the emission of the cavity, time-integrated as well as time-resolved spectrally, spatially, and angularly resolved detection has been employed. This required the use of photomultiplier tubes, CCD and streak cameras and frequency upconversion techniques as well as spatial and temporal interferometry. The main results can be summarised as follows:

- In chapter 3, we investigated the dynamics of coherent polaritons during a stimulated parametric scattering experiment in a GaAs microcavity. Essentially pump-double-probe (i.e. coherent control) techniques have been employed, for the detection we used CCD cameras in time-integration. We found that parametric scattering can be well controlled by judiciously phase-locked probe pulses. Just above threshold, the signal emission can be regarded as a superposition of coherently interfering processes of the respective probe pulses. For delays of the second probe pulse as long as $10\,ps$ interference contrasts of more than $75\,\%$ were observed, confirming that polaritons have long dephasing times. Far above threshold a depletion of the pump polariton mode is observed, a feature which is well reproduced by numerical simulations using the model of the polariton parametric amplifier proposed by Ciuti *et al.* [29]. In an angle resolved intensity measurement we showed, that the emission of signal and idler is correlated, i.e. the signal and idler oscillations are in phase and when the coherent control maximises the emission in the probe direction, the idler also is maximized.

- In chapter 4 the real-time dynamics of the polariton parametric scattering process in the stimulated and spontaneous regimes were investigated. As shown in chapter 3, the pump mode is strongly depleted by the parametric scattering far above threshold. This depletion acts on the temporal shape of the scattering and shifts the emission maximum to earlier delays. In the upconversion measurements it was shown, that the rise of the signal emission is considerably delayed with respect to the pump and probe excitations. This was attributed to the changes

of the polariton dispersion during the experiments employing high pump densities. The shape of the dispersion changes in time which leads to a very complex phase-matching for the process, probably explaining the delayed rise of the signal emission. In the spontaneous regime, we showed, that the parametric scattering is initially started by polaritons which have relaxed to the band bottom by the phonon emission.

- In chapter 5 the coherence properties of the non-linear emission occurring close to zero in-plane wavevector in CdTe microcavities under non-resonant excitation were investigated. The energy distribution of the polaritons emitted from the cavity is thermalised below threshold. The emission above threshold is highly polarised and the orientation of the polarisation does not depend on the polarisation direction of the exciting laser beam. A spatial coherence largely exceeding the thermal correlation length of the polaritons was shown to build up above threshold. At the threshold the system passes from a thermal state into a coherent state characterised by the wavefunction of the polariton condensate. The sum of all these experimental observations enables us to conclude that the Bose-Einstein condensation of polaritons has been observed. We regard these observations as the first bullet-proof evidence for spontaneous Bose-Einstein condensation in a solid state system, a phenomenon that has been the subject to many investigations and controversies during the past four decades.

The experiments presented show that it is possible to achieve a quantum degenerate occupation of polariton states, which can interact in a reasonably efficient way. In the framework of polariton parametric scattering this quantum degeneracy is directly induced by the exciting laser beam, whereas in the case of Bose-Einstein condensation it builds up spontaneously.

The performed series of experiments could be extended and complemented as follows:

- The coherent control experiment has been performed applying two probe pulses to the signal state. In the modelling in chapter 4 a coherent control effect was observed when one probe is applied to the signal and another one to the idler state. It would be interesting to realise this situation in the experiment, although this is very complex.

- Below threshold the spontaneous parametric scattering mechanism is supposed to produce polarisation entangled signal idler pairs. This important property could be probed doing polarisation resolved coincidence or noise measurements.

- Some excitation parameters in the experiments on the real-time dynamics were not completely controlled. Especially the spot shape and the superposition of pump and probe spots should be monitored and eventually recorded. The data on the spatial intensity distribution could be used as an input for a theoretical model accounting for finite size and inhomogeneous excitation and emission spots.

- The long-range order of a polariton condensate has been shown. The polariton condensate is inhomogeneous and a more detailed mapping of the first order spatial coherence function normalised by the spatial intensity distribution could give information about the condensate fraction distribution over the emission zone.

- The Bose-Einstein polariton condensate is supposed to be in a single coherent state. This feature could be checked by performing spatially resolved measurements of the second order coherence in the emission zone.

Polariton parametric scattering could be exploited in real world applications as ultrafast amplification devices or compact sources for entangled photons. This appears especially interesting, as there is a need to further push up the speed of telecommunication networks and to use quantum cryptography for the secure transmission of data. The main technological challenge for this research direction would be to make microcavities that work at room-temperature. As discussed in [93], the maximum operation temperature is dependent on the exciton binding energy which in turn depends on the respective employed material system. Promising candidates for this attempt are ZnSe or GaN based microcavities or cavities with an organic active material with first samples featuring the strong coupling regime [84, 71, 49, 112].

A second more fundamental promising direction would be the investigation of quantum phenomena in polariton systems. In the past polariton microstructures with one-dimensional and zero-dimensional photonic confinement have been demonstrated. The photonic mode confined by the boundary of the dielectric mirrors in the growth direction is further confined in the in-plane resonator direction by etching away the top Bragg mirror and the cavity [35]. This gives rise to one- and zero-dimensional polariton modes and parametric scattering involving different confined modes has been demonstrated [36, 37, 34]. In a recent work, El Daïf and co-workers have employed a different approach [45]: the thickness of the cavity is locally modified by etching a mesa of a few nm depth before growing the top Bragg reflector. The advantage of this method is that the interaction of two dimensional polaritons with zero-dimensional or one dimensional confined polariton modes can be studied. The lateral structure of the confinement zones can be defined on demand using photo-lithography and the realisation of "polaritonic circuits" is imaginable. Using such circuits, the study of a polariton Josephson effect or polariton superfluidity could be possible. The effect of Bose-Einstein condensation in CdTe microcavities seems to be influenced by the local disorder in the sample. Using the technique described in [45], one could introduce defects in the in-plane cavity structure on demand and study the effects of an eventual polariton Bose-Einstein condensation in such structures.

# Appendix A

# Stabilised Michelson Interferometer

For the measurements in chapter 3 and 5 a stabilised Michelson interferometer was used. The employed interferometer stabilisation setup was first proposed by Wehner, Ulm and Wegener [115].

The stabilisation setup is depicted in figure A.1. The input signal beam is split into the two interferometer arms by a non-polarizing beam-splitter BS2.The two beams are reflected by two plane mirrors M2 and M3. They are recombined in the beam-splitter and sent to the output of the interferometer. Changing the position of a mirror along the beam direction varies the optical path between the two interferometer arms and thus the time delay and relative phase between the two split input signals changes.

One of the two mirrors is attached to a piezo actuator which is mounted on a translational stage. The translational stage can be used to vary the relative delay of the two interferometer arms to up to several hundred picoseconds. The piezo actuator can be used to actively stabilise the relative phase of the two interferometer arms and also allows a variation of the optical path of about $6\mu m$ or 40 fs ($\sim$ 15 times the polariton wavelength). The active stabilization is provided by monitoring the intensity fringes of a He-Ne laser beam which passes the Michelson interferometer on a second plane which is parallel to the one of the signal beam [115]. The He-Ne beam which has linear p-polarization is reflected twice once by the mirror $M0$ and once $M1$ this allows the control the position and the direction of the beam. Before entering the interferometer the beam passes a polariser in order to extinct any polarisation deviation induced by the reflection on the metallic mirrors $M0$ and $M1$. The beam is split and recombined by BS2 after having passed through the two interferometer arms. In the arm of mirror $M2$, the incident p-polarization is turned by 90° into s-polarisation by passing twice through a $\lambda/4$-waveplate. Thus the $M2$-arm beam has s-polarization and the $M3$-arm beam p-polarisation at the output of the interferometer. The two perpendicularly polarised beams are transformed into left and right circularly polarized light by the second $\lambda/4$-waveplate. If the beams are of the same intensity, the beams superimpose to form linearly polarized light. Putting a polarizer after the waveplate allows one to probe the delay between the two pulses since the angle of polarisation depends on the

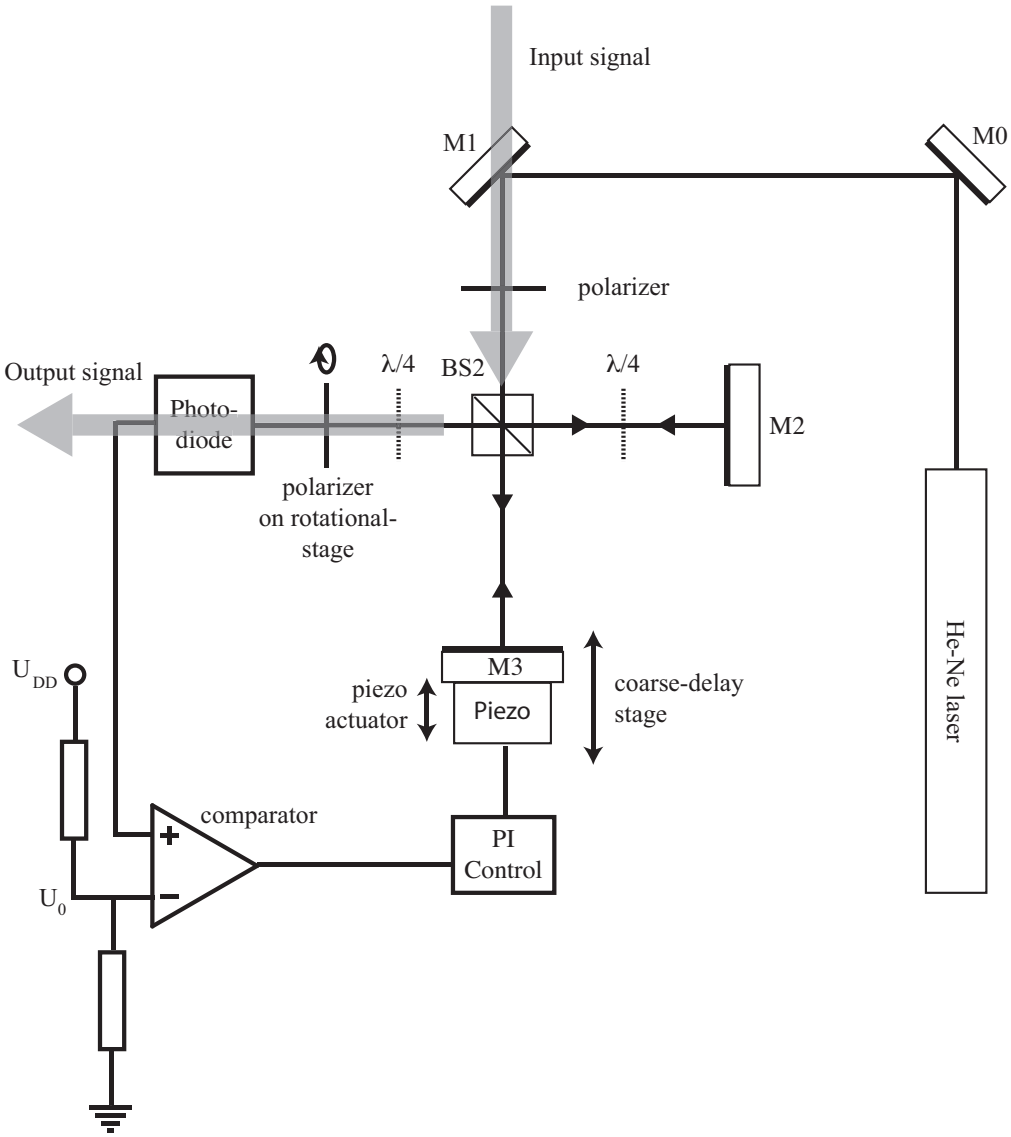


**Figure A.1:** Setup of the stabilized interferometer.

difference in the optical paths. The intensity after the polarizer varies according to

$$I = 2I_0 \cos^2(\delta/2 - \phi + \pi/4) \tag{A.1}$$

where $\delta$ is the path difference of the two arms in terms of relative phase and $\phi$ is the polarizer angle. Some remaining circular polarization stays constant for different polarizer angles. Since we can measure the path difference by the intensity $I$ and change it by the piezo voltage it is possible to stabilize the relative phase difference with a feedback-loop. A photodiode and a preamplifier transform the intensity $I$ into a Voltage $U$. A constant voltage reference $U_0$ corresponding to the intensity $I_0$ is

subtracted by a comparator. The signal coming out of the comparator is zero when the incident light-intensity on the photodiode is $I_0$ thus at the inflection point of the $cos^2$-function. If the optical path of the $M3$-arm is more than desired we get a positive signal at the output of the comparator and vice versa. This allows a proportional-integral-control to drive the piezo actuator and to stabilise the optical path difference in a very efficient manner.

Turning the polarizer angle $\phi$ results in changing the set point of the stabilisation (see equation A.1) and thus varies the optical path difference on a nanometer-scale. A rotation of the polarizer angle of $2\pi$ changes the phase between the arms by $4\pi_{He-Ne}$ which corresponds to 1265.6 nm (twice the He-Ne laser wavelength) or a time delay of $4fs$.

An estimation of the interferometer stability can be made by measuring the intensity detected by the photodiode with and without active stabilization. The deviations of the reference intensity $I_0$ after the comaparator is just:

$$I = I_0(2\cos^2(\delta/2 - \phi + \pi/4) - 1) \tag{A.2}$$

Without stabilization the fluctuations of the detected intensity are $\Delta I = 2I_0$. When the stabilization is turned on the fluctuations diminish down to $\Delta I \leq 0.03 \cdot 2I_0$. Approximating equation A.2 by a sawtooth function we can assume that a variation of $\Delta I = 2I_0$ corresponds to a fluctuation amplitude of 316.4 nm. In the stabilized case the optical path fluctuations are thus three percent of 316.4 nm which is $\sim 10nm$. For the polariton wavelength of $\sim 800nm$ we obtain a relative phase stability of $\pi/40$. The setup has a good performance, since the phase between the two pulses can continuously be scanned over $30\pi$, whilst maintaining a phase stability of $\sim \pi/40$.

# Acknowledgements

My PHD has been a very rich experience for me. Many people have contributed to this work giving their advice, guiding through the jungle of ideas for new experiments or even participating in the numerous measuring sessions lasting until daybreak.

First of all, I would like to thank my thesis adviser Jean-Louis Staehli. He let me a lot of liberty in the laboratory work and was always available for profound and critical physics discussions and lots of suggestions. Benoît Deveaud closely followed my work and gave important impulsions for new research ideas. Especially his enthusiasm for my research results was an important source of motivation for me.

I started to work in the laboratory with Michele Saba, who passed me his experimental know-how of ultra-fast spectroscopy. During one year I worked together with Thierry Guillet and we tried to find the shortest time transients of the polariton scattering. Maxime Richard came to Lausanne for two intense measuring sessions. Augustin Baas brought many new ideas for experiments especially about the quantum optics aspects of the polariton system. Pierre Jeambrun, last come, enriched our team with his enthusiasm for polariton physics. The last chapter of my PHD would never have been possible without Augustin, Maxime, and Pierre and we put all our know-how together to obtain the results during weeks of intense night shifts. I had a lot of support for theoretical aspects by Vincenzo Savona, Cristiano Ciuti, Davide Sarchi, Paolo Schwendimann, and Antonio Quattropani. I thank Jacek Kasprzak for making me available unpublished measurements. Romuald Houdré, Ross Stanley, and Ursula Oesterle in the group of Marc Ilegems developed the sample for the polariton parametric scattering studies. Régis André and Le Si Dang did the pioneering work to obtain high quality CdTe microcavity samples at the University of Grenoble. Andrea Dunbar revised the manuscript with great patience and made me find the numerous "Germanisms" and "Frenchisms".

I am grateful to Roger Rochat, Nicolas Leiser, and Alessandro Ichino from the mechanics and electronics workshops. Many thanks to our secretaries Claire-Lyse Rouiller, Aline Gruaz, Corine Chiquet, and Suada Hasanovic.

A lot of persons gave me advice and support during these four years with their ups and downs. I am especially grateful to Blandine Alloing, Jean Berney, Christian Blumer, Raphaël Butté, Iacopo Carusotto, Andrea Crottini, Ounsi El Daïf, Gregor Dasbach, Andrea Feltrin, Rolando Ferrini, Jean-Daniel Ganière, Nicolas Grandjean, Gary Hayes, Reda Idrissi, Lars Kappei, André Kuntz, Pierre Lugan, Alexander Markus, Daniel Marti, Michele Merano, Pablo Moreno, François Morier-Genoud, Tim Otterburg, Gaetano Parascandolo, Martia Portella-Oberli, Philipp Ridha, Marco Rossetti,

Lorenzo Sirigu, Samuel Sonderegger, Jacek Szczytko, Carl Zinoni, and any person I have unintentionally forgotten.

I am honored that Manfred Bayer, Attaç Imamoglu, Vincenzo Savona, and Robert Schaller agreed to judge my thesis.

Finally I would like to thank my parents and all my family for their constant support and my friends here in Switzerland and in Germany.

# Curriculum vitæ

**Stefan KUNDERMANN**

Physicist

Institute of Quantum Electronics and Photonics
Swiss Federal Institute of Technology - EPFL
CH-1015 Lausanne, Switzerland

stefan.kundermann@epfl.ch
tel. + 41 21 693 6008
fax + 41 21 693 5480

## Education

- **2002-2006 Ph.D. Thesis**
  "Coherence Properties of Microcavity Polaritons:
  from Parametric Scattering to Bose-Einstein Condensation",
  supervisor Dr. J.-L. Staehli (EPFL).

- **2001-2006 Post-graduate training**:
  Euroconference on Quantum Optoelectronics for NanoTechnology (EQUONT) Les Houches, Centre de Physique, 21 - 26 April 2002.Course "Ultrafast Processes in Solid State Nanostructures"

  International School of Physics "Enrico Fermi", Varenna, Villa Monastero, 25 June - 5 July 2002. Course "Electron and Photon Confinement in Semiconductor Nanostructures" Directors: Prof. B. Deveaud-Plédran, Prof. A. Quattropani Varenna, Villa Monastero, 25 June - 5 July 2002.

  Euroconference on Quantum Optoelectronics for NanoTechnology (EQUONT) Cambridge-England, Clare College, 19 - 23 Septembre 2004.
  Course "Quantum technology and optical processes in semiconductor nanostructures"

  Physics of nanostructures (EPFL)

- **2002 Diploma Degree in Physics**, Darmstadt University of Technology, Germany.
  Diploma thesis: "Coherent Control of Polariton Dynamics in Semiconductor Microcavities", supervisors Dr. J.-L. Staehli (EPFL) and Prof. W. Elsässer (Darmstadt University of Technology).

# Conferences

- OECS7, Montpellier, France (as a participant)
- Euroconference on Quantum Optoelectronics for NanoTechnology (EQUONT) Les Houches, Centre de Physique, 21 - 26 April 2002. Course "Ultrafast Processes in Solid State Nanostructures" (oral): "Coherent control of parametric amplification in semiconductor microcavities" S. Kundermann, M. Saba, C. Ciuti, JL. Staehli and B. Deveaud
- CLEO-QUELS 2002, May 19-24 2002, Long Beach, CA, USA (oral): "Coherent Control of parametric amplification in semiconductor microcavities" S. Kundermann, M. Saba, C. Ciuti, J. L. Staehli, B. Deveaud
- International School of Physics "Enrico Fermi", Varenna, Villa Monastero, 25 June - 5 July 2002. Course "Electron and Photon Confinement in Semiconductor Nanostructures" Directors: Prof. B. Deveaud-Pldran, Prof. A. Quattropani Varenna, Villa Monastero, 25 June - 5 July 2002.
- ISCS 2002, october 7 - 10 2002, Lausanne, Switzerland (poster): "Coherent optical control of parametric gain in semiconductor microcavities" S. Kundermann, M. Saba, J. L. Staehli, B. Deveaud
- NOEKS7 2003, 24-28 February 2003, Karlsruhe, Germany (oral): "Coherent control of parametric amplification in semiconductor microcavities" S. Kundermann, M. Saba, C. Ciuti, JL. Staehli and B. Deveaud
- IV GIORNATA INTERNAZIONALE DI SCIENZA DEI MATERIALI, 30 Maggio 2003 Cittadella Universitaria Monserrato-Cagliari (invited): "Controllo coerente della diffusione parametrica nelle microcavit semiconduttrici: nuovi dispositivi per le telecomunicazioni?" S. Kundermann
- OECS 8, 15-17 September , 2003 Lecce, Italy (invited): "Coherence properties of polaritons in semiconductor microcavities" S. Kundermann , T. Guillet, M. Saba, C. Ciuti, O. El Daif, JL. Staehli, and B. Deveaud
- Annual meeting of the SPS 2004, March 3-4, Neuchatel, Switzerland (invited): "Evidence for parametric memory and correlation in semiconductor microcavities" S. Kundermann, T. Guillet, M. Saba, C. Ciuti, J. L. Staehli, and B. Deveaud

- International conference on spontaneous coherence in excitonic systems, May 24-28 2004, Seven Springs Mountain Resort, Pennsylvania USA (oral): "Evidence for correlation and parametric memory in semiconductor microcavities" S. Kundermann, M.Saba, C. Ciuti, T. Guillet, J. L. Staehli, and B. Deveaud

- NCCR QP General assembly Chaumont, 5 - 6 July 2004, (invited): "Dynamics of the polariton parametric amplifier" S. Kundermann, C. Ciuti, O. El Daif, R. Idrissi, A. Baas, JL. Staehli, and B. Deveaud

- Euroconference on Quantum Optoelectronics for NanoTechnology (EQUONT) Cambridge-England, Clare College, 19 - 23 Septembre 2004. Course "Quantum technology and optical processes in semiconductor nanostructures" (oral): "Dynamics of the microcavity polariton parametric amplifier" S. Kundermann, C. Ciuti, T. Guillet, JL. Staehli, and B. Deveaud

- OECS 9 - ICSCE 2, 5-10 September, 2005 Southampton, England (oral): "Phase coherent effects of polariton parametric scattering in the time domain" S. Kundermann, A. Baas, JL. Staehli, and B. Deveaud

# Selected Publications


- M. Saba, C. Ciuti, J. Bloch, V. Thierry-Mieg, R. Andre, L. S. Dang, S. Kundermann, A. Mura, G. Bongiovanni, J. L. Staehli, and B. Deveaud, High-temperature ultrafast polariton parametric amplification in semiconductor microcavities, Nature **414** (2001), no. 6865, 731.

- M. Saba, C. Ciuti, S. Kundermann, J. L. Staehli, B. Deveaud, J. Bloch, V. Thierry-Mieg, R. Andre, L. S. Dang, G. Bongiovanni, and A. Mura, Towards a room temperature polariton amplifier, Physica Status Solidi A-Applied Research **190** (2002), no. 2, 315.

- J. L. Staehli, M. Saba, S. Kundermann, C. Ciuti, and B. Deveaud, Quantum kinetics of parametric polariton scattering in microcavities, Physica Status Solidi B-Basic Research **234** (2002), no. 1, 183.

- S. Kundermann, M. Saba, C. Ciuti, T. Guillet, U. Oesterle, J. L. Staehli, and B. Deveaud, Coherent control of polariton parametric scattering in semiconductor microcavities, Physical Review Letters **91** (2003), no. 10, 107402.

- M. Saba, C. Ciuti, S. Kundermann, J. L. Staehli, and B. Deveaud, Towards a room-temperature polariton amplifier, Semiconductor Science And Technology **18** (2003), no. 10, S325.

- S. Kundermann, T. Guillet, M. Saba, C. Ciuti, O. El Daif, J. L. Staehli, and B. Deveaud, Coherence properties of polaritons in semiconductor microcavities, Physica Status Solidi A-Applied Research **201** (2004), no. 3, 381.

- J. L. Staehli, S. Kundermann, M. Saba, C. Ciuti, A. Baas, T. Guillet, and B. Deveaud, Non-linear dynamical effects in semiconductor microcavities, Physica Status Solidi B-Basic Solid State Physics **242** (2005), no. 11, 2246.

# Bibliography


[1] J. F. Allen and A. D. Misener, Nature **141** (1938), 75.

[2] M. H. Anderson, J. R. Ensher, M. R. Matthews, C. E. Wieman, and E. A. Cornell, *Observation of bose-einstein condensation in a dilute atomic vapor*, Science **269** (1995), no. 5221, 198–201.

[3] R. Andre and L. S. Dang, *Low-temperature refractive indices of $Cd_{1-x}Mn_xTe$ and $Cd_{1-y}Mg_yTe$*, Journal Of Applied Physics **82** (1997), no. 10, 5086–5089.

[4] F. T. Arecchi, E. Gatti, and A. Sona, *Time distribution of photons from coherent and gaussian sources*, Physics Letters **20** (1966), no. 1, 27–29.

[5] G. Arisholm, G. Rustad, and K. Stenersen, *Importance of pump-beam group velocity for backconversion in optical parametric oscillators*, Journal Of The Optical Society Of America B-Optical Physics **18** (2001), no. 12, 1882–1890.

[6] A. Assion, T. Baumert, M. Bergt, T. Brixner, B. Kiefer, V. Seyfried, M. Strehle, and G. Gerber, *Control of chemical reactions by feedback-optimized phase-shaped femtosecond laser pulses*, Science **282** (1998), no. 5390, 919–922.

[7] A. Baas, J. P. Karr, M. Romanelli, A. Bramati, and E. Giacobino, *Quantum degeneracy of microcavity polaritons*, Physical Review Letters **96** (2006), no. 17, 176401.

[8] A. Baas, J. P. Karr, H. Eleuch, and E. Giacobino, *Optical bistability in semiconductor microcavities*, Physical Review A **69** (2004), no. 2, 023809.

[9] A. Baas, J. P. Karr, M. Romanelli, A. Bramati, and E. Giacobino, *Optical bistability in semiconductor microcavities in the nondegenerate parametric oscillation regime: Analogy with the optical parametric oscillator*, Physical Review B **70** (2004), no. 16, 161307, 161307.

[10] J. J. Baumberg, P. G. Savvidis, R. M. Stevenson, A. I. Tartakovskii, M. S. Skolnick, D. M. Whittaker, and J. S. Roberts, *Parametric oscillation in a vertical microcavity: A polariton condensate or micro-optical parametric oscillation*, Physical Review B **62** (2000), no. 24, R16247–R16250.

[11] J. M. Blatt, W. Brandt, and K. W. Boer, *Bose-einstein condensation of excitons*, Physical Review **126** (1962), no. 5, 1691–1692.

[12] I. Bloch, T. W. Hansch, and T. Esslinger, *Measurement of the spatial coherence of a trapped bose gas at the phase transition*, Nature **403** (2000), no. 6766, 166–170.

[13] N. N. Bogoliubov, J. Phys. USSR **11** (1947), 23.

[14] N. H. Bonadeo, J. Erland, D. Gammon, D. Park, D. S. Katzer, and D. G. Steel, *Coherent optical control of the quantum state of a single quantum dot*, Science **282** (1998), no. 5393, 1473–1476.

[15] G. Bongiovanni, A. Mura, F. Quochi, S. Gurtler, J. L. Staehli, F. Tassone, R. P. Stanley, U. Oesterle, and R. Houdre, *Coherent exciton-photon dynamics in semiconductor microcavities: The influence of inhomogeneous broadening*, Physical Review B **55** (1997), no. 11, 7084–7090.

[16] M. Born and E. Wolf, *Principles of optics*, 7 ed., Cambridge University Press, Cambridge, 1985.

[17] S. N. Bose, *Plancks gesetz und lichtquantenhypothese*, Zeitschrift Für Physik **26** (1924), 178–181.

[18] Robert W. Boyd, *Nonlinear optics*, 2 ed., Academic Press, Boston, 2002.

[19] C. C. Bradley, C. A. Sackett, J. J. Tollett, and R. G. Hulet, *Evidence of bose-einstein condensation in an atomic gas with attractive interactions*, Physical Review Letters **75** (1995), no. 9, 1687–1690.

[20] R. D. Burnham, N. Holonyak, H. W. Korb, H. M. Macksey, D. R. Scifres, Woodhous.Jb, and Z. I. Alferov, *Double heterojunction AlGaAsP quaternary lasers*, Applied Physics Letters **19** (1971), no. 2, 25–28.

[21] L. V. Butov, A. C. Gossard, and D. S. Chemla, *Macroscopically ordered state in an exciton system*, Nature **418** (2002), no. 6899, 751–754.

[22] L. V. Butov, C. W. Lai, A. L. Ivanov, A. C. Gossard, and D. S. Chemla, *Towards bose-einstein condensation of excitons in potential traps*, Nature **417** (2002), no. 6884, 47–52.

[23] R. L. Byer and S. E. Harris, *Power and bandwidth of spontaneous parametric emission*, Physical Review **168** (1968), no. 3, 1064–1068.

[24] H. Cao, S. Pau, J. M. Jacobson, G. Bjork, Y. Yamamoto, and A. Imamoglu, *Transition from a microcavity exciton polariton to a photon laser*, Physical Review A **55** (1997), no. 6, 4632–4635.

[25] I. Carusotto and C. Ciuti, *Spontaneous microcavity-polariton coherence across the parametric threshold: Quantum monte carlo studies*, Physical Review B **72** (2005), no. 12, 125335.

[26] D. S. Chemla and J. Shah, *Many-body and correlation effects in semiconductors*, Nature **411** (2001), no. 6837, 549–557.

[27] S. Chu, L. Hollberg, J. E. Bjorkholm, A. Cable, and A. Ashkin, *3-dimensional viscous confinement and cooling of atoms by resonance radiation pressure*, Physical Review Letters **55** (1985), no. 1, 48–51.

[28] J. I. Cirac, R. Blatt, P. Zoller, and W. D. Phillips, *Laser cooling of trapped ions in a standing wave*, Physical Review A **46** (1992), no. 5, 2668–2681.

[29] C. Ciuti, P. Schwendimann, B. Deveaud, and A. Quattropani, *Theory of the angle-resonant polariton amplifier*, Physical Review B **62** (2000), no. 8, R4825–R4828.

[30] C. Ciuti, P. Schwendimann, and A. Quattropani, *Parametric luminescence of microcavity polaritons*, Physical Review B **63** (2001), 041303.

[31] C. Ciuti, P. Schwendimann, and A. Quattropani, *Theory of polariton parametric interactions in semiconductor microcavities*, Semiconductor Science And Technology **18** (2003), no. 10, S279–S293.

[32] W. Czaja and Schwerdt.Cf, *Evidence for bose-einstein condensation of free excitons in AgBr*, Solid State Communications **15** (1974), no. 1, 87–91.

[33] L. S. Dang, D. Heger, R. Andre, F. Boeuf, and R. Romestain, *Stimulation of polariton photoluminescence in semiconductor microcavity*, Physical Review Letters **81** (1998), no. 18, 3920–3923.

[34] G. Dasbach, C. Diederichs, J. Tignon, C. Ciuti, P. Roussignol, C. Delalande, M. Bayer, and A. Forchel, *Polarization inversion via parametric scattering in quasi-one-dimensional microcavities*, Physical Review B **71** (2005), no. 16, 161308.

[35] G. Dasbach, A. A. Dremin, M. Bayer, V. D. Kulakovskii, N. A. Gippius, and A. Forchel, *Oscillations in the differential transmission of a semiconductor microcavity with reduced symmetry*, Physical Review B **65** (2002), no. 24, 245316.

[36] G. Dasbach, M. Schwab, M. Bayer, and A. Forchel, *Parametric polariton scattering in microresonators with three-dimensional optical confinement*, Physical Review B **6420** (2001), no. 20, 201309.

[37] G. Dasbach, M. Schwab, M. Bayer, D. N. Krizhanovskii, and A. Forchel, *Tailoring the polariton dispersion by optical confinement: Access to a manifold of elastic polariton pair scattering channels*, Physical Review B **66** (2002), no. 20, 201201.

[38] K. B. Davis, M. O. Mewes, M. R. Andrews, N. J. Vandruten, D. S. Durfee, D. M. Kurn, and W. Ketterle, *Bose-einstein condensation in a gas of sodium atoms*, Physical Review Letters **75** (1995), no. 22, 3969–3973.

[39] H. Deng, G. Weihs, C. Santori, J. Bloch, and Y. Yamamoto, *Condensation of semiconductor microcavity exciton polaritons*, Science **298** (2002), no. 5591, 199–202.

[40] F. P. Dos Santos, J. Leonard, J. M. Wang, C. J. Barrelet, F. Perales, E. Rasel, C. S. Unnikrishnan, M. Leduc, and C. Cohen-Tannoudji, *Bose-einstein condensation of metastable helium*, Physical Review Letters **86** (2001), no. 16, 3459–3462.

[41] L. A. Dunbar, R. P. Stanley, M. Lynch, J. Hegarty, U. Oesterle, R. Houdre, and M. Ilegems, *Excitation-induced coherence in a semiconductor microcavity*, Physical Review B **66** (2002), no. 19, 195307.

[42] R. D. Dupuis and P. D. Dapkus, *Room-temperature operation of* $Ga_{(1-x)}Al_xAs - GaAs$ *double-heterostructure lasers grown by metalorganic chemical vapor-deposition*, Applied Physics Letters **31** (1977), no. 7, 466–468.

[43] A. Einstein, *Quantentheorie des einatomigen idealen gases*, Sitz. Ber. Preuss. Akad. Wiss. (Berlin) **22** (1924), 261.

[44] J. P. Eisenstein and A. H. MacDonald, *Bose-einstein condensation of excitons in bilayer electron systems*, Nature **432** (2004), no. 7018, 691–694.

[45] O. El Daïf, A. Baas, T. Guillet, J. P. Brantut, R. Idrissi Kaitouni, J. L. Staehli, F. Morier-Genoud, and B. Deveaud, *Polariton quantum boxes in semiconductor microcavities*, Applied Physics Letters **88** (2006), no. 6, 061105.

[46] J. Erland, V. Mizeikis, W. Langbein, J. R. Jensen, and J. M. Hvam, *Stimulated secondary emission from semiconductor microcavities*, Physical Review Letters **86** (2001), no. 25, 5791–5794.

[47] E. Fortin, S. Fafard, and A. Mysyrowicz, *Exciton transport in* $Cu_2O$ *- evidence for excitonic superfluidity*, Physical Review Letters **70** (1993), no. 25, 3951–3954.

[48] D. G. Fried, T. C. Killian, L. Willmann, D. Landhuis, S. C. Moss, D. Kleppner, and T. J. Greytak, *Bose-einstein condensation of atomic hydrogen*, Physical Review Letters **81** (1998), no. 18, 3811–3814.

[49] T. Fujita, Y. Sato, T. Kuitani, and T. Ishihara, *Tunable polariton absorption of distributed feedback microcavities at room temperature*, Physical Review B **57** (1998), no. 19, 12428–12434.

[50] R. N. Hall, R. O. Carlson, T. J. Soltys, G. E. Fenner, and J. D. Kingsley, *Coherent light emission from GaAs junctions*, Physical Review Letters **9** (1962), no. 9, 366–369.

[51] S. E. Harris, M. K. Oshman, and R. L. Byer, *Observation of tunable optical parametric fluorescence*, Physical Review Letters **18** (1967), no. 18, 732–734.

[52] M. Hasuo, N. Nagasawa, T. Itoh, and A. Mysyrowicz, *Progress in the bose-einstein condensation of biexcitons in CuCl*, Physical Review Letters **70** (1993), no. 9, 1303–1306.

[53] H. Haug and S. W. Koch, *Quantum theory of the optical and electronic properties of semiconductors*, World Scientific Publishing Company, Singapore, 1997.

[54] I. Hayashi, M. B. Panish, P. W. Foy, and S. Sumski, *Junction lasers which operate continuously at room temperature*, Applied Physics Letters **17** (1970), no. 3, 109-111.

[55] A. P. Heberle, J. J. Baumberg, and K. Kohler, *Ultrafast coherent control and destruction of excitons in quantum-wells*, Physical Review Letters **75** (1995), no. 13, 2598–2601.

[56] J. J. Hopfield, *Theory of the contribution of excitons to the complex dielectic constant of crystals*, Physical Review **112** (1958), no. 5, 1555–1567.

[57] R. Houdre, C. Weisbuch, R. P. Stanley, U. Oesterle, P. Pellandini, and M. Ilegems, *Measurement of cavity-polariton dispersion curve from angle-resolved photoluminescence experiments*, Physical Review Letters **73** (1994), no. 15, 2043–2046.

[58] D. Hulin, A. Mysyrowicz, and C. Benoitalaguillaume, *Evidence for bose-einstein statistics in an exciton gas*, Physical Review Letters **45** (1980), no. 24, 1970–1973.

[59] A. Huynh, J. Tignon, O. Larsson, P. Roussignol, C. Delalande, R. Andre, R. Romestain, and L. S. Dang, *Polariton parametric amplifier pump dynamics in the coherent regime*, Physical Review Letters **90** (2003), no. 10, 106401.

[60] A. Imamoglu, R. J. Ram, S. Pau, and Y. Yamamoto, *Nonequilibrium condensates and lasers without inversion: Exciton-polariton lasers*, Physical Review A **53** (1996), no. 6, 4250–4253.

[61] P. L. Kapitza, Nature **141** (1938), 913.

[62] L. V. Keldysh and A. N. Kozlov, *Collective properties of excitons in semiconductors*, Soviet Physics Jetp-Ussr **27** (1968), no. 3, 521.

[63] C. H. Kim, R. D. Li, and P. Kumar, *Deamplification response of a traveling-wave phase-sensitive optical parametric-amplifier*, Optics Letters **19** (1994), no. 2, 132–134.

[64] S. Kundermann, M. Saba, C. Ciuti, T. Guillet, U. Oesterle, J. L. Staehli, and B. Deveaud, *Coherent control of polariton parametric scattering in semiconductor microcavities*, Physical Review Letters **91** (2003), no. 10, 107402.

[65] P. G. Lagoudakis, M. D. Martin, J. J. Baumberg, A. Qarry, E. Cohen, and L. N. Pfeiffer, *Electron-polariton scattering in semiconductor microcavities*, Physical Review Letters **90** (2003), no. 20, 206401.

[66] L. D. Landau, J. Phys. USSR **5** (1941), 71.

[67] L. D. Landau and E. M. Lifshitz, Statisticheskai Fizika (1951).

[68] W. Langbein, *Spontaneous parametric scattering of microcavity polaritons in momentum space*, Physical Review B **70** (2004), no. 20, 205301.

[69] Y. S. Lee, T. B. Norris, A. Maslov, D. S. Citrin, J. Prineas, G. Khitrova, and H. M. Gibbs, *Large-signal coherent control of normal modes in quantum-well semiconductor microcavity*, Applied Physics Letters **78** (2001), no. 25, 3941–3943.

[70] S. Stringari and Lev P. Pitaevskii, *Bose-einstein condensation*, Oxford University Press, Oxford, New York, 2003.

[71] D. G. Lidzey, D. D. C. Bradley, M. S. Skolnick, T. Virgili, S. Walker, and D. M. Whittaker, *Strong exciton-photon coupling in an organic semiconductor microcavity*, Nature **395** (1998), no. 6697, 53–55.

[72] J. L. Lin and J. P. Wolfe, *Bose-einstein condensation of paraexcitons in stressed $Cu_2O$*, Physical Review Letters **71** (1993), no. 8, 1222–1225.

[73] F. London, Phys. Rev. **54** (1938), 947–954.

[74] G. Malpuech, A. Kavokin, A. Di Carlo, and J. J. Baumberg, *Polariton lasing by exciton-electron scattering in semiconductor microcavities*, Physical Review B **65** (2002), no. 15, 153310.

[75] L. Mandel and E. Wolf, *Coherence properties of optical fields*, Reviews Of Modern Physics **37** (1965), no. 2, 231–287.

[76] X. Marie, P. Renucci, S. Dubourg, T. Amand, P. Le Jeune, J. Barrau, J. Bloch, and R. Planel, *Coherent control of exciton polaritons in a semiconductor microcavity*, Physical Review B **59** (1999), no. 4, R2494–R2497.

[77] G. Messin, J. P. Karr, A. Baas, G. Khitrova, R. Houdre, R. P. Stanley, U. Oesterle, and E. Giacobino, *Parametric polariton amplification in semiconductor microcavities*, Physical Review Letters **87** (2001), no. 12, 127403.

[78] G. Modugno, G. Ferrari, G. Roati, R. J. Brecha, A. Simoni, and M. Inguscio, *Bose-einstein condensation of potassium atoms by sympathetic cooling*, Science **294** (2001), no. 5545, 1320–1322.

[79] S. A. Moskalenko, *Reversible optico-hydrodynamic phenomena in a nonideal exciton gas*, Soviet Physics-Solid State **4** (1962), no. 1, 199–204.

[80] M. Müller, *Etude de polariton en cavité en régime de forte excitation: dynamique et non-linéarités dans les microcavités II-VI*, Ph.D. thesis, Université Joseph Fourier, Grenoble, France, 2000.

[81] T. Ostreich and L. J. Sham, *Collective oscillations driven by correlation in the nonlinear optical regime*, Physical Review Letters **83** (1999), no. 17, 3510–3513.

[82] M. B. Panish, I. Hayashi, and S. Sumski, *Double-heterostructure injection lasers with room-temperature thresholds as low as 2300 a/cm2*, Applied Physics Letters **16** (1970), no. 8, 326-327.

[83] S. Pau, H. Cao, J. Jacobson, G. Bjork, Y. Yamamoto, and A. Imamoglu, *Observation of a laserlike transition in a microcavity exciton polariton system*, Physical Review A **54** (1996), no. 3, R1789–R1792.

[84] A. Pawlis, A. Kharchenko, O. Husberg, K. Lischka, and D. Schikora, *Preparation and properties of ZnSe/(Zn, Cd)Se multi-quantum-well microcavities for room temperature polariton emission*, Journal Of Physics-Condensed Matter **16** (2004), no. 35, S3689–S3694.

[85] O. Penrose, *On the quantum mechanics of helium.2*, Philosophical Magazine **42** (1951), no. 335, 1373–1377.

[86] O. Penrose and L. Onsager, *Bose-einstein condensation and liquid helium*, Physical Review **104** (1956), no. 3, 576–584.

[87] D. Porras, C. Ciuti, J. J. Baumberg, and C. Tejedor, *Polariton dynamics and bose-einstein condensation in semiconductor microcavities*, Physical Review B **66** (2002), no. 8, 085304.

[88] M. Richard, *Quasi-condensation de polaritons sous excitation incohérente dans les microcavités à base de CdTe*, Ph.D. thesis, Université Joseph Fourier, Grenoble, France, 2004.

[89] M. Richard, J. Kasprzak, R. Andre, R. Romestain, L. S. Dang, G. Malpuech, and A. Kavokin, *Experimental evidence for nonequilibrium bose condensation of exciton polaritons*, Physical Review B **72** (2005), no. 20, 201301.

[90] M. Richard, J. Kasprzak, R. Romestain, R. Andre, and L. S. Dang, *Spontaneous coherent phase transition of polaritons in CdTe microcavities*, Physical Review Letters **94** (2005), no. 18, 187401.

[91] A. Robert, O. Sirjean, A. Browaeys, J. Poupard, S. Nowak, D. Boiron, C. I. Westbrook, and A. Aspect, *A bose-einstein condensate of metastable atoms*, Science **292** (2001), no. 5516, 461–464.

[92] G. Rochat, C. Ciuti, V. Savona, C. Piermarocchi, A. Quattropani, and P. Schwendimann, *Excitonic bloch equations for a two-dimensional system of interacting excitons*, Physical Review B **61** (2000), no. 20, 13856–13862.

[93] M. Saba, C. Ciuti, J. Bloch, V. Thierry-Mieg, R. Andre, L. S. Dang, S. Kundermann, A. Mura, G. Bongiovanni, J. L. Staehli, and B. Deveaud, *High-temperature ultrafast polariton parametric amplification in semiconductor microcavities*, Nature **414** (2001), no. 6865, 731–735.

[94] S. Savasta, O. Di Stefano, and R. Girlanda, *Many-body and correlation effects in semiconductor microcavities*, Semiconductor Science And Technology **18** (2003), no. 10, S294–S300.

[95] S. Savasta, O. Di Stefano, and R. Girlanda, *Many-body and correlation effects on parametric polariton amplification in semiconductor microcavities*, Physical Review Letters **90** (2003), no. 9, 096403.

[96] S. Savasta, O. D. Stefano, V. Savona, and W. Langbein, *Quantum complementarity of microcavity polaritons*, Physical Review Letters **94** (2005), no. 24, 246401.

[97] V. Savona, C. Piermarocchi, A. Quattropani, P. Schwendimann, and F. Tassone, *Optical properties of microcavity polaritons*, Phase Transitions **68** (1999), no. 1, 169–279, Part B.

[98] V. Savona, P. Schwendimann, and A. Quattropani, *Onset of coherent photoluminescence in semiconductor microcavities*, Physical Review B **71** (2005), no. 12, 125315.

[99] P. G. Savvidis, J. J. Baumberg, R. M. Stevenson, M. S. Skolnick, D. M. Whittaker, and J. S. Roberts, *Angle-resonant stimulated polariton amplifier*, Physical Review Letters **84** (2000), no. 7, 1547–1550.

[100] P. G. Savvidis, J. J. Baumberg, R. M. Stevenson, M. S. Skolnick, D. M. Whittaker, and J. S. Roberts, *Asymmetric angular emission in semiconductor microcavities*, Physical Review B **62** (2000), no. 20, R13278–R13281.

[101] P. G. Savvidis, C. Ciuti, J. J. Baumberg, D. M. Whittaker, M. S. Skolnick, and J. S. Roberts, *Off-branch polaritons and multiple scattering in semiconductor microcavities*, Physical Review B **64** (2001), no. 7, 075311.

[102] P. Schwendimann, C. Ciuti, and A. Quattropani, *Statistics of polaritons in the nonlinear regime*, Physical Review B **68** (2003), no. 16, 165324.

[103] J. Shah, *Ultrafast spectroscopy of semiconductors and semiconductor nanostructures*, 2 ed., Springer Series in Solid-State Sciences, 1999.

[104] D. Snoke, S. Denev, Y. Liu, L. Pfeiffer, and K. West, *Long-range transport in excitonic dark states in coupled quantum wells*, Nature **418** (2002), no. 6899, 754–757.

[105] D. W. Snoke, J. L. Lin, and J. P. Wolfe, *Coexistence of bose-einstein paraexcitons with maxwell-boltzmann orthoexcitons in $Cu_2O$*, Physical Review B **43** (1991), no. 1, 1226–1228, Part B.

[106] D. W. Snoke, J. P. Wolfe, and A. Mysyrowicz, *Evidence for bose-einstein condensation of a 2-component exciton gas*, Physical Review Letters **64** (1990), no. 21, 2543–2546.

[107] H. Soda, K. Iga, C. Kitahara, and Y. Suematsu, *GaInAsP-InP surface emitting injection-lasers*, Japanese Journal Of Applied Physics **18** (1979), no. 12, 2329–2330.

[108] J. L. Staehli, S. Kundermann, M. Saba, C. Ciuti, A. Baas, T. Guillet, and B. Deveaud, *Non-linear dynamical effects in semiconductor microcavities*, Physica Status Solidi B-Basic Solid State Physics **242** (2005), no. 11, 2246–2259.

[109] J. L. Staehli, M. Saba, S. Kundermann, C. Ciuti, and B. Deveaud, *Quantum kinetics of parametric polariton scattering in microcavities*, Physica Status Solidi B-Basic Research **234** (2002), no. 1, 183–194.

[110] R. P. Stanley, R. Houdre, U. Oesterle, M. Gailhanou, and M. Ilegems, *Ultrahigh finesse microcavity with distributed bragg reflectors*, Applied Physics Letters **65** (1994), no. 15, 1883–1885.

[111] R. M. Stevenson, V. N. Astratov, M. S. Skolnick, D. M. Whittaker, M. Emam-Ismail, A. I. Tartakovskii, P. G. Savvidis, J. J. Baumberg, and J. S. Roberts, *Continuous wave observation of massive polariton redistribution by stimulated scattering in semiconductor microcavities*, Physical Review Letters **85** (2000), no. 17, 3680–3683.

[112] J. R. Tischler, M. S. Bradley, V. Bulovic, J. H. Song, and A. Nurmikko, *Strong coupling in a microcavity led*, Physical Review Letters **95** (2005), no. 3, 036401.

[113] J. P. Vanderziel, R. Dingle, R. C. Miller, W. Wiegmann, and W. A. Nordland, *Laser oscillation from quantum states in very thin* $GaAs - Al_{0.2}Ga_{0.8}As$ *multilayer structures*, Applied Physics Letters **26** (1975), no. 8, 463–465.

[114] W. S. Warren, H. Rabitz, and M. Dahleh, *Coherent control of quantum dynamics - the dream is alive*, Science **259** (1993), no. 5101, 1581–1589.

[115] M. U. Wehner, M. H. Ulm, and M. Wegener, *Scanning interferometer stabilized by use of pancharatnam's phase*, Optics Letters **22** (1997), no. 19, 1455–1457.

[116] T. C. Weinacht, J. Ahn, and P. H. Bucksbaum, *Controlling the shape of a quantum wavefunction*, Nature **397** (1999), no. 6716, 233–235.

[117] C. Weisbuch, M. Nishioka, A. Ishikawa, and Y. Arakawa, *Observation of the coupled exciton-photon mode splitting in a semiconductor quantum microcavity*, Physical Review Letters **69** (1992), no. 23, 3314–3317.

[118] X. J. Zhu, P. B. Littlewood, M. S. Hybertsen, and T. M. Rice, *Exciton condensate in semiconductor quantum-well structures*, Physical Review Letters **74** (1995), no. 9, 1633–1636.

[119] R. Zimmermann, *Excitons and electron-hole plasma - ground-state calculation*, Physica Status Solidi B-Basic Research **76** (1976), no. 1, 191–205.